

INGAN/GAN MULTIPLE QUANTUM WELL STRUCTURES: SUBMICRON
STRUCTURAL, OPTICAL, ELECTRICAL AND CHEMICAL PROPERTIES

by

Ying Li

A dissertation submitted to the faculty of
The University of North Carolina at Charlotte
in partial fulfillment of the requirements for the degree of
Doctor of Philosophy in
Optical Science and Engineering

Charlotte

2013

Approved by:

Dr. Edward B. Stokes

Dr. Michael A. Fiddy

Dr. Yong Zhang

Dr. Thomas A. Schmedake

©2013
Ying Li
ALL RIGHTS RESERVED

ABSTRACT

YING LI. InGaN/GaN multiple quantum well structures: submicron structural, optical, electrical and chemical properties.

(Under the direction of DR. EDWARD B. STOKES)

In this work, a novel approach has been implemented to investigate the submicron (30nm spatial resolution) structural and optical properties of bulk GaN, InGaN/GaN Multiple Quantum Well (MQW), p-type AlGaN capped MQW, and full Light Emitting Diode (LED) as-grown structures by stopping the Metal Organic Chemical Vapor Deposition (MOCVD) process at various points during the growth. 4 pair or 6 pair of 2.6nm $\text{In}_{0.14}\text{Ga}_{0.86}\text{N}/10\text{nm}$ GaN MQW structures have been grown at same well and barrier temperature (at 760°C), and at different well and barrier temperature (well at 760°C and barrier at 860°C). For the first time these structures have been analyzed layer by layer using high resolution Cathodoluminescence (CL) system. This technique allowed independent study of structural and carrier confinement effects of each layer on subsequent layers. Together with other characterization techniques, this novel approach can allow critical improvements in future LED development.

Owing to the ability of the CL system to study the luminescence properties in the vertical axis by changing the electron beam voltage, the nonradiative recombination centers (NRRCs) and radiation fluctuations beneath the surface were studied as a function of film depth. Pits and dislocations in bulk GaN and V-pits in MQW were shown to be NRRCs. Luminescence fluctuations, at about 30nm spatial resolution, in MQW emission wavelength was observed in CL images and correlated to local bandgap variation.

InGaN/GaN MQW layers revealed double peak emission at 2.74eV and 2.82eV. Optical

microscopy, Atomic Force Microscopy (AFM) and its electrical modules, X-ray diffraction (XRD), photoluminescence (PL), electroluminescence (EL), time resolved PL (TRPL), Scanning Transmission Electron Microscopy (STEM), and Secondary Ion Mass Spectrometry (SIMS) analysis were performed to investigate the origin of double peak emission. The low energy (LE) emission at 2.74eV was attributed to InGaN/GaN MQWs, and the high energy (HE) emission at 2.82eV to nanostructures formed surrounding the $(V_{\text{Ga}}-O_{\text{N}})^{2-}$ point defects mainly at the bottom pairs of MQW layer due to the strain relaxation by the point defects and the compositional pulling effect. This O impurity introduced HE emission decreases the quantum efficiency of the MQW structure and deteriorated the device performance by forming leakage paths. It was observed that O impurity incorporation was enhanced by defective nature of the films and low growth temperature. It was shown that higher temperature growth of GaN quantum barriers at 860°C eliminated the double peak InGaN emission.

ACKNOWLEDGEMENTS

The past three years of working for my PhD in UNC Charlotte while employed in Veeco Instrument Inc. and living in NJ is one of the most important and precious experiences in my life. I am extremely proud because not everyone has the opportunity to experience this and I MADE IT!

I have pictured writing the acknowledgements for countless times, when the countless mentoring, helps, and supports escorted me through this process. So many times I felt I was in a war and I was failing the battle, but every time I survived with grateful tears knowing how many loves, trusts, and supports I had been given.

Lixia Li and Changgang Li, my dear mom and dad, you gave my life and my belief. You taught me to be persistent on my pursuits and never easily gave up. I live and fought against all the difficulties with your loves. Mom, you said you were very proud of me. But I cannot be more proud that I am your daughter.

Center for Optoelectronics and Optical Communications in the University of North Carolina at Charlotte and Veeco Instrument Inc., you gave me all the opportunity to learn from elites, work with professionals, research with the best equipment and in the best atmosphere.

Dr. Stokes, my advisor, you walked me through the whole process with patience, mentoring, and care. You supported me to overcome this difficult remote PhD program and taught me a great many during the process. You have my greatest respect and the most special gratitude.

Dr. Fiddy, Dr. Zhang, and Dr. Schmedake, my committees, you helped me and gave me many great ideas during the proposal and defense. You have been so supportive and

have made the program much easier. I am really lucky to have such a knowledgeable and helpful committee.

Dr. Davies, my coordinator, without your understanding and kindness, my PhD experience cannot be so smooth and pleasant.

Dr. Lu and Mr. Ebert, my managers at Veeco Instrument Inc., your encouragement and support allowed me to survive my full time employment and part time PhD work.

Dr. Arif, Dr. Krishnan, Dr. Armour, Mr. Ramos, Mr. Krahnert, my colleagues at Veeco, thank you for sharing your expertise, mentoring me through new fields, and being supportive at work.

Beibei (Dr. Zhou), Ding, Yue, Yalong (Dr. Gu), Youfei, and Merry, my dear friends, you are the best and you make the difficult part time PhD life much easier for me. Cheng (Dr. Li), my dear colleague and comrade, I am so lucky that we worked through all these together and thank you for all your helps. Dan, my dear brother, you enlightened, mentored and helped me when I was in difficulties. Mingzhen (Dr. Tang), my dear sister, you always told me to hold on and you trusted me when I didn't even trust myself. I don't think I would have had the courage to continue if not because of you. Acar (Dr. Erkan A. Berkman), my dear colleague and friend, you were the most knowledgeable scientist and teacher; you were the most patient and helpful reviewer; you were the most soothing and caring counselor; you were the most supportive and tolerant friend. Thank you for all those help and support you have given me.

TABLE OF CONTENTS

CHAPTER 1: INTRODUCTION	1
1.1 InGaN/GaN MQW LED	2
1.2 MOCVD Technology	3
1.3 CL Technology	3
1.4 Dissertation Structure	4
CHAPTER 2: LIGHT EMITTING DIODE	5
2.1 Luminescence	5
2.1.1 Interband Luminescence in Direct Bandgap Materials	7
2.1.2 Types of Luminescence	9
2.2. Light Emitting Mechanism	12
2.3 InGaN/GaN MQW LED	14
2.3.1 III-N Materials	14
2.3.2 Lattice Mismatch and Strain	15
2.3.3 Quantum Confinement Effects	17
2.3.4 Polarization and Piezoelectric Effects	22
2.3.5 Defects and the Effects	25
CHAPTER 3: MOCVD PROCESS OF INGAN/GAN MQW LED STRUCTURES	29
3.1 MOCVD Theory	29
3.2 Veeco TurboDisc K465i MOCVD System	31
3.3 Epitaxial Process	34
3.3.1 C-plane Sapphire Substrate	35
3.3.2 GaN Nucleation Layer	37

	viii
3.3.3 3D GaN Roughening Layer	38
3.3.4 GaN Layers	40
3.3.5 InGaN/GaN MQW Active Layer	42
3.3.6 p-AlGaN Electron Blocking Layer	44
3.3.7 p-GaN Layer	45
CHAPTER 4: SEM-CL TECHNOLOGY	47
4.1 Electron Interaction in Semiconductor	47
4.2 SEM	49
4.3 CL	50
4.4 Previous Studies on the Effects of Electron Beam on GaN Based Structures	51
CHAPTER 5: EXPERIMENTS DETAILS	53
5.1 Sample Description	53
5.1.1 Sample Set 4: nGaN Structures	54
5.1.2 Sample Set 3: MQW Structures	55
5.1.3 Sample Set 2: pAlGaN Capped MQW Structures	56
5.1.4 Sample Set 1: LED Structure	57
5.2 Characterization Techniques	58
5.2.1 Microscope	58
5.2.2 AFM, SCM, and CAFM	58
5.2.3 XRD	59
5.2.4 Time Resolved PL	59
5.2.5 EL	60
5.2.6 SEM-CL	60

	ix
5.2.7 STEM	63
5.2.8 SIMS	64
CHAPTER 6: RESULTS AND DISCUSSION	65
6.1 nGaN As-grown Structure: Sample A4 and C4	65
6.1.1 Surface Morphology	65
6.1.2 SEM-CL and Spot CL Analysis	66
6.1.3 STEM Analysis	70
6.2 MQW As-grown Structure (Sample A3, B3 and C3)	71
6.2.1 Surface Morphology	71
6.2.2 XRD Analysis	72
6.2.3 Room Temperature Power Dependent PL Analysis	73
6.2.4 CL Analysis	75
6.2.5 Time Resolved PL Analysis	93
6.2.6 AFM-SCM Analysis	95
6.2.7 STEM Analysis	98
6.2.8 SIMS Analysis	99
6.2.9 Summary of Double Peak InGaN Emission	103
6.3 AlGaIn Capped MQW Structure (Sample A2)	105
6.3.1 Surface Morphology	105
6.3.2 SEM-CL Analysis	106
6.4 LED As-grown Structure (Sample A1 and B1)	112
6.4.1 EL Test	112
6.4.2 Surface Morphology	113

	x
6.4.3 SEM-CL Analysis	114
6.4.4 AFM-CAFМ Analysis	118
6.5 Summary of Experiment Results	119
CHAPTER 7: CONCLUSIONS	122
REFERENCES	125

LIST OF SYMBOLS AND ABBREVIATIONS

3D	3 dimensional
μm	micron (10^{-6} m)
\AA	angstrom (10^{-10} m)
AFM	atomic force microscope
Al	aluminum
AlGaAs	aluminum gallium arsenide
AlGaN	aluminum gallium nitride
AlN	aluminum nitride
CAFM	conductive atomic force microscope
CL	cathodoluminescence
CP ₂ Mg	cyclopentadienylmagnesium
Cs	cesium
C-V	capacitance-voltage
DC	direct current
e	electron
EB	electron beam
EBL	electron blocking layer
ED	edge dislocation
EDS	energy dispersive x-ray spectroscopy
EFS	electron flight simulator
E_g	band gap energy

EL	electroluminescence
eV	electron volt
FE-SEM	field emission scanning electron microscopy
FIB	focus ion beam
FWHM	full width at half maximum
Ga	gallium
GaAs	gallium arsenide
GaN	gallium nitride
Ge	germanium
GE	general electric
h	hole
H	hydrogen
He-Cd	helium – cadmium
HE	high energy
HRTEM	high resolution transmission electron microscopy
HVPE	hydride vapor phase epitaxy
IQE	internal quantum efficiency
I-V	current-voltage
In	indium
InGaN	indium gallium nitride
InN	indium nitride
k_B	boltzmann constant
LE	low energy

LEEBI	low energy electron beam irradiation
LED	light emitting diode
MBE	molecular beam epitaxy
Mg	magnesium
MOCVD	metal organic chemical vapor deposition
MQW	multiple quantum well
N	nitrogen
NH ₃	ammonia
NL	nucleation layer
Nm	nanometer (10^{-9} m)
NRRC	nonradiative recombination center
O	oxygen
°C	degree celsius
PL	photoluminescence
PMT	photomultiplier tube
PSS	patterned sapphire substrate
PZ	piezoelectric
Q	charge of a particle
QCSE	quantum confined stark effect
QD	quantum dot
RMS	root mean square
Rpm	revolutions per minute
RRC	radiative recombination center

SCM	scanning capacitance microscope
SD	screw dislocation
SEM	scanning electron microscopy
SE SEM	secondary electron scanning electron microscopy
Si	silicon
SiC	silicon carbide
SIMS	secondary ion mass spectrometry
SP	spontaneous polarization
STEM	scanning transmission electron microscopy
TEGa	triethylgallium
TEM	transmission electron microscopy
TD	threading dislocation
Ti	titanium
TMA	trimethylaluminium
TMGa	trimethylgallium
TMIn	trimethylindium
Torr	a unit of pressure, equal to 1.316×10^{-3} atmosphere
TRPL	time resolved photoluminescence
UV	ultraviolet
V	volt
Xe	xenon
XRD	x-ray diffraction

CHAPTER 1: INTRODUCTION

LEDs have attracted the interest of researchers all over the world, and proven to be versatile light sources with a bright future. III-Nitride compounds are among the most promising materials for LEDs, and their great potential in blue, violet, and UV light emitting devices have been widely explored, investigated, and successfully commercialized. InGaN/GaN MQW LEDs emitting at about 370nm to 500nm, which still exhibit issues like less than optimum quantum efficiency and efficiency droop, have nevertheless proven their significance in the blue LED industry that drives Solid State Lighting for general illumination. MOCVD has been the main technique used for epitaxial growth of InGaN/GaN MQW LEDs in industry. Great efforts have been and still are made to refine the system design and improve the process. During the development of this industry, many analytical techniques have been used, such as X-ray Diffractometer, AFM, TRPL, SIMS, SEM, and CL.

Figure 1.1 shows the thematic diagram of the experiment that will be discussed in this dissertation. InGaN/GaN MQW LED wafers and epitaxial structures stopped at various points during the full LED structure growth were grown by MOCVD system and characterized by various analytical techniques. The structural, optical, electrical, and chemical properties will be studied and discussed.

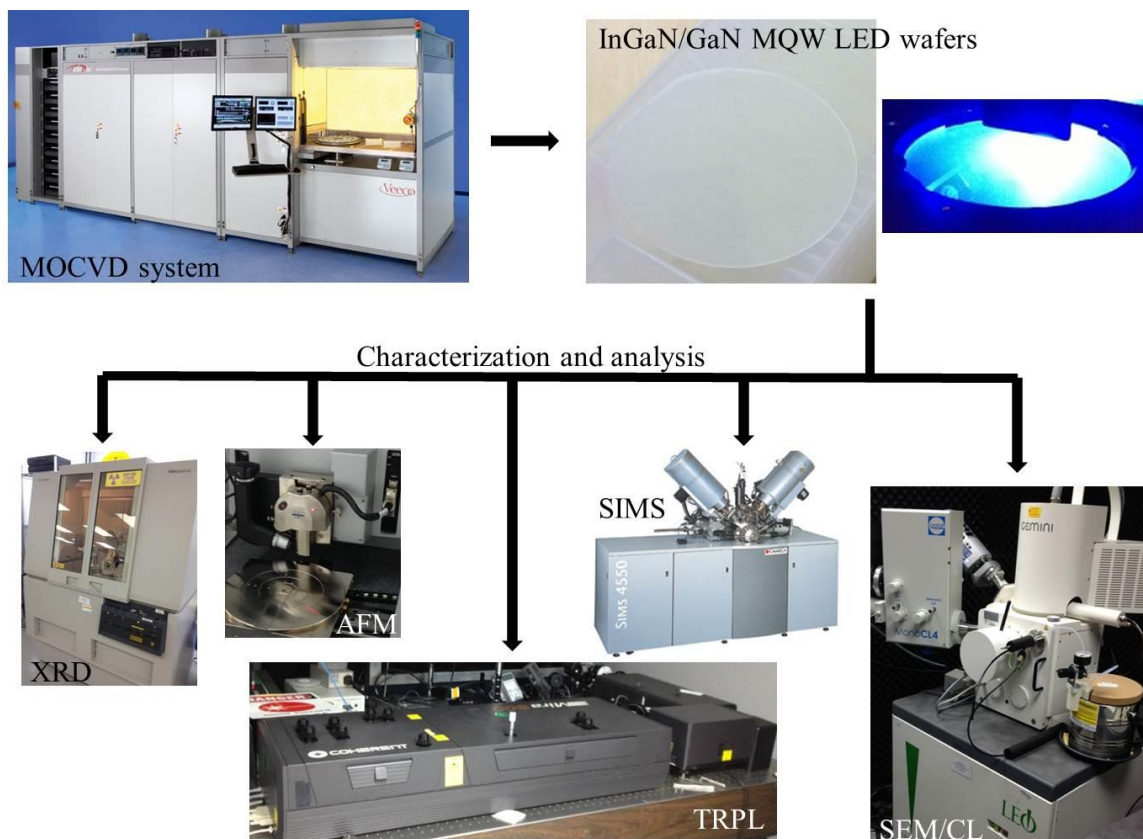


Figure 1.1: Thematic diagram of the experiment

1.1 InGaN/GaN MQW LED

It was two decades ago when Dr. Nakamura et al. first reported the GaN/InGaN/GaN blue LED by MOCVD [1], in which a bulk InGaN/GaN double heterostructure was grown epitaxially on sapphire substrate. Carriers were confined in the bulk InGaN active layer due to the smaller bandgap compared with that of GaN. Later, InGaN/GaN single quantum well and multiple quantum well structures were grown as the active layer and were investigated, considering the higher quantum efficiency may be achieved due to the quantum confinement of carriers. In these structures, attribute to the great difference in lattice constant (30% difference), high density of threading dislocations (up to 10^{10} cm^{-2})

propagate along the growth direction and intersect the active light emitting layers. Even though no light emission will be expected considering the high defect density, luminescence was obtained despite the high density of defects, V-pits, in these structures. Therefore, InGaN/GaN LED structures have been extremely interested by a great many researchers. Numerous researches have been done to develop InGaN/GaN MQW and LED structures, to improve the process conditions, and to study the role of impurities and defects. The present dissertation will study and discuss these in detail.

1.2 MOCVD Technology

Various techniques have been implemented for epitaxial growth of III-N thin films. However, of all the techniques employed, MBE and CVD techniques have been adopted most commonly for the epitaxial growth of thin III-N layers.

For the growth of III-N based optoelectronic devices, MOCVD has been the predominant growth technology due to the application in growing various III-V materials with good control on single layer thickness, interface abruptness, surface uniformity, and the ability to deposit heterostructures in a single experiment and highly controlled p- and n-doping of individual layers. Initially, MOCVD was defeated by MBE in its real time in-situ monitoring. Today, most MOCVD chambers are equipped with advanced in-situ monitoring tools that provide metrology of growth surface.

All the samples studied in this dissertation were grown by MOCVD system.

1.3 CL Technology

Among the characterization techniques, high resolution CL is a very significant one. A great many efforts have been put into developing techniques to observe localized luminescence properties in semiconductors due to their importance in studying

semiconductor physics and optoelectronic devices. CL is a powerful tool for this purpose because of its capability of carrying out experiments of large scanning areas and short total measuring time. By scanning a large area of the sample with electron beam, any point on the sample can be measured easily compared with using piezo-driving devices. Besides, since the excitation intensity of an electron beam is significantly larger than that of laser, high luminescence intensity can be achieved by CL technique. The high intensity allows decreasing exposure time and thus faster response. Moreover, by controlling the electron beam diffusion depth into the semiconductor structure, a depth dependent luminescence study can be executed.

In this dissertation, SEM-CL system and CL spectrometry will be applied to the MOCVD As-grown structures to study the submicron optical properties and also the effects of impurity on the optical properties of MQW structure with the assist of the results from other analytical techniques.

1.4 Dissertation Structure

The dissertation is divided into the following chapters. In chapter 2, the concept of luminescence is introduced, the mechanism for LED is explained and the structural and piezoelectrical properties of InGaN/GaN MQW LED are described. The MOCVD technique and process conditions for the InGaN/GaN MQW LED structural are described in chapter 3. Chapter 4 summarizes the SEM-CL technology and the previous studies on the electron beam induced effects on the GaN based heterostructures. Chapter 5 describes the experiment details and chapter 6 summarizes the experiment results and discusses the submicron structural, optical, electrical and chemical properties of the MOCVD As-grown structures. Conclusions are presented in chapter 7.

CHAPTER 2: LIGHT EMITTING DIODE

Light Emitting Diode was discovered in 1904 and the first LED results were published in 1907. LEDs became forgotten only to be re-discovered in the 1920's and again in the 1950's. In the 1960's, several groups pursued the demonstration of semiconductor lasers, when the first viable LEDs were produced. Since then, light emission from semiconductor devices has attracted the interest of researchers all over the world. During the last four decades, LEDs have become devices in hot spot, and nowadays, are versatile light sources with a bright future.

2.1 Luminescence

In solids, when electrons in excited states spontaneously drop down to a lower energy level and emit photons, this radiative emission process is called luminescence. Luminescence can occur by various mechanisms, such as photoluminescence, electroluminescence, bioluminescence, chemoluminescence, thermoluminescence, and mechanoluminescence.

In semiconductor materials, the luminescence process happens between conduction band and valence band. Figure 2.1 [2] gives an overview of the luminescence process in semiconductor materials, where the black solid circle stands for electrons and hollow circle for holes, and these symbols will be used through the whole dissertation. When an electron

in conduction band drops down into valance band, such as the ground state, a photon emission can take place. To obtain luminescence, first, electrons must be injected to the conduction band, and then relax to the valance band. Second, the phonon cannot be emitted unless valance band is empty, since the Pauli principle does not allow two electrons in the same level. The empty valance band is produced by injecting holes. Third, photon emission can only happen when the transition is radiative, τ_R standing for the radiative lifetime of the transition. Radiative emission is not the only mechanism by which the electrons in conduction band can fall to valance band, and the alternative pathway is the non-radiative relaxation, τ_{NR} standing for the non-radiative lifetime of the transition. In this mechanism, the electron may lose its excitation energy as heating by emitting phonons, or it may transfer the energy to impurities or defects. If non-radiative relaxation processes occur on a faster time scale than the radiative transitions, very little luminescence can be observed, and the luminescence is called not efficient.

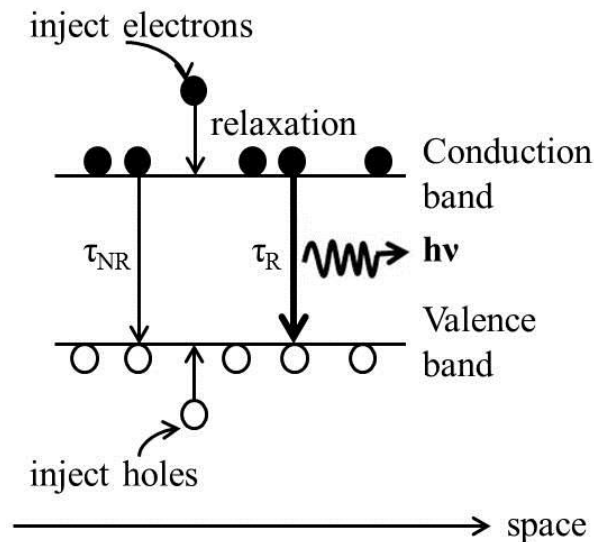


Figure 2.1: General schematic of luminescence in semiconductor materials

2.1.1 Interband Luminescence in Direct Bandgap Materials

Interband luminescence occurs when the electron transition is from conduction band to valence band. The process that an electron in conduction band drops down to an empty level in the valence band made by a hole and takes its place is called electron-hole recombination. There are two kinds of electron-hole recombination, radiative recombination and non-radiative recombination, depending on whether photon emission happens or not.

Before the interband transition, the electrons in the conduction band will relax very rapidly to the lowest level within the conduction band, and holes follow a similar relaxation process in the valence band. The photon is emitted between the electron and hole states thermally occupied, and will only be emitted within a narrow energy range from the bottom of conduction band to the top of valence band.

In direct Bandgap materials, the minimum of the conduction band and the maximum of the valence band are at same wavevector. Figure 2.2 shows the band diagram for an interband luminescence process in a direct Bandgap semiconductor [2].

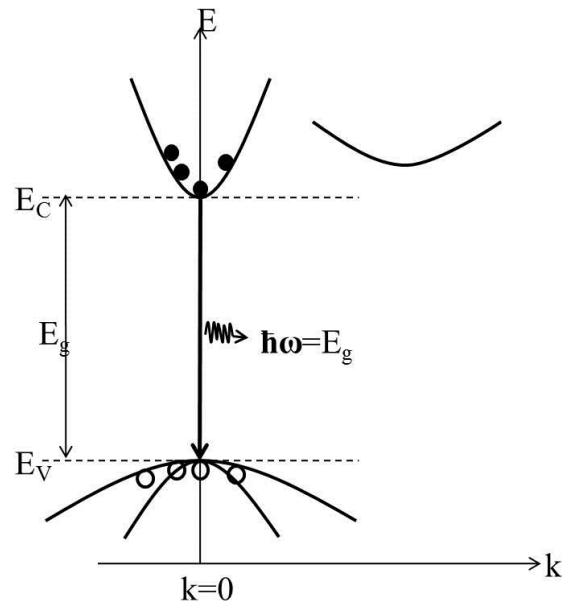


Figure 2.2 Interband luminescence process in a direct bandgap semiconductor

Because the optical transitions between the conduction and valence bands of direct bandgap semiconductors are dipole allowed and have large matrix element, and the radiative lifetime is short, with typical values in the range 10^{-8} - 10^{-9} s, the luminescence efficiency for direct bandgap material is relatively high [2].

Since no phonon is required during this direct bandgap transition and the momentum of the photon is negligible compared to the momentum of the electron, the radiative recombination must take place between the electrons and holes that have the same wavevector k . The emission happens near $k=0$, which corresponds to a photon of energy E_g . Therefore, the emission edge should satisfy Equation (2-1).

$$\lambda(\mu m) = \frac{hc}{E_g} = \frac{1.24}{E_g(eV)} \quad (2-1)$$

2.1.2 Types of Luminescence

There are many types of luminescence, categorized by how it is initiated. For examples, chemiluminescence is a result of a chemical reaction; mechanoluminescence is a result of a mechanical action on the material; and thermoluminescence is the re-emission of absorbed light when a substance is heated. A few kinds of luminescence (PL, EL, and CL) which are involved in the present studies will be discussed in detail.

2.1.2.1 Photoluminescence

Photoluminescence is a luminescence mechanism, in which phonon re-emission takes place after absorbing a photon of higher energy. Figure 2.3 shows the schematic diagram of the processes occurring during photoluminescence in a direct bandgap semiconductor after excitation [2]. An excitation source such as a laser, LED, or lamp, is used to inject electrons into the conduction band and holes into the valence band by providing photons with energy larger than bandgap. When the electrons are excited to higher energy levels in conduction band, they rapidly relax and drop to the lower energy states by emitting phonons. The relaxation process is indicated by the cascade of transitions within the conduction and valence bands. Each drop indicates the emission of one phonon, which has the energy and momentum to satisfy the conservation laws.

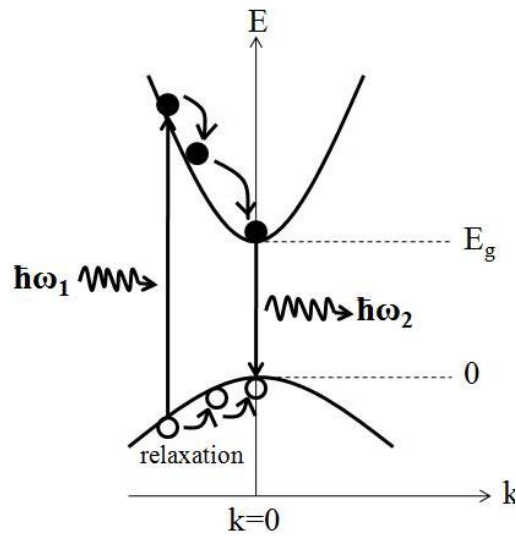


Figure 2.3: Photoluminescence in a direct bandgap semiconductor

Photoluminescence spectroscopy is mainly applied to the semiconductor research as a diagnostic and development tool. Figure 2.4 shows a basic photoluminescence spectroscopy test setup. The sample is illuminated by a laser or LED or lamp with photon energy larger than E_g . The photoluminescence is emitted at lower frequencies, a portion of it collected by a lens and focused onto the entrance slit of a spectrometer. The spectrum is then recorded by a detection program.

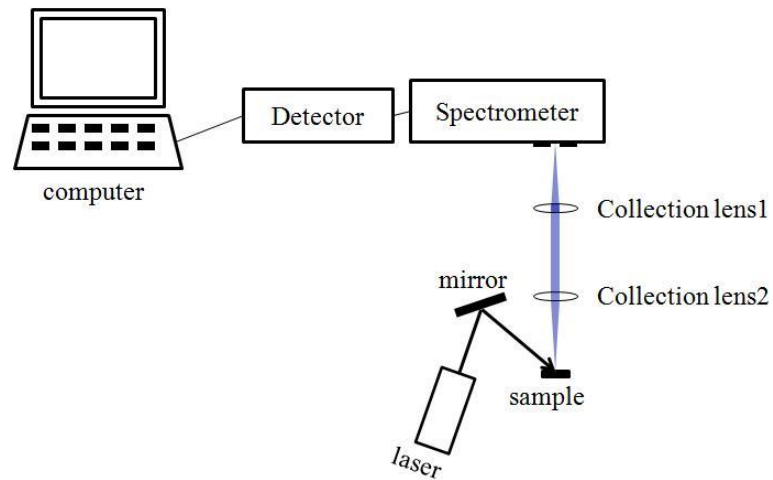


Figure 2.4: Photoluminescence test setup

2.1.2.2 Electroluminescence

In electroluminescence, the emission of photons is caused by running an electrical current through the material. Figure 2.5 shows circuit diagram of EL on a MQW LED structure with p-side on top. The diode is operated in forward bias, with a current flowing from the p-type layer through the MQW active region to the n-type layer. The luminescence is generated in MQW region by the recombination of electrons and holes flowing in from the n-type and p-type layer, respectively.

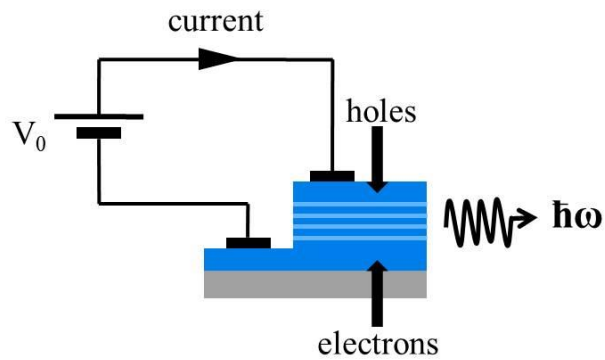


Figure 2.5: Circuit diagram for a MQW LED structure

The band diagram for electroluminescence is almost same as that for photoluminescence in Figure 2.4. The only difference is that the electrons and holes are injected electrically rather than optically.

2.1.3.3 Cathodoluminescence

Cathodoluminescence is an optical and electromagnetic phenomenon in which electrons interact on a luminescent material and generate electron-hole pairs which recombine in the material radiatively and lead to light emission.

The band diagram is almost same as that for photoluminescence in Figure 2.4. The only difference is that the electrons and holes are generated by secondary electrons excited by the incident electron beam.

2.2. Light Emitting Mechanism

Figure 2.6 shows the band diagram of a MQW LED with p-type EBL, in which photons are generated by luminescence, electroluminescence, or cathodoluminescence [3]. A large population of electrons is injected into conduction band, and holes into valence band. In thermal equilibrium at zero bias, the bands align with the Fermi energies of the p- and n-regions at the same energy, as shown in Figure 2.6 (a)., No light can be emitted at the MQW active region, because there is no significant population of electrons and holes. However, when a forward bias is applied to drive a current through the device, the Fermi levels shift and the active region shrinks, which allows the electrons in the n-region to diffuse into the MQW region, and vice versa, as shown in Figure 2.6 (b). This creates a region where both electrons and holes are present, where the electrons recombine with the holes, and emitting photons by interband luminescence.

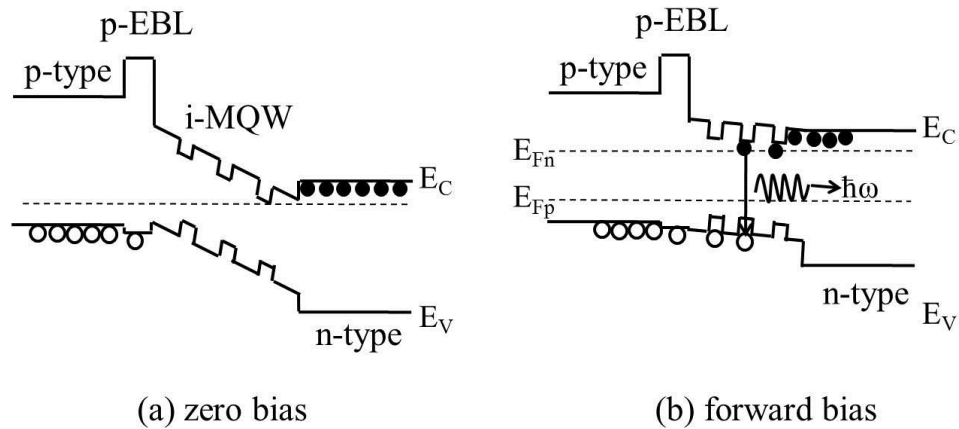


Figure 2.6: Band diagrams of a MQW LED with p-type EBL at (a) zero bias, and (b) forward bias

An LED emits light by spontaneous emission, which, compared with stimulated emission in laser, requires a smaller forward bias. Therefore, LEDs operate at lower current densities than lasers, which makes LEDs are more reliable devices compared with laser diodes since they avoid high power caused degradation. An ideal LED exhibits a linear light output-current characteristic, unlike that of an injection laser, and is therefore very suitable for analog modulation. The light-current characteristic is also more stable to temperature than that is a laser. Besides, an LED does not require an optical cavity and mirror facets to provide feedback of photons. The emitted photons have random phases, making the LED an incoherent light source. The linewidth of the spontaneous emission is approximately equal to the photoluminescence linewidth, which is typically 30-50 nm at room temperature. Thus, many optical modes are supported and therefore the LED is a convenient multimode optical source, suitable for use with multimode fibers.

2.3 InGaN/GaN MQW LED

2.3.1 III-N Materials

Significant attention in semiconductor electronic and optoelectronic devices have been won by III-N materials. III-Ns refer to GaN, AlN, InN, AlGaN, InGaN, AlInN, and AlInGaN. Compared to other semiconductor materials, III-Ns exhibit many unique and outstanding properties. First of all, any direct bandgap in 0.7eV (InN) to 6.2eV (AlN) range can be achieved by changing the composition in the III-Ns alloys. Second, the wide bandgap energy, which results from strong bonding, shows a great advantage in its low intrinsic carrier concentrations, n_i , over a wide temperature range, because n_i is exponentially dependent on bandgap. As a result, compared to Si or GaAs based optoelectronic devices, III-Ns based ones exhibit lower leakage and dark currents. Moreover, attribute to the wide energy gap, III-Ns are physically, chemically and thermally stable, and they present high thermal conductivities. Third, III-Ns are most stable in wurtzite crystallographic structure compared with semiconductor materials with cubic symmetry, such as Si and GaAs. Therefore, III-Ns lack inversion symmetry, which makes them polar crystals that exhibit properties such as piezoelectricity, pyroelectricity and nonlinear optical properties. Fourth, the charge carriers, i.e., electrons and holes, possess larger effective masses, and thus lower carrier mobilities than Si and GaAs based semiconductors materials, which, on the other hand, is compensated by the high saturation drift velocity of carriers. Fifth, nitride based devices are more environmentally green and less toxic than the other compound semiconductors. All the distinctive properties discussed above make III-Ns crucial for the development of powerful and stable electronic and optoelectronic devices. [5]

Despite all the advantages exhibited by III-N materials, the development of the epitaxial process has been very challenging. Multiple problems had to be solved, such as discovering suitable substrates, application of complicated epitaxial growth techniques, and achieving n-type and p-type doping. Take GaN as an example. It was eight decades ago when the growth of single crystal GaN was first attempted. GaN was synthesized by passing NH_3 through hot liquid Ga. By using this method, the structural properties of the material such as lattice constant and molecular structure were investigated by Juza et al. [6], and the PL properties were studied by Grimmeiss et al. [7], which produced inherently n-doped GaN attributed to N vacancies in the high growth temperature atmosphere. Whereas, Seifert et al. reported that this n-type conductivity was actually caused by O impurities from the chamber material, quartz, and/or reactor leaks [8]. Pankove et al. grew the first GaN based LEDs, in which a Metal – intrinsic – n-type structure was used [9]. Even though a great many of findings and improvements were accomplished for the employment of GaN based devices during that time period, the lack of suitable substrates, well-developed epitaxial process, and the inability to grow p-type doped material hindered the development of GaN and its alloys until the late 1980's.

2.3.2 Lattice Mismatch and Strain

Lattice matching is determined by the lattice constants of the epitaxial layers and the substrate. If the lattice constant for the substrate material is a_s , and that for the epitaxial overlayer is a_e , then the lattice mismatch or misfit is defined as Equation (2-2) [4].

$$\frac{\Delta a}{a_e} = \frac{a_e - a_s}{a_e} = -f . \quad (2-2)$$

Therefore, a lattice match between the two crystalline structures can only be achieved when elastic strain is exerted on one or both crystals. Usually the substrate is significantly

thicker than the epitaxial layer. As a result, the atoms of the epitaxial layer are displaced, which is shown in Figure 2.7 [4]. When the strain is applied onto the epitaxial layer, the lattice constant of the epitaxial layer in the direction parallel to the interface has to match the lattice constant of the substrate. Meanwhile, the lattice constant of the epitaxial layer perpendicular to the substrate is varied due to Poisson effect. If the parallel lattice constant is forced to decrease, i.e., a compressive strain is applied, the perpendicular lattice constant will increase, shown in Figure 2.7 (b). Conversely, if the parallel lattice constant of the epitaxial layer has to increase, i.e., a tensile strain is applied, the perpendicular lattice constant will decrease, shown in Figure 2.7 (c).

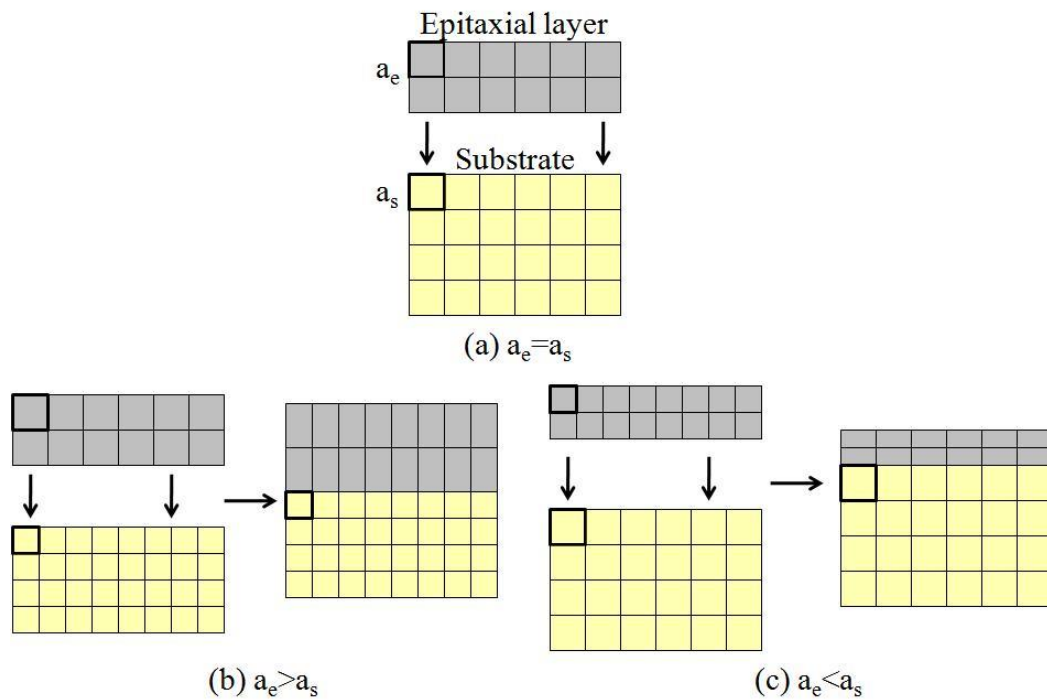


Figure 2.7: Accommodation of lattice between epitaxial layer and substrate

If the lattice match condition is not satisfied, crystal dislocations are likely to form in the epitaxial layer, as shown in Figure 2.8 [4]. Misfit dislocations usually propagate upward

during the growth and form threading dislocations.

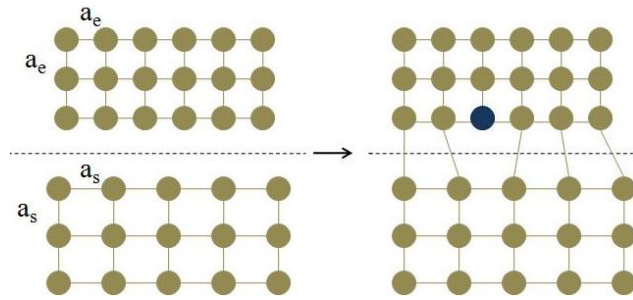


Figure 2.8: The formation of an edge misfit dislocation

In the case of wurtzitic $\text{In}_x\text{Ga}_{1-x}\text{N}$ growth on c-plane GaN, a compressive strain is exerted on the epitaxial layer. For example, when $x=0.11$ (11% InN), $a_0^{\text{GaN}}=3.189\text{\AA}$ and $a_0^{\text{InGaN}}=3.540\text{\AA}$. In this situation, there is a considerable lattice mismatch of 9.9%. The initial growth of $\text{In}_x\text{Ga}_{1-x}\text{N}$ is strained coherently. The lattice constant of InGaN epitaxial layer expands in the perpendicular direction, i.e., the c-direction, under the compressive strain due to Poisson effect. The strain increases with the $\text{In}_x\text{Ga}_{1-x}\text{N}$ layer thickness until the critical layer thickness is reached. Above this critical layer thickness, misfit dislocations are formed and strain energy is thus released.

2.3.3 Quantum Confinement Effects

According to quantum-mechanical rules [10][11], particles in the diameter range 1-10 nm would exhibit electronic band structures of nanoparticles,. The consequential physical properties are highly depend on the shape of the nanoparticles, interparticle distance, particle size, and characteristic of the capping organic shell, different to those of bulk materials or those of molecular compounds. Those exclusive properties are called quantum size effect, which is involved when the de Broglie wavelength of the valence electrons is comparable to the size of the particle.

There are three confinement regimes, according to the size of material [12]. (i) The weak confinement regime, in which the material diameter, R , is larger than the bulk exciton Bohr radius a_B ; (ii) the moderate-confinement regime, in which $R \approx a_B$, and $a_h < R < a_e$, where a_h is the hole Bohr radius, and a_e the electron Bohr radius; and (iii) the strong-confinement regime, in which $R < a_B$, and $R < a_h, a_e$.

2.3.3.1 Quantized Energy Subbands

Take quantum well for example, which is a potential well that confined particles in z direction, forcing them to move in the xy plane. Schroedinger's equation and the effective mass approximation are used to calculate the energies of the quantized states in the conduction and valence bands in this situation. The total energy for an electron or hole in the n th quantum level is shown in Equation (2-3) [2]:

$$E^{total}(n,k) = E_n + \frac{\hbar^2 k_n^2}{2m^*}, \quad (2-3)$$

where E_n is the quantized energy of the n th level, k_n is the wave vector, and m^* is the effective mass. For infinite potential wells, the form of wave function describes a standing wave inside the well with nodes at the interface. The energy that corresponds to the n th level is shown in Equation (2-4) [2]:

$$E_n = \frac{\hbar^2 k_n^2}{2m^*} = \frac{\hbar^2}{2m^*} \left(\frac{n\pi}{d} \right)^2, \quad (2-4)$$

where d is the width of quantum well.

Although real quantum wells have finite barriers, the infinite barrier model is a good starting point for a discussion of their properties.

The energy of the levels is inversely proportional to the effective mass and the square of the well width. This means that low mass particles in narrow quantum wells have the

highest energies. In addition, since the energy depends on the effective mass, the electrons, heavy holes and light holes will all have different quantization energies. In conduction band, electron energies will have larger energy gaps than those of the hole energies on the same quantum level in the valence band. In the valence band, the heavy holes will have the lowest energy, and are dominant in most situations because they form the ground state level [2]. Figure 2.9 shows the quantized energy levels in a quantum well.

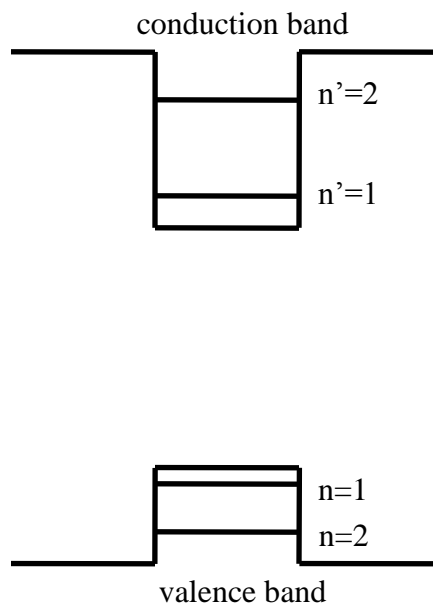


Figure 2.9: Energy levels in the quantum well

If the size of the semiconductor material is comparable to or even smaller than the Bohr radius, the moves of charge carriers will be confined to a limited space. Picture an electron in a box with finite size, when the box gets smaller, the kinetic energy and excitation energy increase. Therefore, the band gap energy of semiconductor particles increases when the size is smaller than their Bohr radius. Meanwhile, bandgap increases and becomes dependent to the size of the particles. [13]

In this study, the emission band we observe are primarily ground state to ground state, i.e., $n'=1$ to $n=1$.

2.3.3.2 Quantized Density of State

Consider the two-dimension absorption for a quantum well for simplification. Since the energy levels in conduction band and valence band are quantized, interband transition can only occur at a discrete set of energies. The energy of transition is given by Equation (2-5) [2]:

$$\hbar\omega = E_g + E_{hhn} + E_{en}, \quad (2-5)$$

where E_g is the band gap of the quantum well material, E_{hhn} is the n th heavy hole energy, and E_{en} is the n th electron energy.

The 3-D bulk semiconductor has a parabolic density of states given by Equation (2-6) [2]. By contrast, the joint density of states for a 2-D material is independent of energy and is given by Equation (2-7) [2].

$$g(E) = \frac{1}{2\pi^2} \left(\frac{2m^*}{\hbar^2} \right)^{\frac{3}{2}} E^{\frac{1}{2}}. \quad (2-6)$$

$$g(E) = \frac{\mu}{\pi\hbar^2}, \quad (2-7)$$

where μ is the electron-hole reduced effective mass defined in Equation (2-8) [2].

$$\frac{1}{\mu} = \frac{1}{m_e^*} + \frac{1}{m_h^*}. \quad (2-8)$$

This means that the joint density of states and absorption coefficient have a step-like structure, being zero up to the threshold energy, and then having a constant non-zero value for larger photon energies. The threshold energy for the n th transition is given by Equation (2-9) [2].

$$\hbar\omega = E_g + \frac{\hbar^2 n^2 \pi^2}{2m_e^* d^2} + \frac{\hbar^2 n^2 \pi^2}{2m_h^* d^2} = E_g + \frac{\hbar^2 n^2 \pi^2}{2\mu d^2}. \quad (2-9)$$

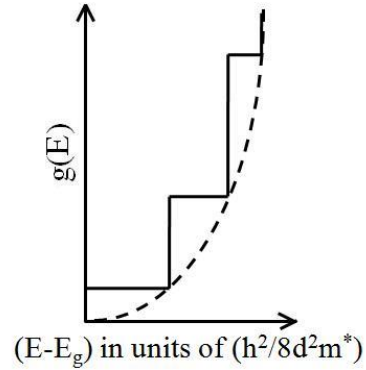


Figure 2.10: Step like density of states for a quantum well

2.3.3.3 Phonon Assisted Stimulated Emission

Other than trapping and confining photogenerated carriers, the quantum size structure tends to confine the recombination radiation. If most of the photogenerated carriers are trapped and thermalized in the quantum confined region, a large phonon population can be accumulated and confined [14][15]. These phonons participate and assist the stimulated emission, and increase the rate of recombination radiation.

2.3.3.4 The Quantum Confined Stark Effect

When there is no external electric field, quantum size confined carriers will only occupy states within a discrete set of energy subbands. In another word, only photons with a discrete set of wavelengths can be absorbed. When there is an external electric field, the energy band tilts, the electron and hole states shifting to lower energies respectively, and electrons and holes pushed in opposite directions, which causes red shift of the absorption edge.

Besides the shift in energy level, the external electric field results to decrease of absorption coefficient, since electrons and holes are pushed to opposite directions and the overlap of electron-, and hole-wave function is decreased as depicted in Figure 2.11 [5].

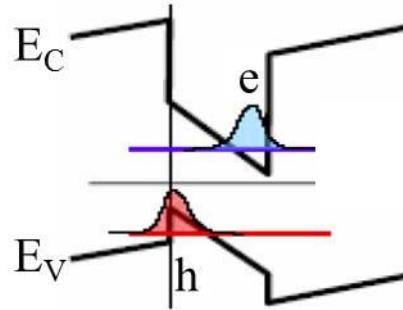


Figure 1.11: Bending of the band diagram due to QCSE

Since photon absorption of quantum size material can be controlled by changing electric bias, quantum confined Stark effect is applied to optical modulator.

2.3.4 Polarization and Piezoelectric Effects

The polarization in the III-N materials system is a result from both spontaneous and piezoelectric components. This polarization phenomenon depends upon the crystal growth direction.

The intrinsic polar bonds and the crystal structure without inversion symmetry lead to spontaneous polarization in a material. Wurtzite III-N materials exhibit spontaneous polarization because of the highly ionic bond result from the large difference in electronegativity between Ga/In/Al and N, and wurtzite structure lacking of inversion symmetry, i.e., same atoms on the same plane. Spontaneous polarization does not exist in semiconductors with zinc-blende cubic structure. The polarity of the crystal decides the direction of SP. In the present work, Ga-faced GaN materials are used, in which the

direction of the SP is from the substrate to the surface.

Besides, III-Ns exhibit piezoelectricity, i.e., the characteristic of generating an electric potential under applied mechanical stress. As a result, the compressive strain in InGaN induces an internal piezoelectric field. The polarity of the crystal and the kind of elastic strain, i.e., compressive or tensile strain, decide the direction of PZ polarization together. In the present work, $\text{In}_x\text{Ga}_{1-x}\text{N}$ layers are grown under compressive stress on Ga-faced GaN. The PZ field is be towards the substrate, as shown in Figure 2.12 [5].

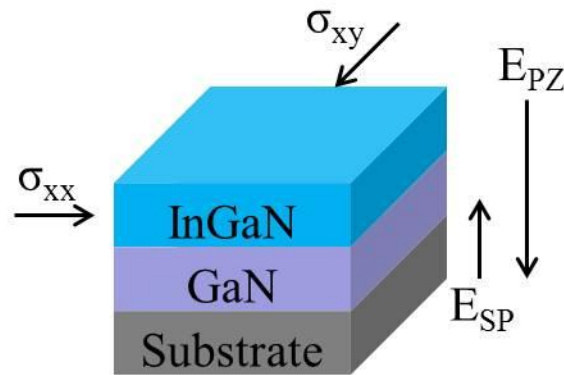


Figure 2.12: SP and PZ polarization of InGaN grown on Ga-faced GaN

Therefore, the total internal field is comprised of piezoelectric polarization and spontaneous polarization. In $\text{In}_x\text{Ga}_{1-x}\text{N}$ materials, the PZ polarization is usually more than 10 times larger than spontaneous polarization due to the highly strained nature of InGaN and thus the latter is negligible in the present discussion. Besides, the spontaneous polarization of GaN and InN are very similar, which results to a small spontaneous polarization field.

If we consider a p-AlGaIn/n-GaN structure whose band structure is shown in Figure 2.13, in equilibrium, a linear band tilt happens due to the existence of E_{PZ} and

makes the lowest conduction band minima at the InGaN/AlGaN interface and the highest valence band maximum at the GaN/InGaN interface. This is the Quantum Confined Stark Effect discussed in 2.3.3.4, which induces a smaller effective bandgap or a redshift of the emission with respect to flat band conditions.

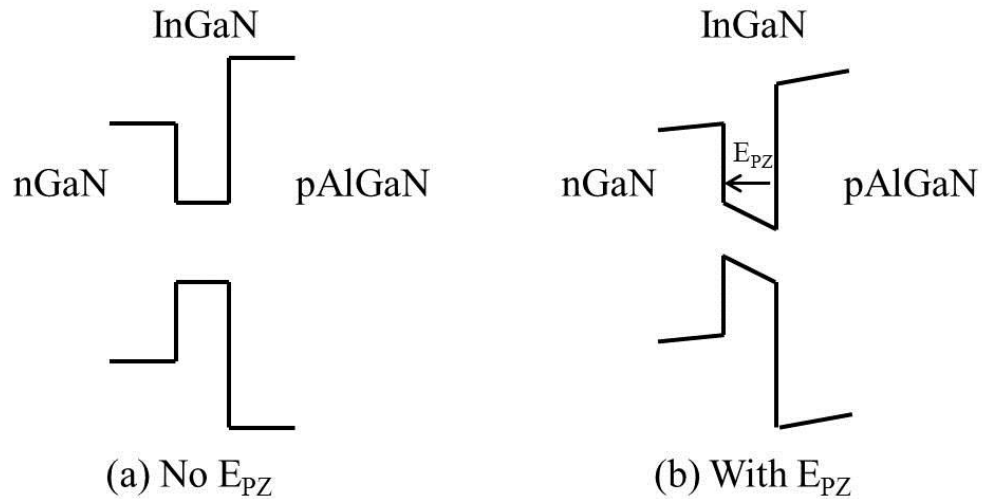


Figure 2.13: Schematic of the band structure of an InGaN SQW structure (a) without and (b) with PZ effects

The magnitude of the shift is dependent to the strength of the field and to the layer thickness. When an external bias is exerted on the material as shown in Figure 2.14 (b), a decrease in the internal piezoelectric field is resulted, which leads to an increase in effective bandgap or a blueshifted emission spectrum. When the bias increases, the cancellation of the PZ field will occur as flatband conditions are reached and a further increase inverts the bands and leads to a decreased effective bandgap or a redshifted emission spectrum. When additional carriers are injected into or generated in the quantum well by increasing the forward bias or photon/electron beam excitation as shown in Figure 2.14 (c), the additional carriers would accumulate at the local energy minima

and results to separation of charge, which builds up a screening electric field against the PZ field. When additional carrier concentration increases, the internal PZ field decreases and leads to an increased effective bandgap or a blueshifted emission spectrum. Similarly, when increase the injected or generated carriers, a cancellation of the PZ field takes place until flatband conditions are reached.

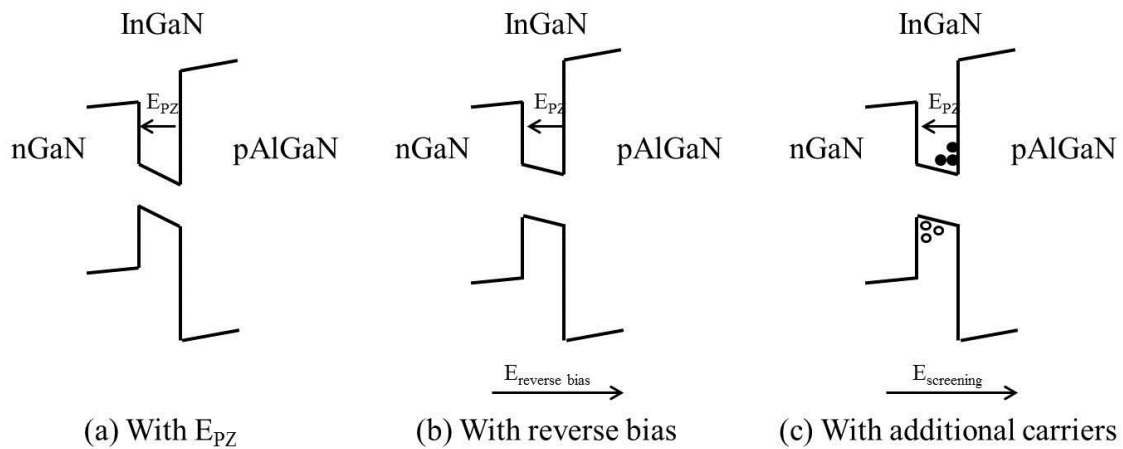


Figure 2.14: (a) Schematic of the band structure of an $\text{In}_x\text{Ga}_{1-x}\text{N}$ SQW with the PZ field, (b) the effects of applying a reverse bias on the band structure, and (c) the effects of additional carriers in the quantum well on the band structure. [16]

2.3.5 Defects and the Effects

Different kinds of defects exist in the InGaN/GaN MQW LED heterostructure grown by MOCVD, including point defects, dislocations, epitaxial defects, stacking faults and inversion domains.

Point defects include C and O impurities, Ga and N vacancies, Mg-H complexes, and so on. They form interband impurity levels and cause yellow luminescence of GaN.

Dislocations are divided into two categories: misfit dislocations and threading dislocations. Misfit dislocations are those which confined within the bulk GaN epi-layer

and are not expected to propagate through the layer thickness. They are one of the most efficient strain relieving mechanisms. Threading dislocations, on the other hand, thread up into the layer to the film surface if not merged with each other. Also, threading dislocations can be interconnected to misfit dislocations [17]. TEM investigations have been done by others and proven that most threading dislocations originated at the GaN/substrate interface propagates to the surface [18]. Threading dislocations are divided into three groups: edge dislocation, screw dislocation, and mixed dislocation [19]. The small angular deviations about the $[0\ 0\ 0\ 1]$ axis are relaxed by edge dislocations (a-type), while deviations resulting from overgrowth steeped substrate surface by screw dislocations (c-type). Non-pure edge or screw dislocations are of mixed dislocations type and are called c+a type. As a consequence of the large differences in thermal expansion coefficients, lattice constants, and chemical characteristics between GaN and sapphire, high density of dislocations are formed in the GaN or AlN low temperature buffer layer grown on the sapphire substrate, and continue into InGaN/GaN MQW active layer on top, which will be discussed in detail later. In GaN on sapphire structure, threading dislocations and mixed dislocations are the two major dislocation types.

Epitaxial defects, such as V-pits, nanopipes and voids are formed mechanically during the growth process.

The planar defects that exhibit different stacking order are defined as Stacking faults. They occur where the normal ABABAB or ABCABC stacking sequences are disrupted. They most often form in the region immediately adjacent to the substrate where the low crystal quality GaN or AlN buffer layer are grown.

Epitaxially grown GaN can be Ga- or N-polar. Most high quality MOCVD GaN films

are Ga-polar. Inversion domains in a material are formed where the polarity domains are reversed. This can happen when N-polar domains are grown on top of Ga-polar material or on free surface of an otherwise Ga-polar film.

GaN-based optical emitters with dislocation densities of 10^8 to 10^{10} cm^{-2} can work efficiently, while it is common knowledge that a dislocation density of 10^4 cm^{-2} is enough to kill GaAs-based LEDs. This arise questions that do the dislocations act as nonradiative recombination centers? If they do, why don't they reduce the light emission efficiency of the LEDs? Therefore, the influence of defects on LED structures leads to big controversy. A great many studies [20] to [50] have been done to investigate the optical and electrical properties of the defects on GaN and InGaN/GaN MQW structures grown by MOCVD. A summary is shown in Table 2.1. However, the debate is still continuing, and there are still some new and interesting studies can be done to further study the influence of defects on the LED heterostructure.

Table 2.1: reported studies of the effects of defects on the optical and electrical properties of GaN and InGaN/GaN MQW LED structures grown by MOCVD

Effects?	Optical Properties	Electrical Properties
Yes	<ul style="list-style-type: none"> -EDs decrease PL intensity.[20] -TDs and pits are NRRCs. [21] -Screw and mixed dislocations are NRRCs. [31][32] -EDs are NRRCs. [33] -V-pits affect luminescence due to the absence of QW growth on the pit facets. [32][35] 	<ul style="list-style-type: none"> -negative charges existing near TDs scatter the carriers and introduce deep-level states. [20][40][46] -Oxygen impurities, nitrogen vacancies, Mg-H complexes, and structural defects cause deep level traps in LEDs and lead to carrier tunneling. [32][47][48] -There are acceptor- and donor-like traps around screw TDs. [49]
No	<ul style="list-style-type: none"> -EDs are optically inactive. [31][32] -Dislocations and V-pits cannot act as efficient NRRCs. [36][39] 	<ul style="list-style-type: none"> -Bandgap states associated with TDs and V-pits are not electrically active. [37][50]

CHAPTER 3: MOCVD PROCESS OF INGAN/GAN MQW LED STRUCTURES

3.1 MOCVD Theory

Various techniques have been implemented for epitaxial growth of III-N thin films. However, of all the techniques employed, MBE and CVD techniques have been adopted most commonly for the growth of III-N thin films.

For the growth of III-N based optoelectronic devices, MOCVD has been the predominant growth technology due to the application in growing various III-V materials with good control on single layer thickness, interface abruptness, surface uniformity, and the ability to deposit heterostructures in a single experiment and highly controlled p- and n-doping of individual layers. Initially, MOCVD was defeated by MBE in its real time in-situ monitoring. Today, most MOCVD chambers are equipped with advanced in-situ monitoring tools that provide metrology of growth surface.

The use of the terminology MOCVD was originally reported by Manasevit. Alternative nomenclatures have been used since then such as OMVPE (organometallic vapor phase epitaxy), OMCVD (organometallic chemical vapor deposition), OMP (organometallic pyrolysis) and MOVPE (metalorganic vapor phase epitaxy). Same idea has been conveyed in these nomenclatures that the vapor form of the organometallic compound materials are transported chemical species to the heated reaction zone. The

nuances of the techniques are governed by precursor type, reactor pressure, system design details and methodology used in mixing of chemicals in the gas flow and nature of the carrier gas.

Even though complex reaction paths may exist, the fundamental chemical reaction taking place in an MOCVD chamber for the growth of III-V can be represented by:



where III represents the group III elements, V the group V elements, and A the organic compound which the group III element is attached to, an Alkyl in most cases. And thus, for the epitaxial growth of GaN, TMG and NH₃ are used:



Note that the above equations represent the overall reaction path, and does not include any intermediate steps that occur in the chamber such as pyrolysis of alkyls, cracking of NH₃, formation of adducts and other parasitic reactions etc.

The metalorganic precursors, in liquid or solid form, are introduced into the reaction chamber via a carrier gas passing through a bubbler, the container for the precursors. The carrier gas is typically N₂, H₂ or a mixture of the two, depending on the alkyl species being transported and the growth conditions of the specific layer. The molar flux of a metalorganic delivered to the reactor, F_{MO} , is a function of bubbler equilibrium vapor pressure of the metalorganic, P_{MO} , the pressure on the bubbler, P_B , and the molar flow rate of the carrier gas, F_C , as given below [5]:

$$F_{MO} = \frac{P_{MO}}{P_B} F_C, \quad (3-3)$$

The metalorganic equilibrium vapor pressure, P_{MO} , is decided by bubbler temperature and pressure. The equilibrium vapor pressure of a metalorganic at a given temperature is tabulated by vendors. The bubbler temperature is controlled by placing the bubblers in chiller baths with temperature controller. P_B is controlled by a pressure controller installed on the outlet of the bubbler.

The molar flow rate of the carrier gas can be calculated in accordance with the Ideal Gas Law as [5]:

$$F_C = \frac{P_A \cdot V'}{R \cdot T}. \quad (3-4)$$

In equation 3-4, P_A is the atmospheric pressure, V' is the carrier gas volumetric flow rate, R is the gas constant and T is the standard temperature.

Therefore, the growth rate and composition of epitaxial film can be controlled precisely by bubbler temperature and pressure, and the flow rate of the carrier gas.

3.2 Veeco TurboDisc K465i MOCVD System

The samples studied and discussed in the present work was grown by using a Veeco TurboDisc K465i GaN MOCVD reactor. The reactor is comprised of gas delivery system, sources and precursors, resistively heated reaction chamber and an exhaust system. This section is dedicated to briefly describing the aforementioned components of the reactor.

The reaction chamber is of vertical flow rotating disk configuration, in which the precursors and the carrier gases are flowed vertically onto the substrate as seen in Figure 3.1. The substrate wafers are loaded into the chamber within the pockets of SiC coated graphite platters as seen in Figure 3.2. The platter is rotated typically between 500 to 1200 rpm during the epitaxial growth by a spindle connected to a motor to ensure thermal and chemical uniformity across the platter.

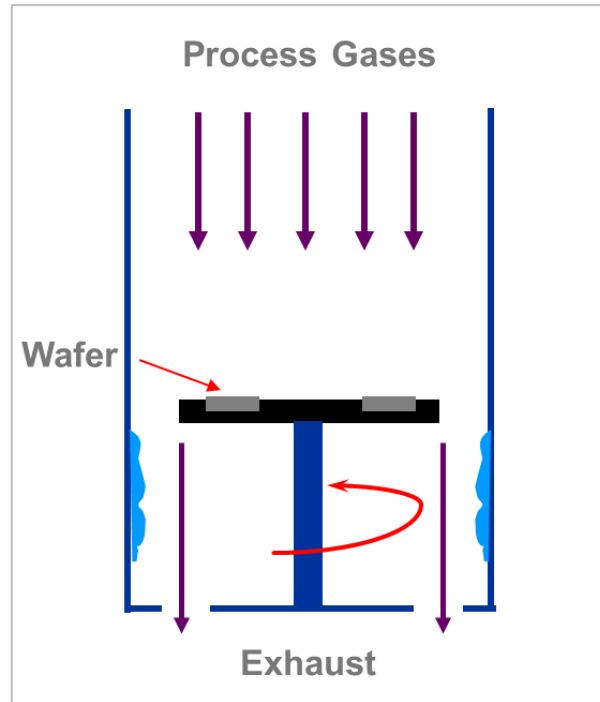


Figure 3.1: The schematics of vertical rotating disc growth chamber

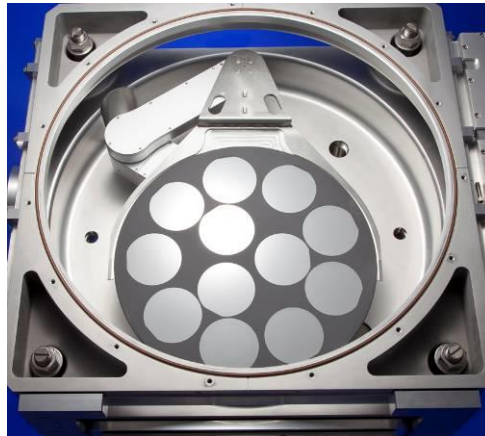


Figure 3.2: 12x4" SiC Coated Graphite Platter loaded with sapphire wafers

The process gases are introduced into the chamber through the Uniform Flow Flange® [51], Figure 3.3, designed to maintain laminar gas flow while minimizing buoyancy and recirculation effects. The flange has separate alkyl and hydride slits to

circumvent premature gas phase reactions. The use of two separate paths until the reaction zone is critical since the alkyl sources (group III precursors) are Lewis acids; whereas ammonia, the primary group V source, is basic. Therefore, the pre-mixing between the two species will lead to gas-phase reactions, i.e. premature parasitic reactions, which are detrimental to the film growth process [51].

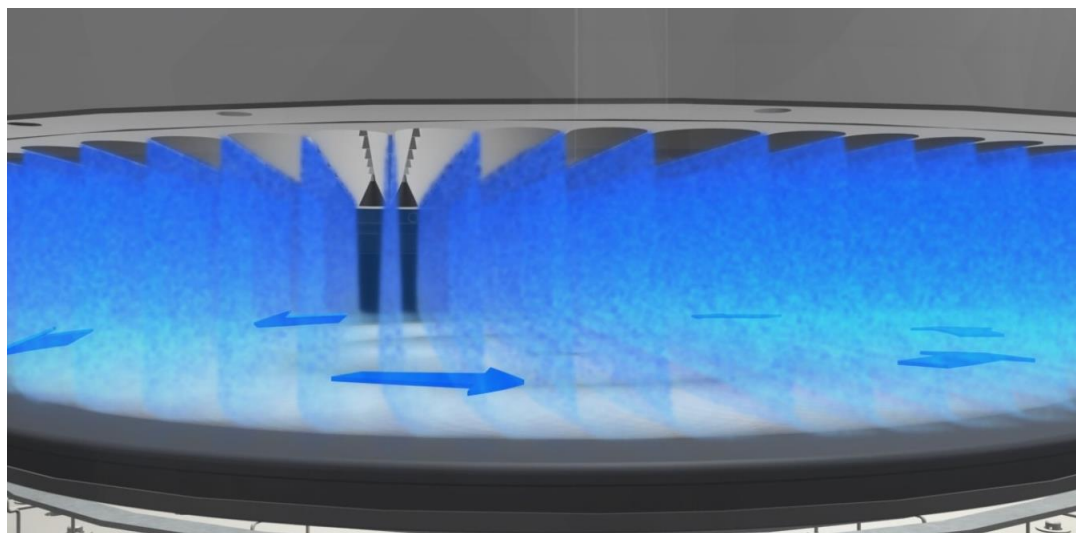


Figure 3.3: The schematic cross section of the Uniform Flow Flange® with separate alkyl and hydride slits. The blue dots represent the pathway for the hydrides, while red dots represent pathway for alkyls

The chemical species that are not consumed in the epitaxial growth reactions (excess precursors, by-products, carrier gases etc.) is pumped out through the exhaust by two Ebara pumps placed downstream the growth chamber, shown in Figure 3.4.



Figure 3.4: Ebara process pumps

The Veeco K465i MOCVD growth chamber is equipped with in-situ measurement equipments RealTemp200® Emissivity-Corrected Pyrometer and DRT210® integrated deflectometer, reflectometer, pyrometer. This set-up enables in-situ monitoring of key epitaxial growth metrics including reflectivity of the wafer, temperature of the wafer and the platter, wafer curvature and epitaxial growth rate during the run. The heating of the platter is done via 3 filament resistive heating and the temperature control is achieved by 3 zone closed loop temperature control.

3.3 Epitaxial Process

The typical InGaN/GaN MQW LED heterostructure grown by MOCVD system is shown in Figure 3.5. C-plane, or (0001) plane, sapphire wafer is used as the substrate. Several GaN layers are grown under different growth conditions to help with the nucleation of relatively high quality n-type GaN layer. n-type GaN layer is usually thick to maintain good crystal quality. InGaN/GaN MQW are grown as the active layer of the

LED heterostructure. The thickness of the InGaN wells is around 2.5nm, and 130nm for GaN barriers. Indium composition is about 14% to achieve blue emission around 460nm. Then p-type AlGaN electron blocking layer and p-type GaN layer are grown respectively to form the pn junction.

80nm pGaN
30nm pAl _{0.18} Ga _{0.82} N
4-8 pairs of 2.5nm In _{0.14} Ga _{0.86} N/13nm GaN MQW
2-5um nGaN
1um uGaN
1um uGaN recovery layer
200nm HP GaN roughening layer
25nm HP LT GaN nucleation layer
C-plane Sapphire Substrate

Figure 3.5: Schematic of a typical InGaN/GaN MQW LED structure grown by MOCVD

3.3.1 C-plane Sapphire Substrate

Even though large differences in the lattice constant and thermal expansion coefficient exist between III-Ns and Al₂O₃, sapphire is extensively used as the substrate material due to its high-temperature stability, physical robustness, and availability at a relatively low cost. In our structure, (0001) direction or c-plane sapphire substrate is used. The AFM image in Figure 3.6 shows the surface morphology of the sapphire substrate, which is very smooth with a RMS roughness less than 0.2nm. Before epilayer growth, the sapphire substrate is ramped up to 1070°C in H₂ atmosphere for in-situ

cleaning process. The cleaning process lasts 5-10min and helps achieve clean surface for crystal growth.

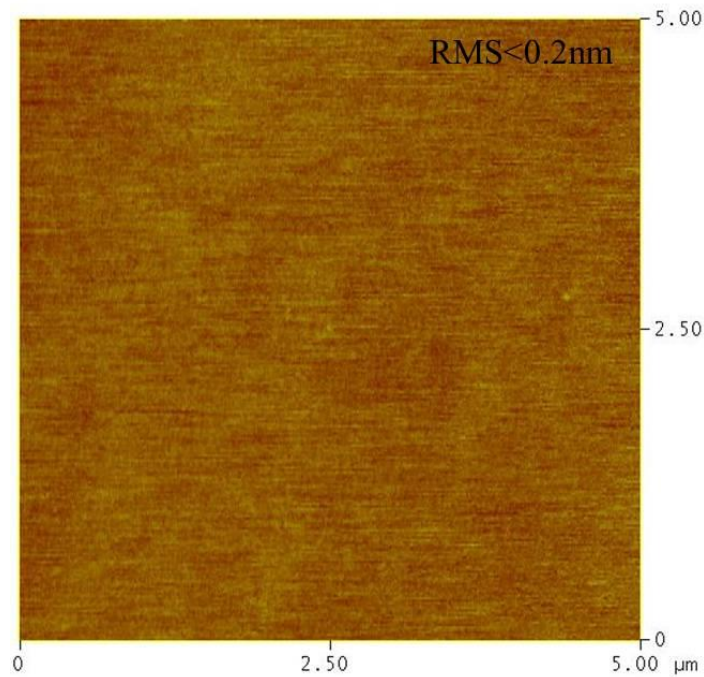


Figure 3.6: AFM image of c-plane sapphire substrate

Several works [52][55] have been done to study the LED structures grown on vicinal c-plane sapphire substrates, which are the misoriental sapphire wafers with their c-axis offset by a small angle. According to these studies, the LED structures grown on misoriented sapphire substrate show reduced point defect densities by giving suppressed yellow luminescence, show sharp layer interfaces and uniform QW period by giving clearer XRD curves, and show higher EL intensities. It has also been reported that LED structures fabricated on the 0.2 degree off substrates exhibits better material quality, lower dislocation density, and stronger EL intensity than the other misorientation angles for 20% in composition InGaN/GaN MQW LED.

Some other works [56][59] have been done to study the LED structure grown on c-plane patterned sapphire substrates, or PSS, considering the possibility of enhancing light extraction from multiple scatterings. Those works show that LED structures grown on PSS exhibit reduced dislocation density, increased IQE, higher extraction efficiency shown in Figure 3.7 and higher EL intensity.

For the studies in this dissertation, 0 degree off un-patterned sapphire substrate was used.

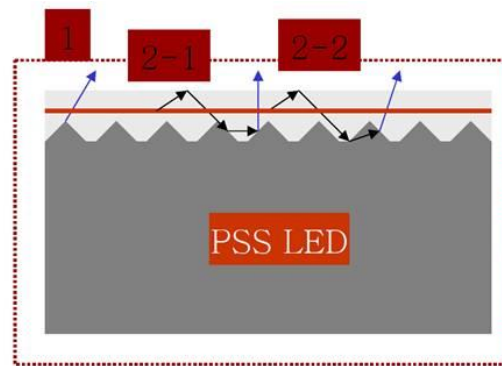


Figure 3.7: schematic of light extraction from LED grown on PSS

3.3.2 GaN Nucleation Layer

After the sapphire substrate cleaning process, GaN nucleation layer is grown at 550°C and 500torr to wet sapphire surface, achieve 2 dimensional growth and give smooth surface. TMGa and ammonia are used as the source materials of Ga and Nitrogen. AFM image in Figure 3.8 shows that GaN nucleation layer is pretty rough with a RMS roughness around 2nm.

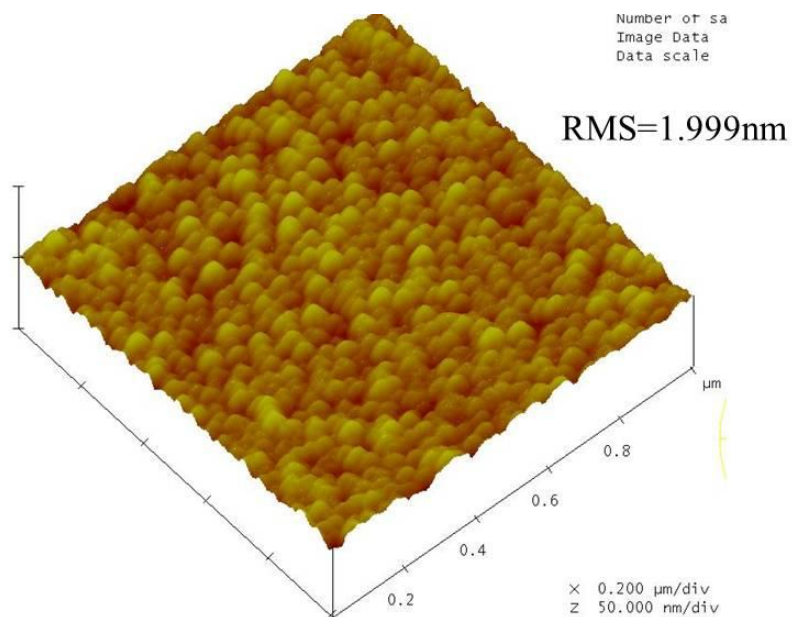


Figure 3.8: AFM image of GaN nucleation layer

Nucleation layer has a rough morphology and a high degree of stacking disorder with mixed (111) cubical and (0001) hexagonal structures, as shown in Figure 3.9. This stacking disorder is a consequence of the low nucleation layer growth temperature and high supersaturation of the MOCVD precursors in the vapor phase [60].

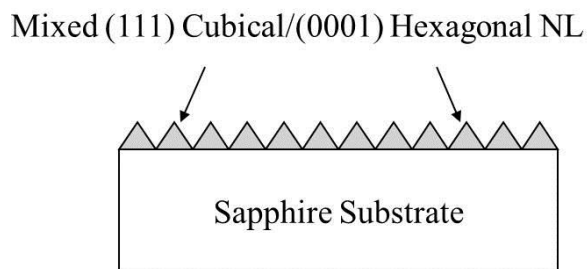


Figure 3.9: Schematic of GaN nucleation layer

3.3.3 3D GaN Roughening Layer

Then GaN roughening layer is grown at 1000-1050°C and 500torr. 3 dimensional

GaN islands are formed and they improve crystal quality by filtering dislocations out.

XRD data of uGaN structure grown with and without roughening layer are shown in Table 3.1. It shows that smaller XRD curve FWHM for (002) plane ω scan, (002) plane $\omega 2\theta$ scan, and (102) plane $\omega 2\theta$ scan, which indicates that uGaN structure with roughening layer exhibits lower dislocation density and better crystal quality.

Table 3.1: XRD data of uGaN structure grown with and without roughening layer

		FWHM (arc sec)
uGaN with 3D roughening layer	002- ω	208.4
	002- $\omega 2\theta$	155.3
	102- $\omega 2\theta$	231.8
uGaN without 3D roughening layer	002- ω	242.0
	002- $\omega 2\theta$	183.5
	102- $\omega 2\theta$	548.4

Cross-section TEM micrographs for a series of samples with GaN thickness of 0Å (a), 250Å (b), 500Å (c), 1000Å (d), 2000Å (e), and 4000Å (f) on NL have been taken and studied by others [60]. In the initial stages of growth, the 3 dimensional islands form. The free surface of the islands consists of (0001) and (10-11) facets. With progressive growth, the islands coalesce. After about 4000-5000Å of high temperature growth, the layer is fully coalesced with a smooth (0001) surface. Typically, the islands have one or a few

mixed or screw dislocations. In regions where islands have coalesced, the edge and mixed dislocations form. When dislocations reach the (10-11) facets of the islands, the propagation direction will change and the dislocations will propagate laterally and thus will not thread through the whole epitaxial structure, as shown in Figure 3.10 [40][61].

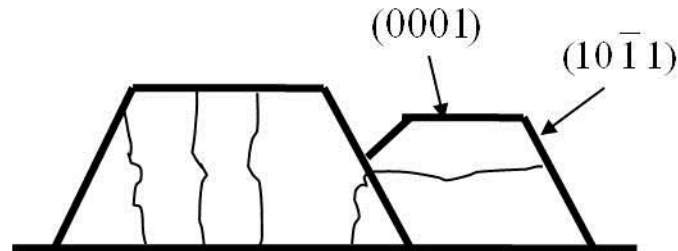


Figure 3.10: Schematic of the coalesced 3D islands

3.3.4 GaN Layers

Then 1 μ m undoped GaN recovery layer is grown to fully coalesce the 3D islands as discussed in 3.3.3. Another 1 μ m uGaN layer and a 2 to 5 μ m n-type GaN layer are grown after that. These GaN layers are all grown at 1050 to 1100°C and 200torr condition. TMGa and ammonia are used as the source materials of Ga and Nitrogen. Silane is used as the n-type dopant source. The AFM image in Figure 3.11 shows the surface morphology of n-type GaN layer. Terrace lines are clearly observed and the surface roughness is around 0.2nm.

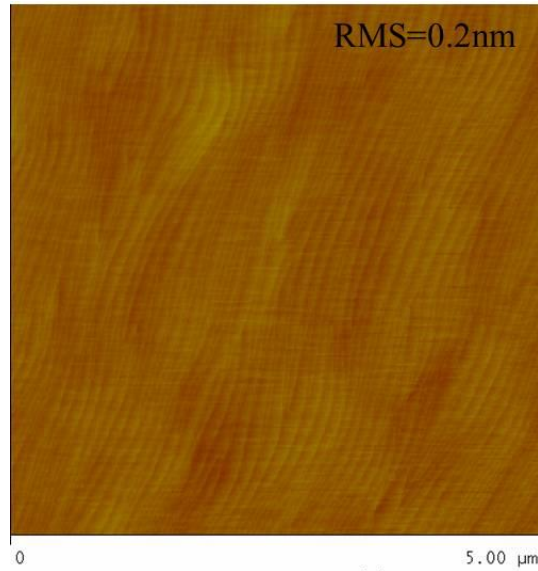


Figure 3.11: AFM of nGaN layer

The reported cross section TEM image on GaN layer [62] shows that above 0.5 μm from the substrate/GaN interface, the dislocations are independent, straight and perpendicular to the surface.

A SCM combined with AFM study on GaN layer has been published [40]. The 2.5 μm by 2.5 μm AFM superposed with contrast reversed SCM image has been shown. A high density of large and small surface pits was observed. It is observed that the regions around dislocations exhibit smaller dC/dV than the dislocation free regions do. A positive voltage shift is observed in the C-V curve of the regions in the vicinity of the dislocations, which indicates that there are negative charges accumulating near the threading dislocations in GaN. The authors reported several possibilities for this negative charge, including the presence of deep acceptor-like trap states, segregation of charged impurities, and piezoelectric fields associated with the strain fields surrounding dislocations.

3.3.5 InGaN/GaN MQW Active Layer

Then the InGaN/GaN MQW active layer is grown at 760°C and 200torr. It confines carriers and generates light emission through recombination. TEGa, TMIIn and ammonia are used as the source materials of Ga, In and Nitrogen, respectively. MQW layer is grown at lower temperature due to the high volatility of indium at high temperature. The AFM image in Figure 3.12 shows the MQW structure surface morphology. Pits are observed.

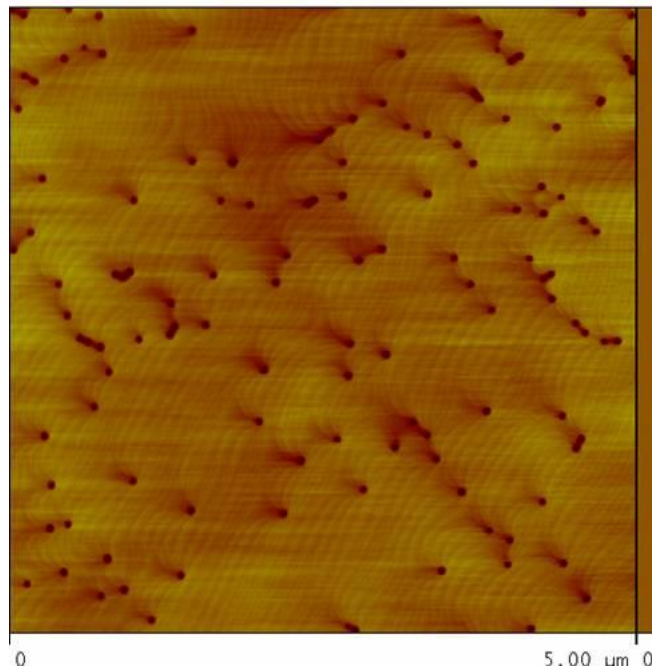


Figure 3.12: AFM of InGaN/GaN MQW layer

This pit is a frequently observed defect in InGaN/GaN MQW, which is an open hexagonal inverted pyramid and the walls of the inverted pyramid are $\{10\bar{1}1\}$ planes [34]. It is named V-pit because from a cross-section TEM view, it shows as the shape of an open V, shown in Figure 3.13. The non-planar V-pits walls are likely to result in In

composition variation through the MQW. V-pit originates at a threading dislocation, an inversion domain, or stacking mismatch boundaries [20][32]. Several suggestions have been made to explain the formation of such V-pits, including strain relaxation, low adatom mobility on the InGaN surface, indium segregation congregated in dislocation core areas and/or decreased Ga incorporation on the $\{1\ 0\ -1\ 1\}$ planes compared with (0001) surface [34][35][63][64]. V-pits are found to worsen quantum barrier/well and MQW/GaN interface abruptness that deteriorate the device performance [65].

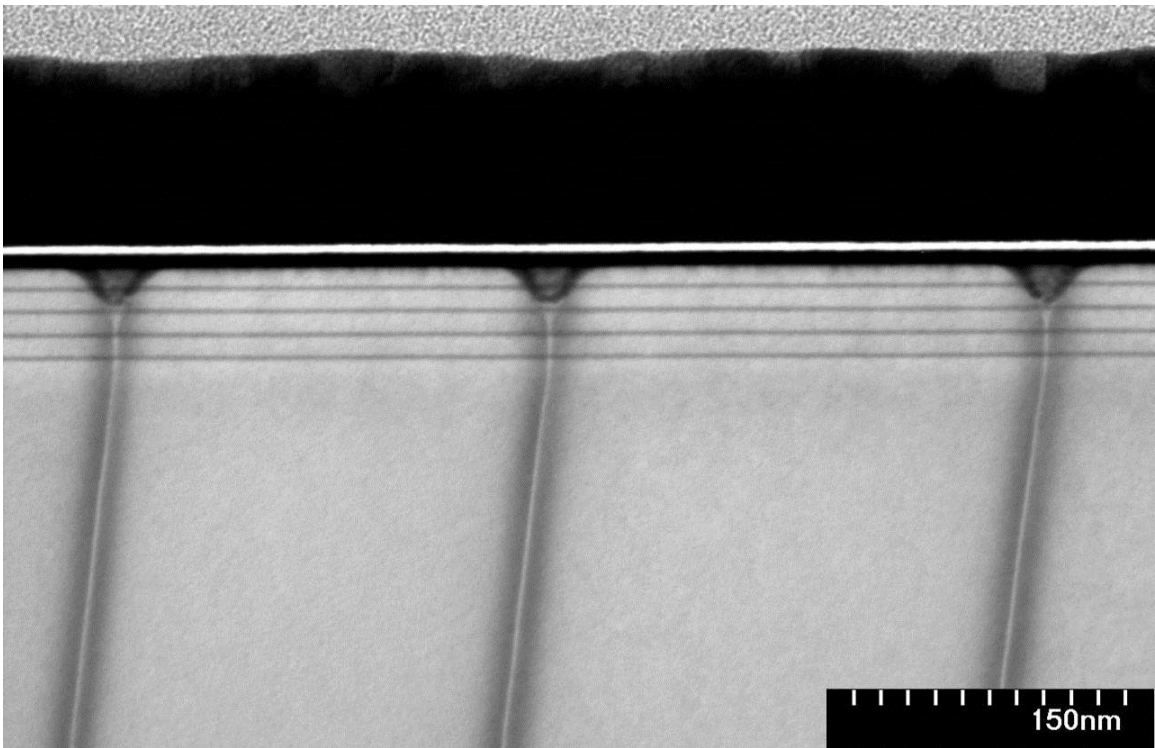


Figure 3.13: Cross section STEM image of V-pit on InGaN/GaN MQW

Also, it has been published by others that the formation of V-pit is related to the pair number of MQW [34], and the AFM images of a series of MQW structures with various numbers of well-barrier pairs are shown. A pit-free AFM image of the bulk n-type GaN

layer prior to the MQW growth with terrace was observed. After the 2nm 32% indium composition QW was grown, island morphology was observed. Still, no pit was observed. After the single InGaN QW is capped by the 7nm GaN barrier layer, the island morphology disappeared, and the surface was flattened. After the growth of three MQWs, pits were observed. After five pairs of MQW growth, the pits got larger in size but the density was same. After capping the MQW layer with a 300nm AlGaIn layer, the pit density decreased, and the pits became smaller in size, which is because the pits have been filled by AlGaIn capping layer, and we will discuss this later in 3.3.6.

CL studies have been done on the InGaN QW layer associated with TEM [23][33]. Plainview TEM image and corresponding CL map at 460nm are shown. It is reported that dislocations and V-pits don't contribute to the band edge emission of QW. However, there are many work published discussed about the possibility of in rich inclusions on the V-pit side walls cause the red shifted emission [66], or the formation of thinner MQW structure on the side walls causes it blue shifted [67][68].

It also has been reported that the MQW emission is decided by both the compound composition and the defects. Multiple CL peaks have been observed which is suggested to come from stacking faults [69].

3.3.6 p-AlGaIn Electron Blocking Layer

Following MQW growth, 30nm p-type AlGaIn layer is grown at 950°C and 100torr to block electrons overflow to p-region. TMA is used as the source material of Al. CP₂Mg is used as the p-type dopant source. Surface morphology of P-AlGaIn on MQW, in Figure 3.14, shows a decreased pit density as we mentioned before.

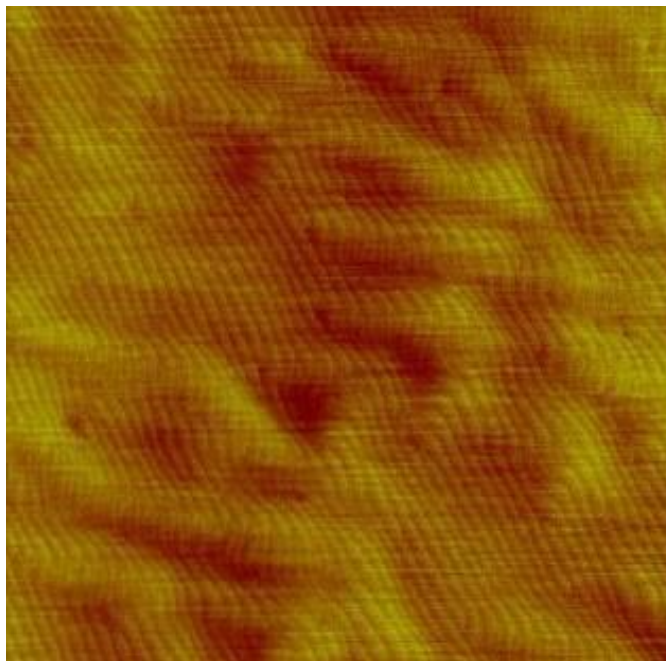


Figure 3.14: 5um by 5um AFM of p-AlGaN capped MQW structure

It has been reported that p-AlGaN cap layer grown at higher temperature increases the surface mobility of adatoms, and partially fills the V-pits [35] as shown in Figure 3.15.

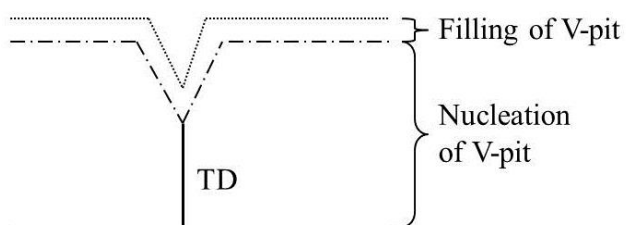


Figure 3.15: Schematic of the filling of V-pit

3.3.7 p-GaN Layer

At last, 80nm p-type GaN layer is grown at 950°C and 200torr. Cp_2Mg is again used as the p-type dopant source. A typical fish bone like surface morphology is observed for

p-GaN layer, shown in Figure 3.16.

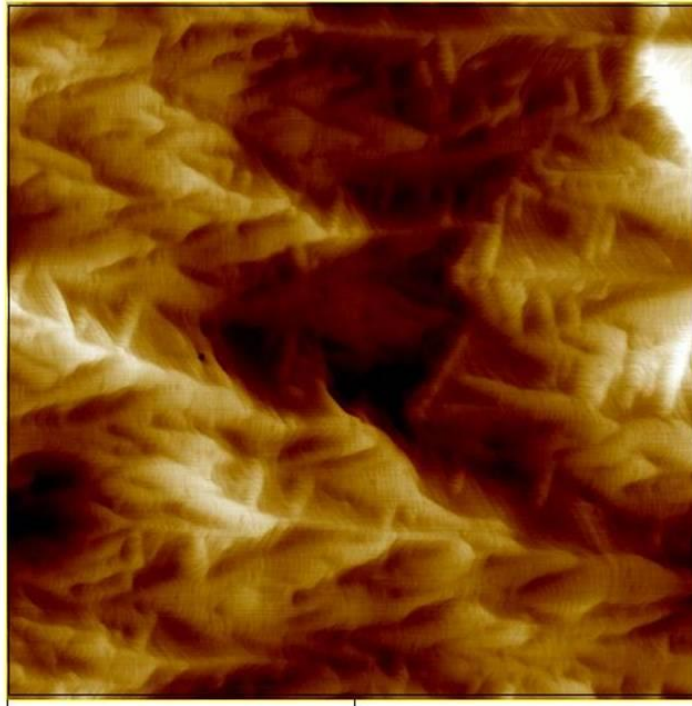


Figure 3.16: 5um by 5um AFM of the full LED structure

Cross-section TEM studies have been done on the full LED heterostructure and show that the V-pits formed both on the top surface and beneath it [32].

CHAPTER 4: SEM-CL TECHNOLOGY

SEM-CL is a nondestructive technique allows spatially resolved observation and characterization of semiconductor materials. Measurement of embedded layers and interfaces is achieved by tuning the electron beam energy and keeping the generation rate of e-h pairs constant. By using this technique, CL spectra and luminescence images can be captured at multiple locations on the sample. Besides, SEM-based CL systems can provide information on the density and behavior of luminescent and non-luminescent features.

4.1 Electron Interaction in Semiconductor

Luminescence emission from a semiconductor is resulted from the recombination of e-h pairs which can be generated by an electron beam or incident light. When light is used as the excitation source, i.e., PL, only one e-h pair is generated by every photon. However, when electron beam is used as the excitation source, e-h pairs are not generated by incident electrons directly. Instead, it induces the X-ray emission by an innershell excitation process, the electron emission by an Auger effect, the secondary electron emission by a cascade process, and so on. Because the Auger electrons generation is a cascading phenomenon, the number of Auger electrons generated is markedly more than the number of incident electrons. Meanwhile, the collision between an incident electron

and a valence electron gives out secondary electron emission, which also increases in number. As a result, every incident electron in the cascade process generates about 1×10^3 secondary electrons, despite that the ratio of the Auger effect to the collision process is not precisely determined. In the case of the electron beam of few keV energy used in SEM in the present work, the X-ray emission by the inner-shell excitation process is inferior to the electron emission by the Auger effect. [70]

Figure 4.1 shows a schematic illustration of the cascade process caused by electron beam [70]. The electrons diffuse in an almost spherical volume. The depth and diameter of the diffusion region are nearly equal, and the depth is given by:

$$D = \frac{0.0276A \cdot E^{5/3}}{\rho \cdot Z^{8/9}}, \quad (4-1)$$

where A , Z , ρ , and E are the mass number, the atomic number, the volume density in g/cm^3 , and the acceleration voltage of the EB in keV, respectively [70].

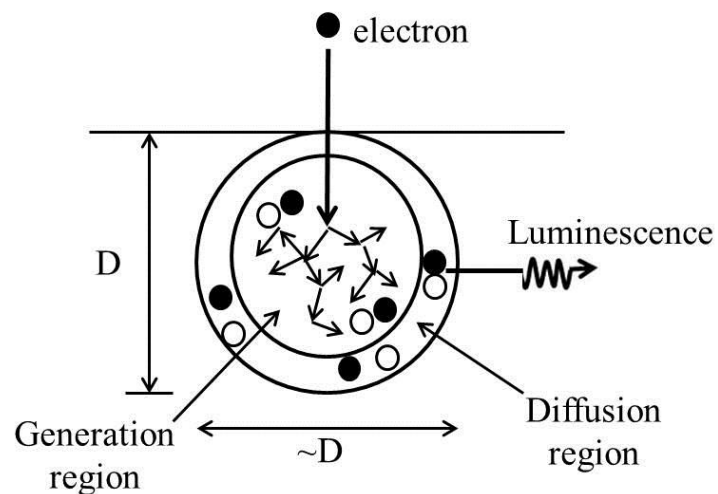


Figure 4.1: Schematic of electron cascade process

4.2 SEM

The initial SEM configuration used to examine the surface of bulk specimens was set up in 1942, which contained many of the basic principles used in the design of today's SEMs. A resolution of 50 nm was achieved with this SEM. However, further development in the SEM slowed down since the advancement was not as profound compared to the performance of the developing TEM. Not until 1948 the SEM was investigated again. By 1952, SEM systems of a resolution of 50 nm were built up. A number of improvements have taken place in the SEM since the first prototype resulting in an improvement in resolution from 50 nm down to ~0.5 nm today. [16]

A basic SEM column includes an electron gun, electron lenses, one or two condenser lenses, an objective aperture, and an objective lens. The electron gun generates a source of electrons and accelerates the electrons to 1-30 keV under vacuum from 10^{-4} to 10^{-10} Torr. The electron lenses demagnify the image of the gun crossover and focus a spot on the specimen on the order of 1nm-1 μ m with a beam current in the range of 1pA-1 μ A. The condenser lens controls the demagnification. The objective lens focuses the final probing on the specimen. The lens and aperture system in the column control the beam diameter, beam current, and convergence angle. These three parameters can be adjusted to achieve high depth-of-field, high-resolution, or high current density. A small convergence angle is required for high depth-of-field imaging and can be achieved by either using a small objective aperture or operating at a long working distance. High resolution imaging needs a small beam size which can be provided by a strong condenser lens, an objective aperture, and/or a short working distance. [16]

Secondary electron (SE) detector is standard equipment in all SEMs and is used in the

present work. The signals come from interactions of the EB with atoms at or closely beneath the sample surface. In general, SE-SEM can generate very high-resolution images of a sample surface, smaller than 1nm.

4.3 CL

Cathodoluminescence is conducted by recombination of EB generated e-h pairs. There are several ways for primary electrons to lose their energy to generate e-h pairs, including exciting plasmons, valence, and inner shell electrons and phonons. Plasmons can decay into excitons. Valance electrons can be excited by Auger electrons, photoelectrons, and x-rays, and then e-h pairs are generated during the excitation process. Phonons assist in indirect electronic transitions. [71]

It was in the middle of the 19th century that the CL phenomenon was first reported, during experiments on electrical discharges in evacuated glass tubes. Luminescence was observed when cathode rays struck the glass tubes. The observation of luminescence due to cathode ray bombardment led to the discovery of the electron in 1897. Today, CL is widely used in instruments such as oscilloscopes, televisions, and electron microscope fluorescent screens. [16]

A great many efforts have been put into developing techniques to observe localized luminescence properties in semiconductors due to their importance in studying semiconductor physics and optoelectronic devices. CL is a powerful tool for this purpose because of its capability of carrying out experiments of large scanning areas and short total measuring time. By scanning a large area of the sample with electron beam, any point on the sample can be measured easily compared with using piezo-driving devices. Besides, since the excitation intensity of an electron beam is significantly larger than that

of laser, high luminescence intensity can be achieved by CL technique. The high intensity allows decreasing exposure time and thus faster response. Moreover, by controlling the electron beam diffusion depth into the semiconductor structure, a depth dependent luminescence study can be executed.

CL analysis performed with an SEM can be divided into microscopy and spectroscopy. In CL microscopy, luminescence images or maps of areas of interest are obtained by a scanning or parallel beam. In panchromatic CL imaging the combined intensity of all CL wavelengths within the response of the detector are used to create the image. In monochromatic CL imaging, the light is coupled into a monochromator and CL images can be created from a selected wavelength bandpass. In CL spectroscopy, a spectrum is obtained in rastering mode or spot mode.

4.4 Previous Studies on the Effects of Electron Beam on GaN Based Structures

The LEEBI effects on the optical properties of GaN based structures have been studied by plenty of researchers and groups. A decrease in luminescence intensity followed by an increase in GaN emission was observed under EB excitation [72][76]. Contradictory discussions about the cause of this effect on the GaN luminescence have been published, including trap formation [73], trap filling [75], stimulated diffusion of point defects [74] or of O and H [72][78], and strain release [74]. The decreased GaN CL intensity was also explained by surface modification [76] and surface carbon contamination [78] stimulated by the LEEBI.

Several investigations also devoted to LEEBI effect on the optical properties of InGaN/GaN quantum well structures. It is reported by others that after the LEEBI treatment at 5 and 300 K, an increased MQW CL intensity with a blue shifted emission

band were observed, which was suggested to be caused by change of internal electrical field happened during the activation of hydrogen-passivated acceptors and donors [77][79]. CL and EBIC investigations have been applied to show that irradiation of the InGaN/GaN QW structure by low energy electrons (10keV EB voltage at $1.5\text{c}/\text{cm}^2$ does) lead to the formation of a new InGaN related emission band that was blue shifted to the original band. Increased InGaN luminescence intensity followed by the decrease was observed. The maximum luminescence intensity was reached at exposure does of a few c/cm^2 . It is explained and reported that the LEEBI resulted in local In composition variation attributed to In or Ga recombination enhanced diffusion, which caused the effects on the CL spectrum. Some quantum dot like structures, therefore, were probably formed as a consequence of EB exposure and thus new emission bands were excited [80]-[84]. A decreased InGaN luminescence intensity after extended LEEBI was explained by the accumulation of hydrocarbons on the sample surface. Also, it has been discovered that the newly formed blue shifted peak is Gaussian broadened, while the original InGaN emission is Lorentzian since it is known that excitonic effects can increase oscillator strength at the band gap energy and remarkably decrease emission line widths [85].

However, it has also been reported that InGaN material is extremely sensitive to high energy EB irradiation between 200 and 400 keV used in TEM [86]. Under only a short period of such irradiation, EB causes molecular damage, and leads to inhomogeneous strain in the material, which exhibit similar feature as InGaN nanostructure compositional in homogeneities and can be falsely interpreted as local In clustering in TEM images.

CHAPTER 5: EXPERIMENTS DETAILS

5.1 Sample Description

A designated aforementioned Veeco K465i MOCVD system has been used for all the studies involved in the present work.

Depending on whether a 5 x 6", 14 x 4", or 45 by 2" carrier has been used for the process, each set of samples include 5 pieces of 6" wafers, 14 pieces of 4" wafers or 45 pieces of 2" wafers. All wafers from the same carrier/run are expected to have same properties within acceptable standard deviation.

To study the properties of the InGaN/GaN MQW LED as-grown structures layer by layer, the process has started from the sapphire substrates, and stopped: i. after bulk nGaN layer (marked as "4"), ii. after MQW layer (marked as "3"), iii. after p-AlGaIn layer (marked as "2"), and iv. after the whole LED structure (marked as "1") have been grown, respectively. The repeated existing layers, therefore, should exhibit similar properties in different samples. The lists of sample naming are shown in Table 5.1.

Table 5.1: Naming rule of sample structure

	1	2	3	4
Structure	LED	p-AlGa _N capped MQW	MQW	Bulk Ga _N

To study the possible growth condition dependent properties of respective samples from 1, 2, 3, and 4, different set of samples were grown with slightly changed growth temperature, marked as A, B, and C. Some layer thickness, dopant concentration and MQW pair numbers also vary among A, B, and C, but the effect of these are assumed to be negligible variables to the properties under investigation and thus not focused in the present work. Other than these, the basic growth process, growth pressure, and precursors used for all the samples are similar as the typical LED structure grown by MOCVD described in Section 3.3. Each wafer is labeled by an alphanumeric system where the number refers to the structure (Ga_N, MQW, AlGa_N capped MQW or LED), while the letter refers to differences in growth parameters. For instance, sample name A4 indicates that the wafer is a Ga_N structure with set A process conditions.

5.1.1 Sample Set 4: nGa_N Structures

Two sets of Ga_N samples, A4 and C4 were grown and their structures are shown in Figure 5.1, respectively. A4 is 2in nGa_N sample with uGa_N recovery and nGa_N layers grown at 1085°C, while both layers of the 6in C4 sample were grown at 1080°C.

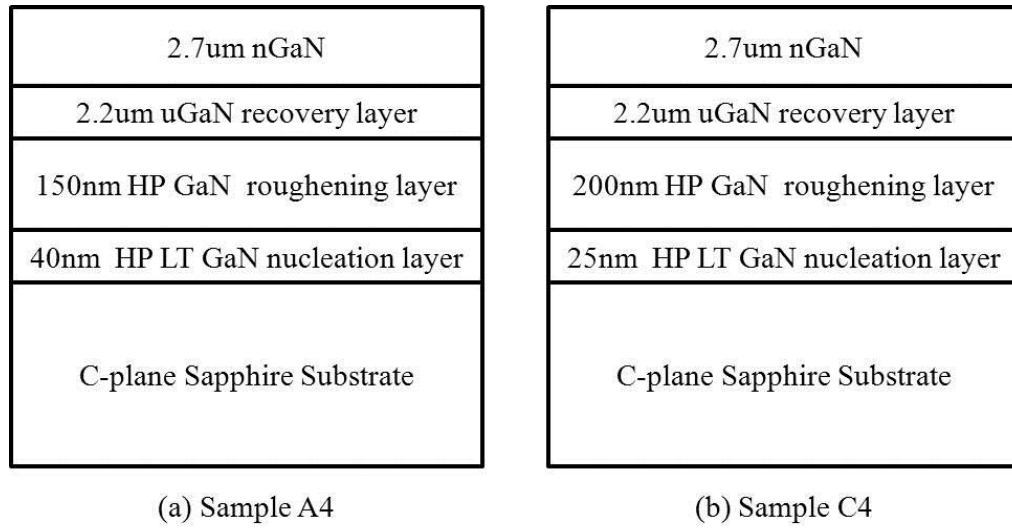


Figure 5.1: Schematics of GaN structures A4 (a) and sample C4 (b)

5.1.2 Sample Set 3: MQW Structures

Figure 5.2 shows the structure for three sets of MQW structures, A3, B3, and C3. A3 is 2in, 4pair MQW sample with GaN quantum barriers and InGaN quantum wells grown at 760°C on top of A4. B3 is 4in, 6pair MQW sample with 860 °C GaN quantum barriers and 760 °C InGaN quantum wells grown on 1100 °C uGaN. C3 is 6in, 4 pair MQW sample with GaN quantum barriers and InGaN quantum wells grown at 767°C on top of C4.

4 pairs of 2.6nm $\text{In}_{0.14}\text{Ga}_{0.86}\text{N}/10\text{nm GaN MQW}$ active layer.	6 pairs of 2.8nm $\text{In}_{0.13}\text{Ga}_{0.87}\text{N}/13\text{nm GaN MQW}$ active layer.	4 pairs of 2.1nm $\text{In}_{0.15}\text{Ga}_{0.85}\text{N}/10\text{nm GaN MQW}$ active layer.
2.7um nGaN	2.7um uGaN	2.7um nGaN
2.2um uGaN recovery layer	2.2um uGaN recovery layer	2.2um uGaN recovery layer
150nm HP GaN roughening layer	200nm HP GaN roughening layer	200nm HP GaN roughening layer
40nm HP LT GaN nucleation layer	25nm HP LT GaN nucleation layer	25nm HP LT GaN nucleation layer
C-plane Sapphire Substrate	C-plane Sapphire Substrate	C-plane Sapphire Substrate
(a) Sample A3	(b) Sample B3	(c) Sample C3

Figure 5.2: Schematics of MQW structures A3, B3, and C3

5.1.3 Sample Set 2: pAlGaN Capped MQW Structures

Figure 5.3 shows the structure for pAlGaN capped MQW sample A2. pAlGaN is grown at 980°C on top of A3.

20nm pAl _{0.15} Ga _{0.85} N
4 pairs of 2.6nm In _{0.14} Ga _{0.86} N/10nm GaN MQW active layer
2.7um nGaN
2.2um uGaN recovery layer
150nm HP GaN roughening layer
40nm HP LT GaN nucleation layer
C-plane Sapphire Substrate

Figure 5.3: Schematics of pAlGaN capped MQW structure A2

5.1.4 Sample Set 1: LED Structure

Figure 5.4 shows the schematics of two sets of LED structures, A1 and B1. A1 is 2in LED sample with pGaN layer grown at 980°C on top of A2. B1 is 4in LED sample with pAlGaN and pGaN grown at 975°C on top of B3.

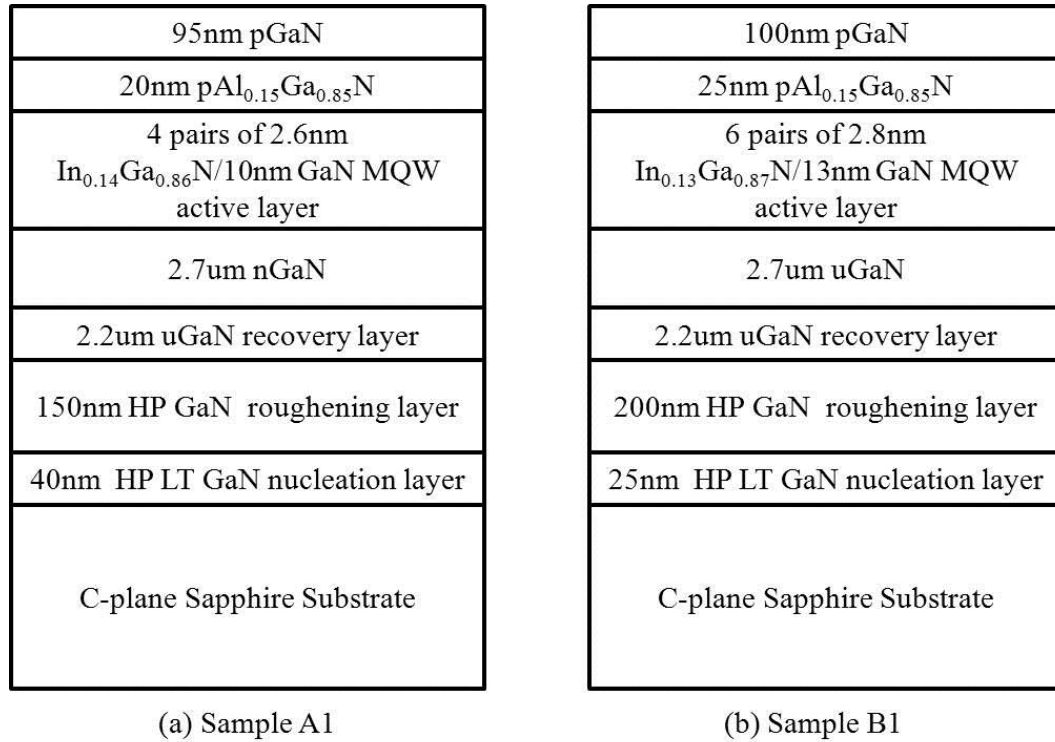


Figure 5.4: Schematics of LED structures A1 and B1

5.2 Characterization Techniques

5.2.1 Microscope

Olympus MX61 microscope is used to study micron scale surface morphology of the samples.

5.2.2 AFM, SCM, and CAFM

Bruker-nano Icon Scanasyst AFM is used to study the sub-micron surface morphology of samples. TESPA probes are used for AFM scans.

SCM module is attached to the AFM system for capacitance and electrical property measurements of the samples. SCM tip holder and SCM-PIC probes are used for AFM-SCM scans. Together with SCM module, the AFM system is capable to acquire the surface morphology image and capacitance data simultaneously, with a one to one

correlation between dislocations either at or beneath surface to the electrical characteristics. During the application of SCM module, a low frequency AC field from 5 to 100 kHz is generally applied between the metallized SCM-PIC probe and the semiconductor surface. As a result, free carriers in the sample are attracted and repelled by the probe consecutively. The change in capacitance between the probe and the sample, therefore, is measured by using a resonant capacitance sensor which operates at around 885MHz. A DC bias can be simultaneously applied to allow control over the voltage at which the AC signal varies [40][87].

CAFM module is mounted to the AFM system for conductivity studies of the sample. Extended-tunneling AFM tip holder and PFTUNA probes are used for AFM-CAFM scans. Similarly as SCM, a selectable bias is applied between the sample and the conductive PFTUNA probe, with the probe set as virtual ground. As the probe is scanning the sample in contact mode and imaging the topography, an electrical amplifier (1pA-1 μ A) measures the current passing through the sample. Thus, the surface morphology image and current image are measured at the same time, allowing the one to one correlation of sample location to its electrical characteristics.

5.2.3 XRD

Triple axis XRD studies are done with Panalytical X'Pert PRO XRD with Empyrean Cu LFF HR X-ray tube, hybrid 2-bounce Ge (220) monochromator, and Xe proportional detector.

5.2.4 Time Resolved PL

Coherent MIRA 900 femtosecond pulse laser and Hamamatsu streak camera are used for the room temperature time resolved PL measurements. The laser emission is

frequency doubled to 375nm, and pulse frequency is 3.79MHz chosen by a pulse picker. A 150g/mm grating glazing at 300nm and 1mm slit are used in the Streak camera of resolution 20ps.

5.2.5 EL

Maxmile EpiEL 700 EL mapper is used to measure EL properties of LED structures. N-contacts are formed via the sample holder at the sidewall of the wafer while p-contact is achieved by a probe in contact with the top surface of the wafer, i.e., the p-GaN layer, during measurement.

5.2.6 SEM-CL

SEM-CL studies are carried out using a field emission gun (Carl Zeiss 1550 FE-SEM Gemini Column) and a Gatan MonoCL4 Elite high resolution CL system. A retractable paraboloidal mirror collects the light emitted from the sample and collimates it into the light guide tube. A monochromator with a 1200 line/mm dispersion grating blazed at 500nm is used. The CL system is equipped with a Hamamatsu Peltier cooled, high sensitivity photomultiplier detector that provides a wavelength detection range from 160nm to 930nm.

The beam current that goes to the sample is measured by using a Faraday cup and its dependence on EB voltage and aperture size is shown in Figure 5.5. Beam current increases monotonously with increasing EB voltage or aperture size, while the latter affects the increase of beam current predominantly.

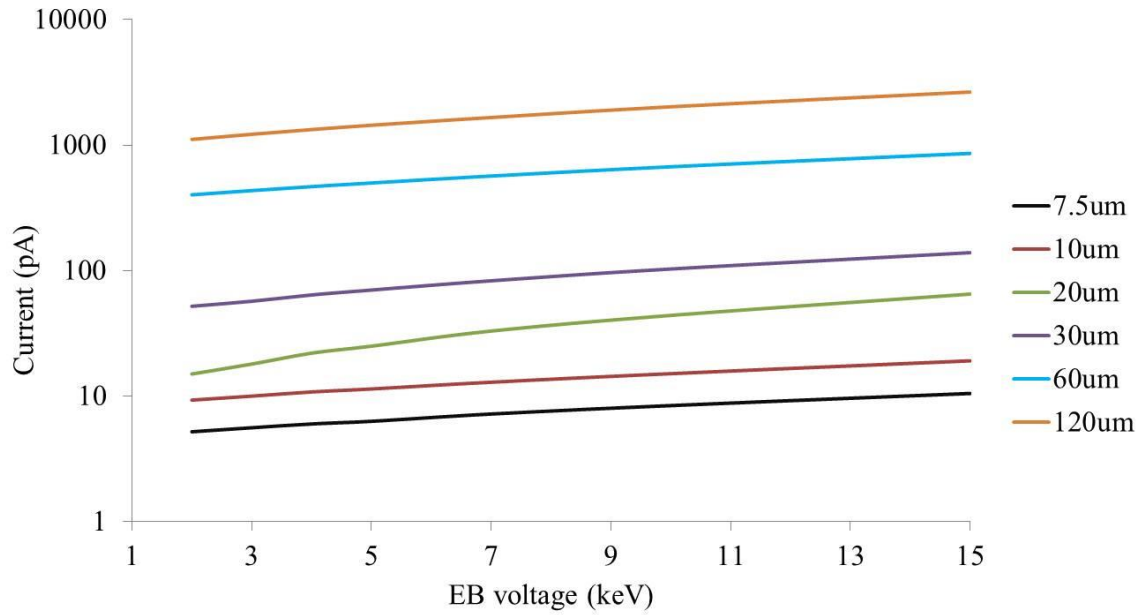


Figure 5.5: CL beam current versus EB voltage and aperture size

When a secondary electron generates an e-h pair in a semiconductor, such an electron requires a kinetic energy of about three times the band-gap energy [88][89]. Supposing that all the kinetic energy of one incident electron is used for the generation of e-h pairs, the multiplication factor is given by:

$$\alpha = \frac{1}{3} \cdot \frac{E}{E_g}, \quad (5-1)$$

where E and E_g are the EB voltage and bandgap energy, respectively. On the other hand, the number of incident electrons per second is:

$$N = \frac{I}{e}, \quad (5-2)$$

where I and e are the beam current and the elementary electric charge, respectively.

Using these two values, the number of e-h pairs generated per second in the diffusion region, N_{e-h} is:

$$N_{e-h} = \alpha \cdot N = \frac{1}{3} \cdot \frac{E}{E_g} \cdot \frac{I}{e} \quad [70] \quad (5-3)$$

Therefore, both increasing EB voltage and aperture size will increase the beam current, and in turn the number of e-h pairs generated per second in the sample.

The EB diffusion path and diffusion length is simulated by Electron Flight Simulator based on Monte Carlo model. Figure 5.6 shows the EB interaction with MQW sample A3 at various EB voltages as an example. To simplify the simulation, the 4 layers of GaN barriers and InGaN wells in MQW are added together as 40nm single barrier layer, and 10.4nm InGaN single layer, respectively. The top white layer stands for the GaN barrier, middle light grey layer for the InGaN well, and bottom dark grey layer for bulk GaN. The trajectories of the EB diffusion paths formed an almost spherical interaction volume and more interactions happen around the equator area. However, due to the electron energy loss, the e-h pair generation rate does not keep constant through the whole interaction volume [71]. Ref. [90] shows the EB energy deposition profile in a bulk GaN layer, and Ref. [91] shows that in a typical InGaN/GaN SQW structure. In both references, the EB energy deposition profiles are similar to an inverted water drop shape, which indicates that more energy is confined to the top regions of the interaction volume. Also it has been reported that e-h pair generation rate in the InGaN wells increases with increasing EB penetration length in bulk GaN layer. The changes of penetration length in GaN barriers do not lead to significant changes in recombination rate in InGaN wells, and almost all carriers generated in GaN barriers recombines in InGaN wells [92]. The number of e-h pair generated in the interaction volume will be affected by the combination effects from the EB diffusion profile and the electron energy deposition profile. Therefore, at 2keV,

EB diffuses within the MQW layer for the depth of approximately the top 2.5 pairs of MQW, and most e-h pairs recombined in the top one InGaN QW. At 3keV, EB covers the whole MQW stack and starts to diffuse into the bulk GaN layer. Most e-h pairs generated recombine at the top two or three InGaN QWs. From 4keV, EB diffuses deeper and deeper into the bulk GaN layer. The deeper it diffuses, the more e-h pair are generated and recombined in the MQW, mainly in the bottom pairs of MQW than the top ones.

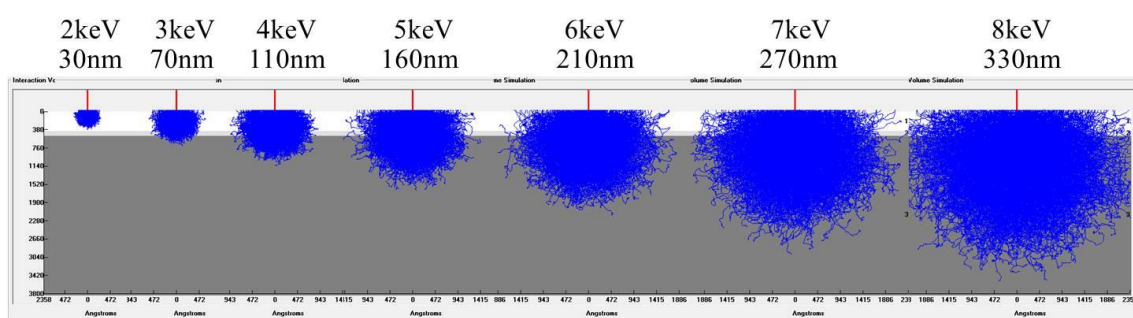


Figure 5.6: Schematic of the diffusion of EB into the MQW sample A3

5.2.7 STEM

In TEM systems, electrons pass through thin specimen and form transmission illumination microscopy. STEM is one of them. The difference between STEM and conventional transmission electron microscopes (CTEM) is that the former focuses the EB into a minute spot and scans over the sample.

The STEM work has been done in Evans Analytical Group in North Carolina. The sample was imaged in a Hitachi HD-2300 dedicated STEM, operated at 200kV with a nominal 0.20 nm diameter electron beam.

Fiducial markings were scribed into the epilayer on the sample and specific site having multiple surface defects were selected and the appropriate a-plane section marked

with Carbon using an S-4700 FE-SEM. STEM ready sample was prepared using a proprietary in-situ lift-out technique in an FEI FIB 200. The protective layers applied to the sample were as follows (from the sample surface up):

- thin polymeric coating was applied locally on the sample;
- ~75-100nm of 99.99% purity Pt was applied by magnetron sputter coating;
- a Pt/C capping layer was applied to the area of interest by the FIB in-situ.

5.2.8 SIMS

SIMS measurement is performed at Evans Analytical Group in California. The Cameca 4F magnetic sector SIMS system is used. 14.5keV Cs ion beam has been applied.

CHAPTER 6: RESULTS AND DISCUSSION

6.1 nGaN As-grown Structure: Sample A4 and C4

6.1.1 Surface Morphology

Optical microscope images of A4 and C4 are shown in Figure 6.1. Micron size pits are observed in the surface morphology of A4, but not in C4. The pits on GaN are most likely caused by relatively low growth temperature. Submicron pits cannot be observed by optical microscope, so higher resolution microscopy tool is needed.

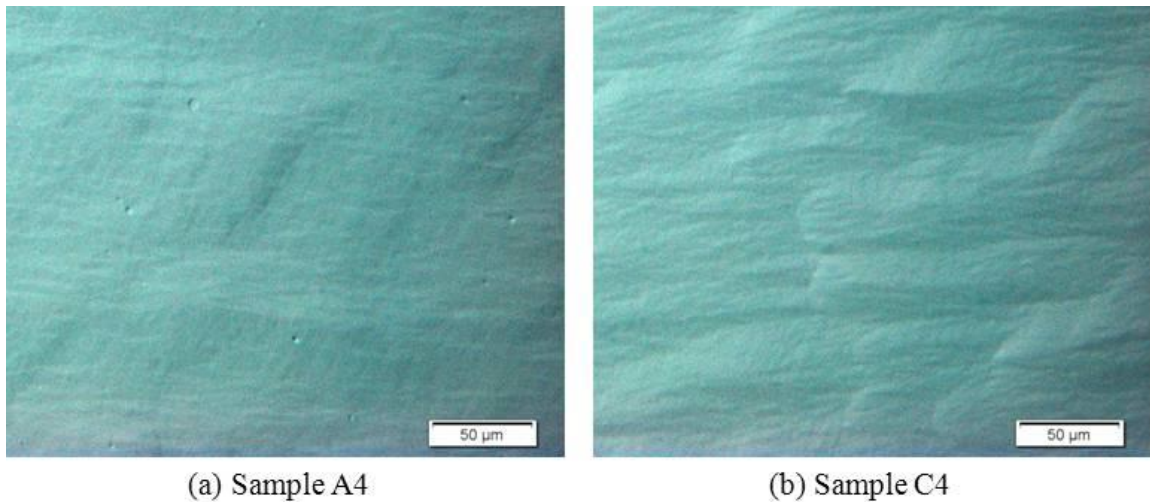


Figure 6.1: Microscope images of nGaN samples A4 and C4

Figure 6.2 shows the AFM images on both samples and presents the submicron scale surface morphology. Other than clear terrace line of nGaN, pits of size from 60nm to 90nm are observed in A4. Average pit density is $2.1 \times 10^8 \text{cm}^{-2}$. No pits are observed in C4. This is consistent with the microscope images results, as a GaN surface with micron size pits is expected to have smaller pits as well. The RMS roughness for A4 and C4 are about 0.4nm and 0.3nm, respectively.

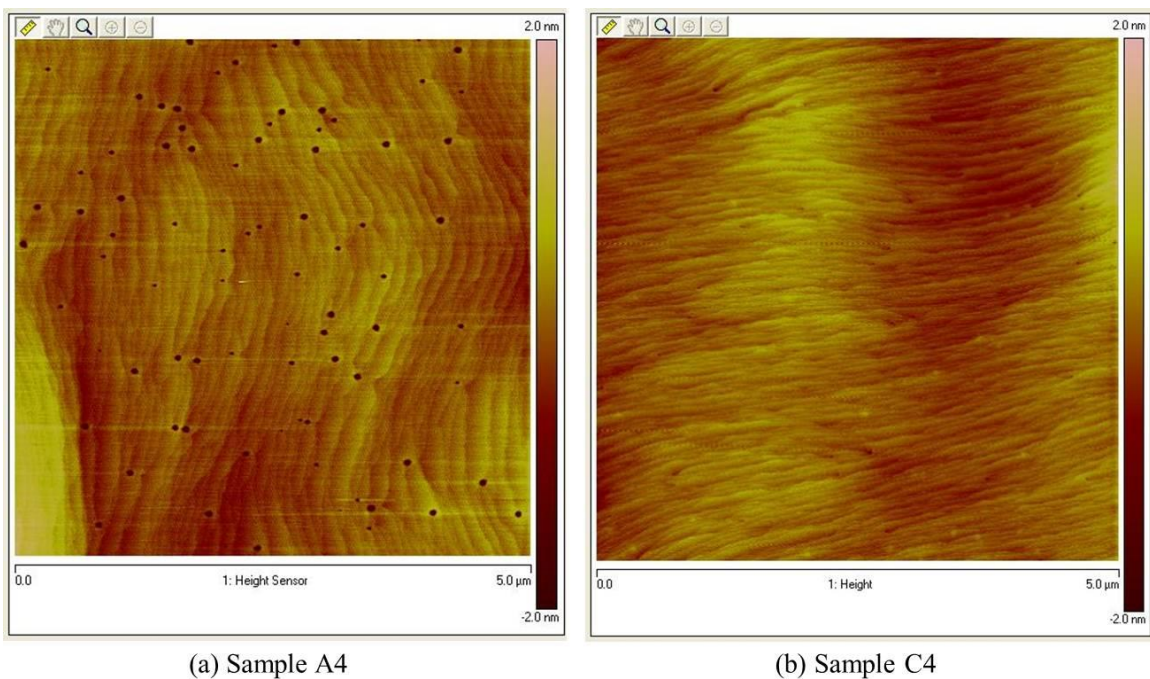


Figure 6.2: AFM images of nGaN samples A4 and C4

6.1.2 SEM-CL and Spot CL Analysis

EB interaction in the bulk nGaN layer is simulated by EFS and shown in Figure 6.3 along with the approximate diffusion length. The diffusion length increases with EB voltage as discussed in Section 5.2.5. SEM-CL studies at 2keV and 6keV EB voltages at 30um aperture size are done to sample A4 to study the luminescence properties of the

nGaN structure.

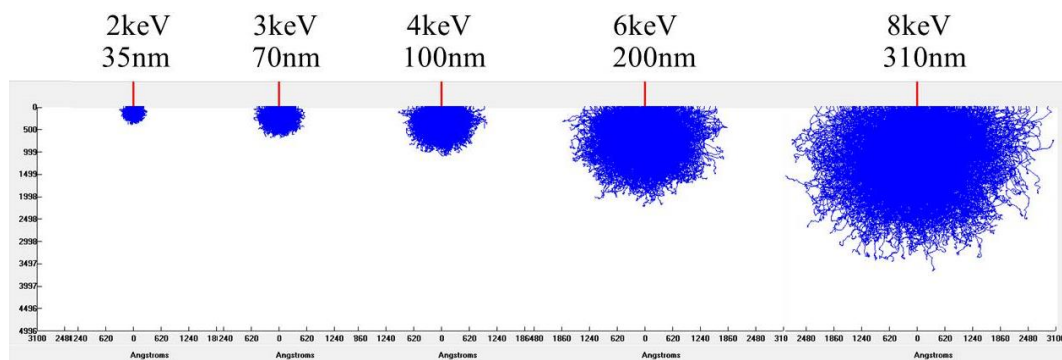


Figure 6.3: EB penetration volume in bulk nGaN simulated by EFS

Figure 6.4 shows the 4 μm by 4 μm SE SEM image and the corresponding panchromatic CL image from 250nm to 800nm and monochromatic CL image at 362nm on A4 at 2keV EB voltage and 30 μm aperture size. The 60nm to 90nm size pits observed in the AFM morphology are also clearly observed in the SEM image, and they show as dark spots with a center of bright contrast in the panchromatic CL image. It suggests that the dark luminescence spots correspond to the dislocations, which the pit originated from, while the centers with bright contrast come from the optically enhanced c-plane emission around and/or beneath the defect cores by the inclined sidewalls of the pits. The solid dark spots observed in CL image correspond to the dislocations or other defects hiding beneath the surface, while they are not observed in the SEM image. Monochromatic CL image is taken by using 1200L/mm grating blazing at 500nm and 0.1mm slit width. The bandpass is about 2.5nm. It has relatively low contrast due to the small bandpass at the targeting wavelength of 362nm in this case. Dark spots have one to one correlation between both CL images, which confirms that the dark spots are coming from dislocations or other defects in the EB interaction volume. Those defects, as reported by

numerous previous works listed in Table 2.1, are NRRCs as confirmed by the dark contrast in the CL image. Average dark spot density is $2.8 \times 10^8 \text{ cm}^{-2}$ in the 362nm CL images.

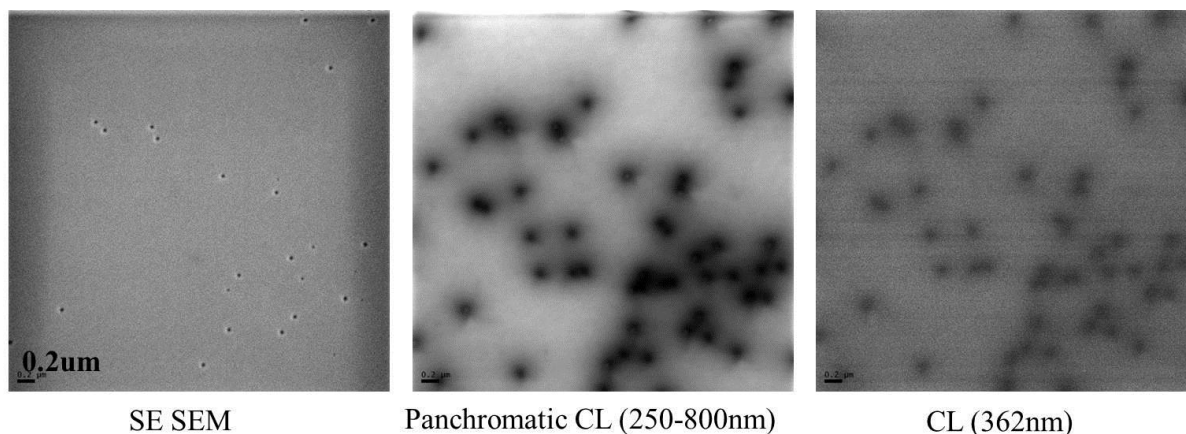


Figure 6.4: SE SEM, panchromatic CL, and monochromatic CL (at 362nm) images of nGaN sample A4 at 2keV EB voltage and 30um aperture size

Similar work is done on A4 at 6keV EB voltage, 30um aperture size. Same grating and slit width are used. According to Figure 6.3, EB interaction volume increases with increasing EB voltage from 2keV to 6keV. As discussed in Section 5.2.5, the number of generated e-h pairs is higher at 6keV EB voltage. Figure 6.5 shows the 4um by 4um SE SEM image and the corresponding panchromatic CL image and monochromatic CL image at 362nm on A4 at 6keV EB voltage and 30um aperture size. Similar to Figure 6.4, pits are observed in the SEM image and CL images. Dark luminescence with bright contrast centers correspond to the pits in SEM, and solid dark spots correspond to dislocations and other defects beneath the surface in the EB interaction volume as discussed before. The average dark spot density at 6keV, however, is $3.7 \times 10^8 \text{ cm}^{-2}$ in the 362nm CL images, which is 1.3 times of that at 2keV. This increase in defect density is

consistent with the dislocation density reduction as the thickness of GaN increases, as discussed in Section 3.3.4.

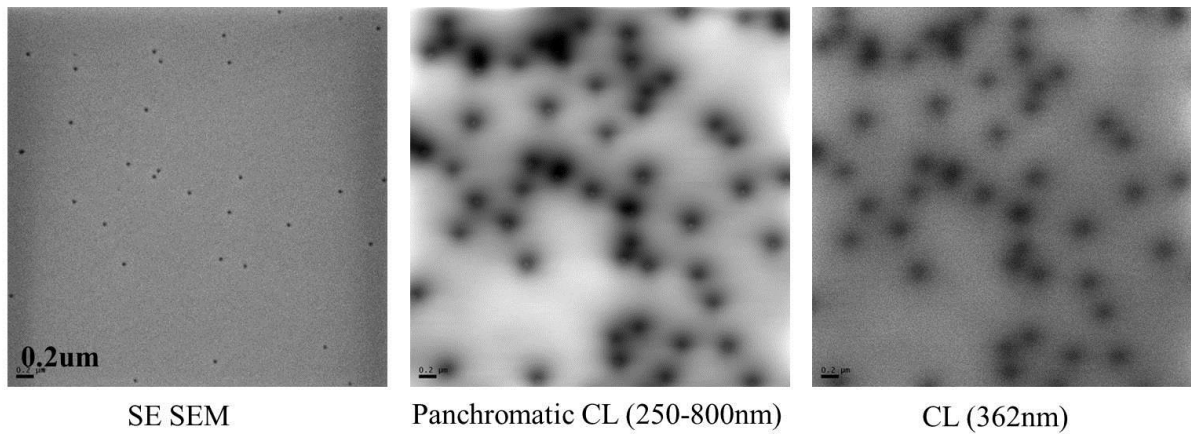


Figure 6.5: SE SEM, panchromatic CL, and monochromatic CL (at 362nm) images of nGaN sample A4 at 6keV EB voltage and 30um aperture size

Figure 6.6 shows the CL spot spectrums at high contrast pit free spots (bright) and dark spots (dark) at 2keV and 6keV EB voltages. Peak emission energies at 3.44eV are observed for all spectrums. Bright spots show higher peak CL intensity than dark spots taken at the same EB voltages. Since the number of e-h pairs generated and interaction volume increase with increasing EB voltages, higher CL peak intensities are observed at 6keV than 2keV. No shift in peak energy is observed since there is no PZ filed in bulk GaN material. GaN peaks skew to the lower energy side due to the donor-valance band emission as reported in [93][94]. No emission is observed from 2.75eV to 2.85eV.

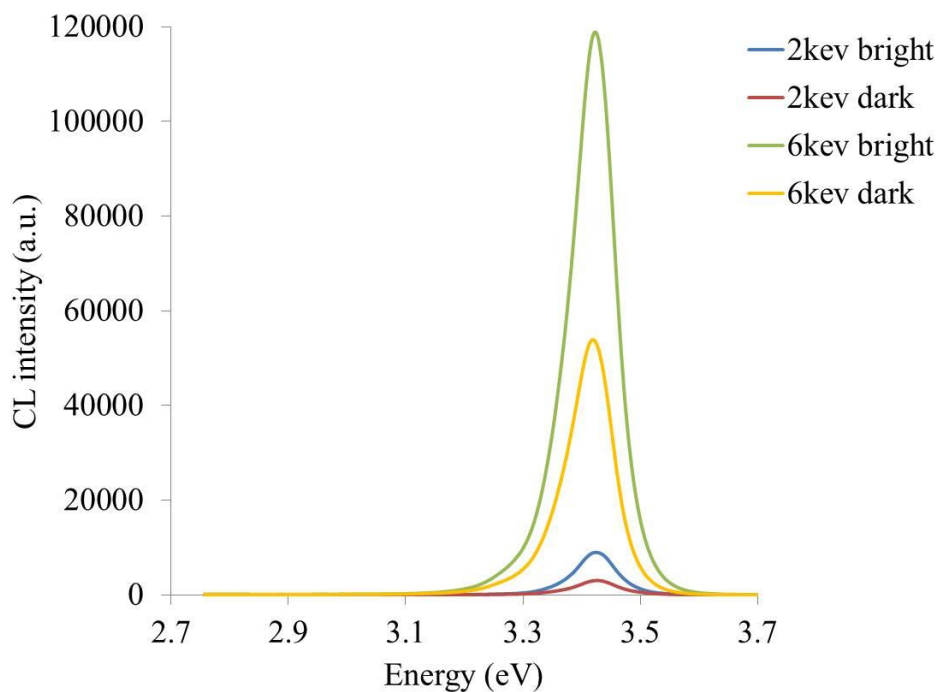


Figure 6.6: CL spot spectrums at bright and dark spots at 2keV and 6keV EB voltages on sample A4

6.1.3 STEM Analysis

Cross-section STEM is done on bulk GaN sample A4 and shown in Figure 6.7. Threading dislocations terminate at the surface and form open pits, which were observed in both AFM and SEM images. From the surface down, more dislocations are observed, which is consistent with the CL results.

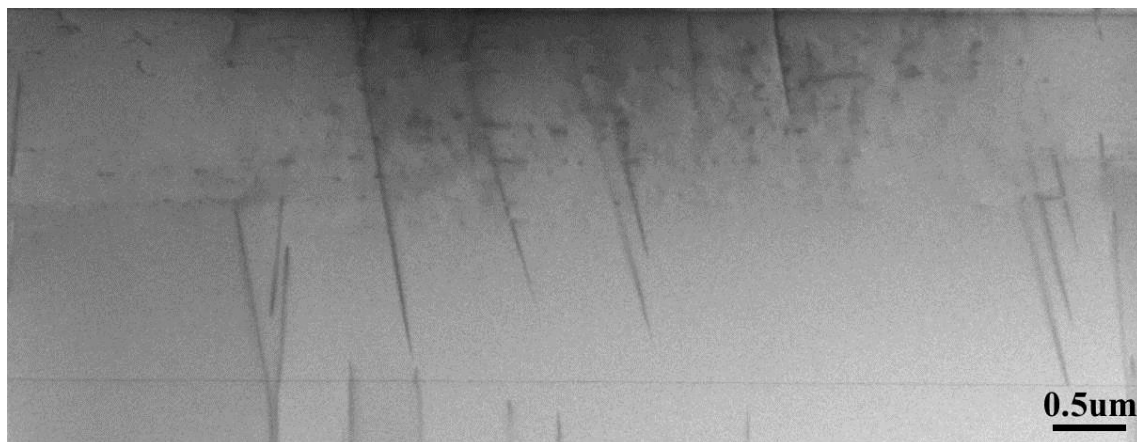
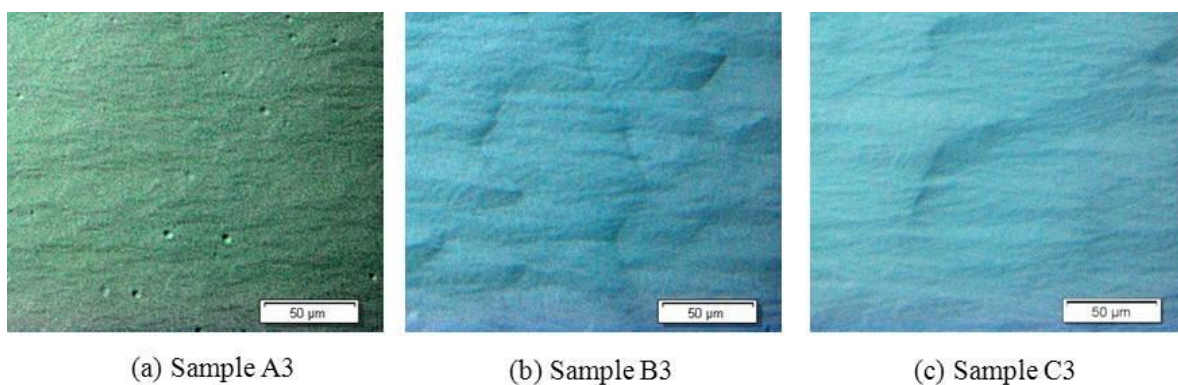


Figure 6.7: Cross-section STEM image of GaN A4

6.2 MQW As-grown Structure (Sample A3, B3 and C3)

6.2.1 Surface Morphology

Microscope images of MQW samples A3, B3 and C3 are shown in Figure 6.8. Micron size pits are observed in the surface morphology of A3, but not in B3 and C3. GaN sample for B3 was not produced (i.e., no B4), but it can be safely predicted that such a GaN sample (B4), does not have a pitty surface morphology, akin to C4.



(a) Sample A3

(b) Sample B3

(c) Sample C3

Figure 6.8: Microscope images of MQW samples A3, B3 and C3

Figure 6.9 shows the AFM submicron scale surface morphology for all MQW samples. The V-pits observed in A3 and C3 have a size range from 60nm to 100nm, while the V-pit size ranges from 80nm to 140nm in B3. Average V-pit density is $5.7 \times 10^8 \text{cm}^{-2}$ in A3, $2.5 \times 10^8 \text{cm}^{-2}$ in B3 and $3.3 \times 10^8 \text{cm}^{-2}$ in C3. It is observed that the terrace lines in sample A3 and C3 are flatter than those in B3, which indicates that A3 and C3 are more relaxed than B3. This is consistent with the higher V-pit density, which helps with strain relaxation as reported in numerous studies, [20][54][95][98].

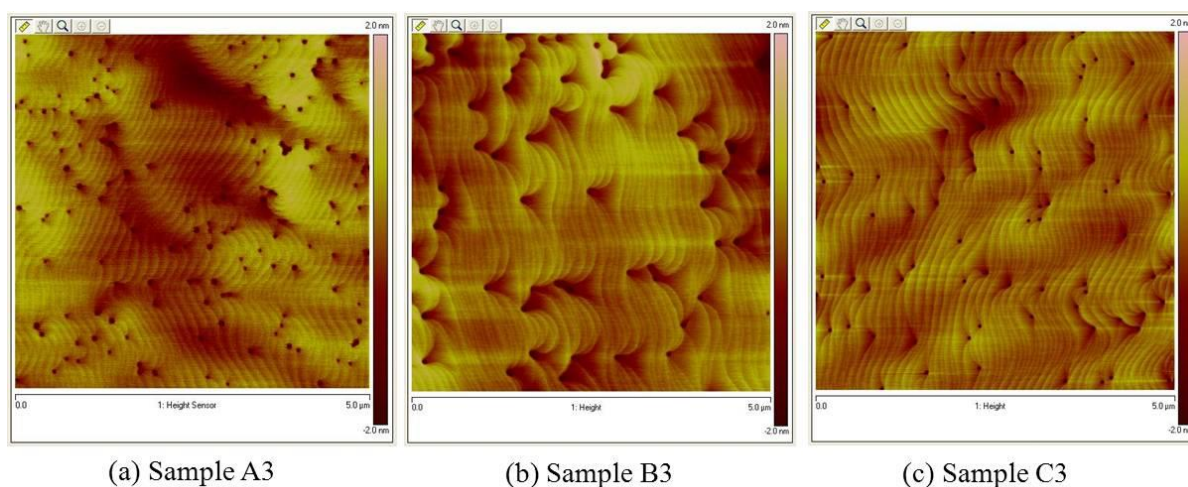


Figure 6.9: AFM images of MQW samples A3, B3 and C3

6.2.2 XRD Analysis

Triple axis XRD scan is done on the (002) plane of MQW samples A3, B3 and C3. The diffraction patterns are shown in Figure 6.10. Since A3 and C3 have 4 pairs of MQW, the XRD curves show 2 secondary maxima fringes, 4 secondary maxima fringes for the 6 pair MQW sample B3. It is apparent that satellite peaks are of higher contrast in B3 than in A3 and C3, while the latter 2 show similar contrast to each other. This indicates that

the InGaN/GaN interface quality, i.e., abruptness, is notably better in B3 [95]. It is acknowledged that non-abrupt interfaces are associated with rough surface (i.e. larger surface area) and enhanced the impurity incorporation into the crystal. Therefore, A3 and C3 are expected to have higher impurity concentration, which will be discussed in the following sections.

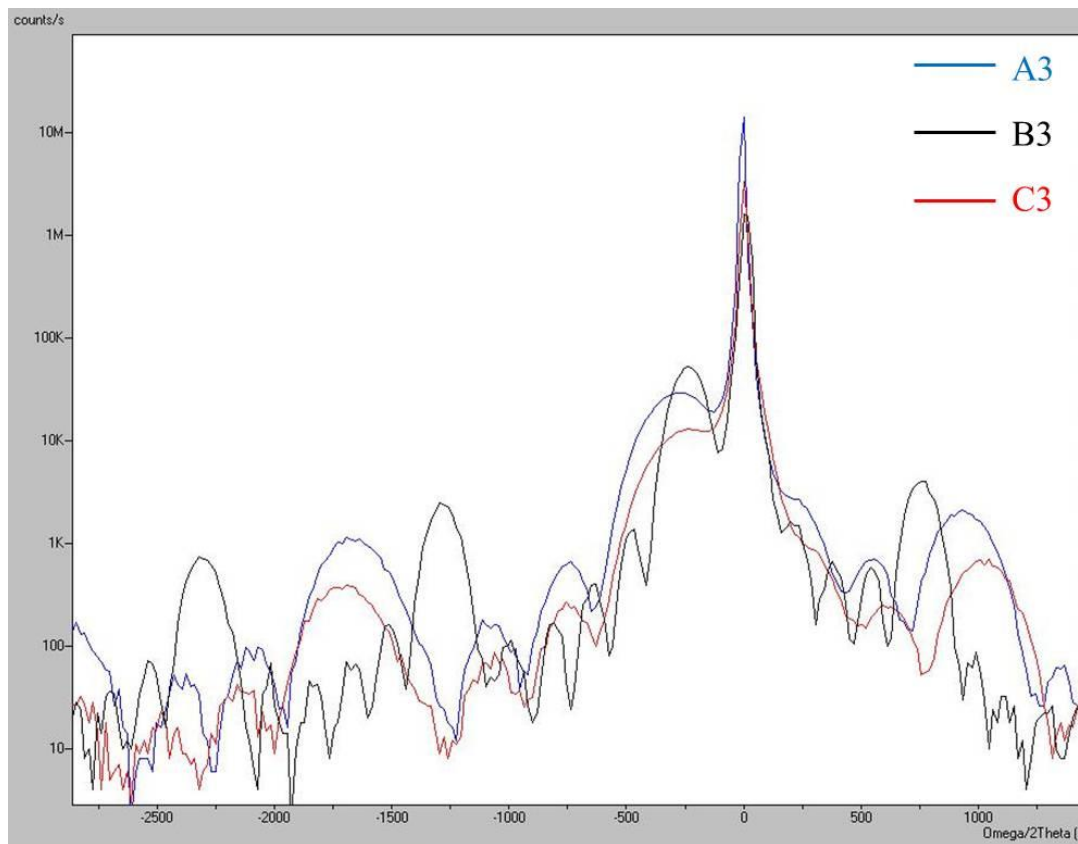


Figure 6.10: Triple axis XRD scan of MQW samples A3, B3 and C3

6.2.3 Room Temperature Power Dependent PL Analysis

The time resolved PL system is used for this power dependent PL study. Laser power has been set at various levels from 0.05mW to 3mW to measure MQW sample A3, the

spectrums shown in Figure 6.11. At all pump powers, the emission peak at around 2.74eV (453nm) and an obvious should at around 2.85eV (435nm) are observed. Since the 1mm slit is used in the measurements and the bandpass is about 21nm, the resolution of the measurements is low. However, the double peak emission is still detectable. This proves that the double peak emission intrinsically exists in sample A3, and not from the electron beam induced effects discussed in Section 4.3. At the highest pulse power, 3mW, the number of photons generated per pulse is about 1.5×10^9 considering no energy loss in the whole optical system. This carrier generation rate will be compared to that of the CL measurement later.

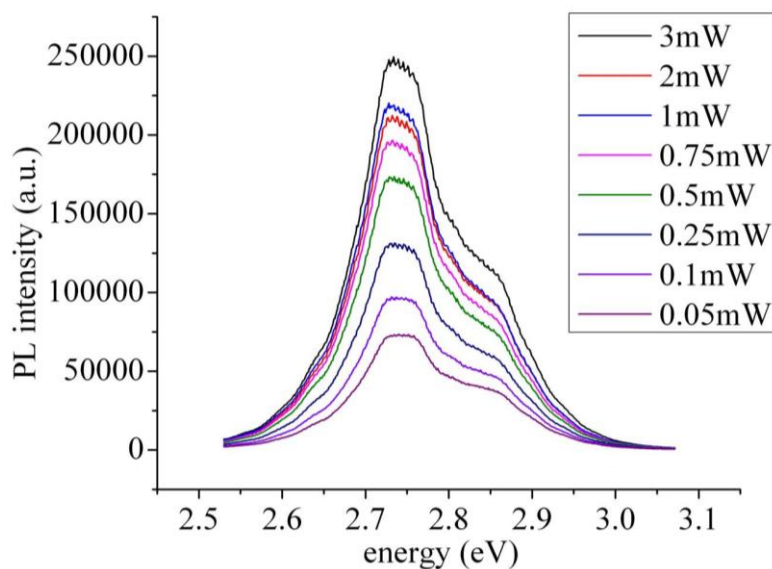


Figure 6.11: Room temperature power dependent PL spectrum of sample A3

B3 and C3 are measured by the same settings with the pulse power at 2mW. Figure 6.12 shows the measured PL spectrums for A3, B3 and C3 pumped at 2mW. The 2.85eV peak is observed in C3 as well, but not in B3, which indicates that the high-energy peak exist regardless of the presence of pits in bulk GaN layer. Another mechanism should be

responsible for the formation of the high-energy peak. The shoulders shown at lower energy side of the peak may be interference fringes.

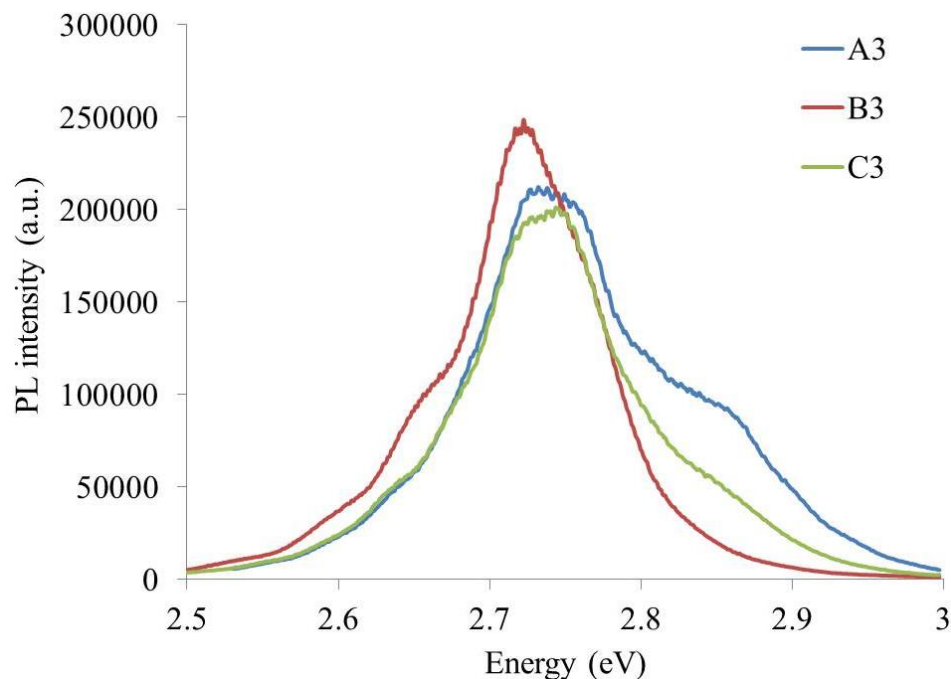


Figure 6.12: Room temperature PL spectrums of sample A3, B3 and C3 at 2mW pulse power

6.2.4 CL Analysis

6.2.4.1 SEM-CL Analysis

Figure 6.13 shows the CL spectrum in logarithmic scale, from which the peak emission wavelengths of GaN (362nm) and MQW (452nm) are detected and set as the central wavelengths for the monochromatic CL images. Figure 6.14 shows the 4 μ m by 4 μ m SE SEM image, the corresponding panchromatic CL image and monochromatic CL images at 362nm and 452nm on A3 at 2keV EB voltage and 30 μ m aperture size. Terrace lines are vaguely observed in the panchromatic CL image. The 60nm to 100nm size pits observed in the AFM morphology are also clearly observed in the SEM image, and they

show as dark spots in the panchromatic CL image and 452nm monochromatic CL image due to the lack of crystal growth in the vacancy and the defects (NRRCs) from which V-pits originate. Luminescence fluctuations in the pit free areas are also observed in the panchromatic and 452nm CL images. Monochromatic CL image is taken by using 1200L/mm grating blazing at 500nm and 0.1mm slit width. The bandpass is about 2.5nm. The 362nm CL image does not show any contrast since EB does not penetrate into the bulk GaN layer at 2keV EB voltage, and most e-h pairs generated in MQW recombine in InGaN wells as discussed in Section 5.2.6.

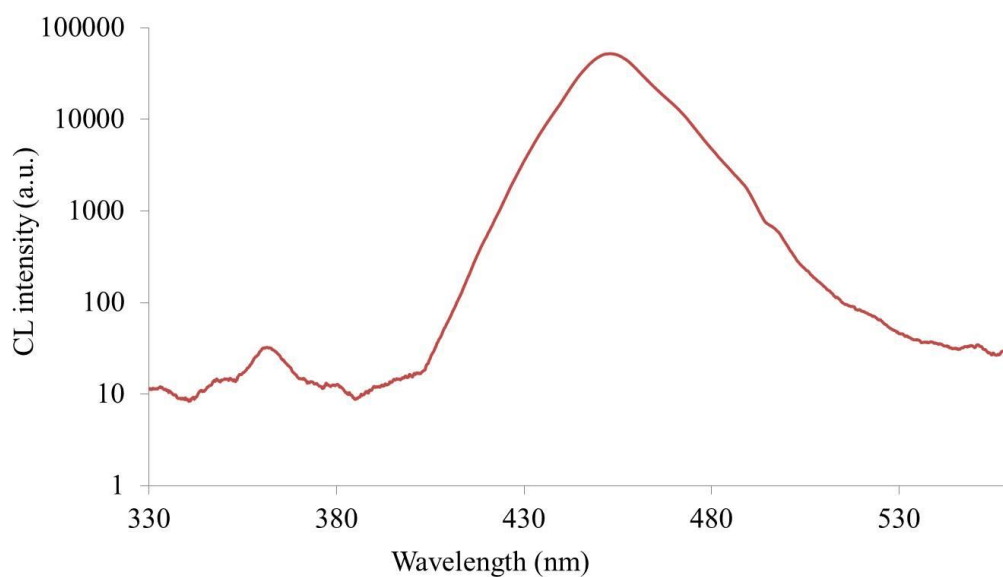


Figure 6.13: CL spectrum of A3 at 2keV EB voltage and 30um aperture size

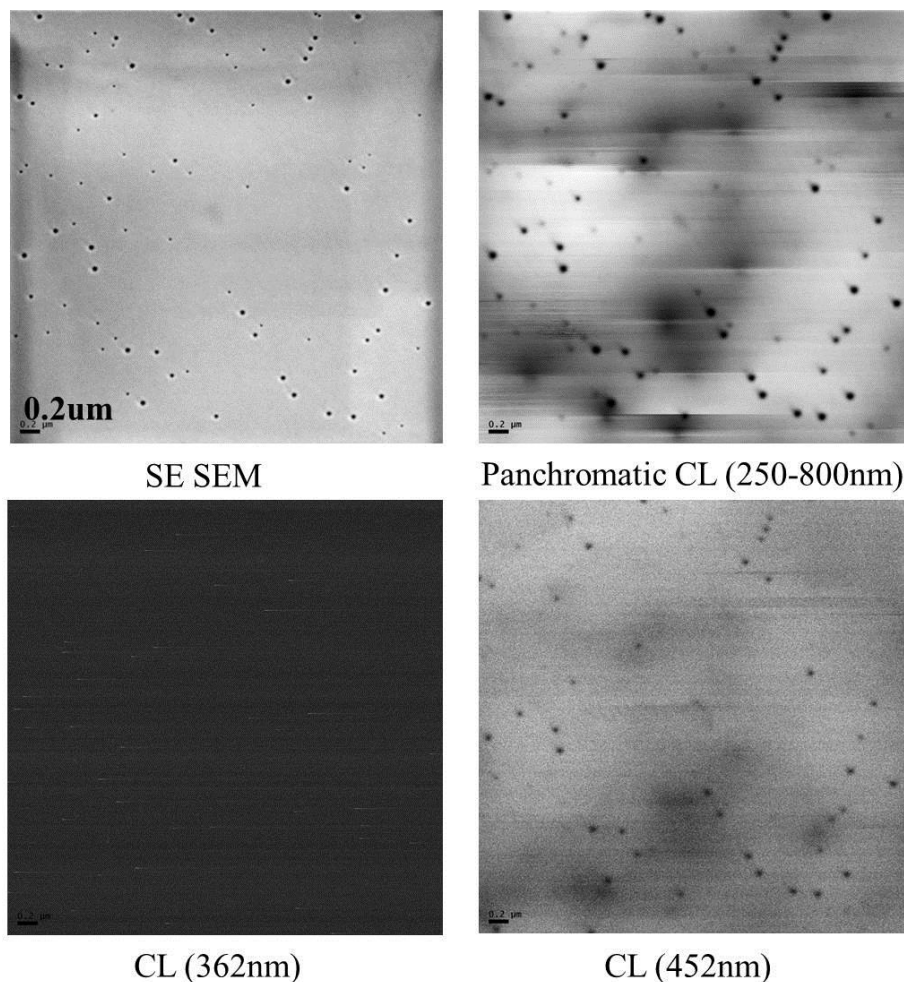


Figure 6.14: SE SEM, panchromatic CL, and monochromatic CL (at 362nm and 452nm) images of MQW sample A3 at 2keV EB voltage and 30μm aperture size

Similar analysis with the same CL settings is done at 4keV EB voltage and 30μm aperture size, in which the EB diffuses through the MQW layer to the bulk n-GaN. Figure 6.15 shows the CL spectrum in logarithmic scale. GaN peak is apparent in this case. A left shoulder in the MQW emission is observed, which will be discussed in detail in the following sections. Figure 6.16 shows the 4μm by 4μm SE SEM image and the corresponding panchromatic CL image and monochromatic CL image at 362nm (GaN emission) and 452nm (MQW emission) on A3 at 4keV EB voltage and 30μm aperture

size. Once more, the V-pits show as dark spots in the SEM, panchromatic CL and 452nm CL images. In 362nm CL image, however, the V-pits show as higher contrast centers surrounded by dark halos. Since GaN emits at higher energy, GaN emission can be reabsorbed by the MQW layer on top. However, in the presence of V-pits, this emission from bulk nGaN survives, as there is no absorber InGaN within the V-pits. Luminescence fluctuations in the pit free areas are again observed in the panchromatic and 452nm CL images, but not in the 362nm CL image, which indicates that the luminescence fluctuations are from MQW emission rather than GaN emission.

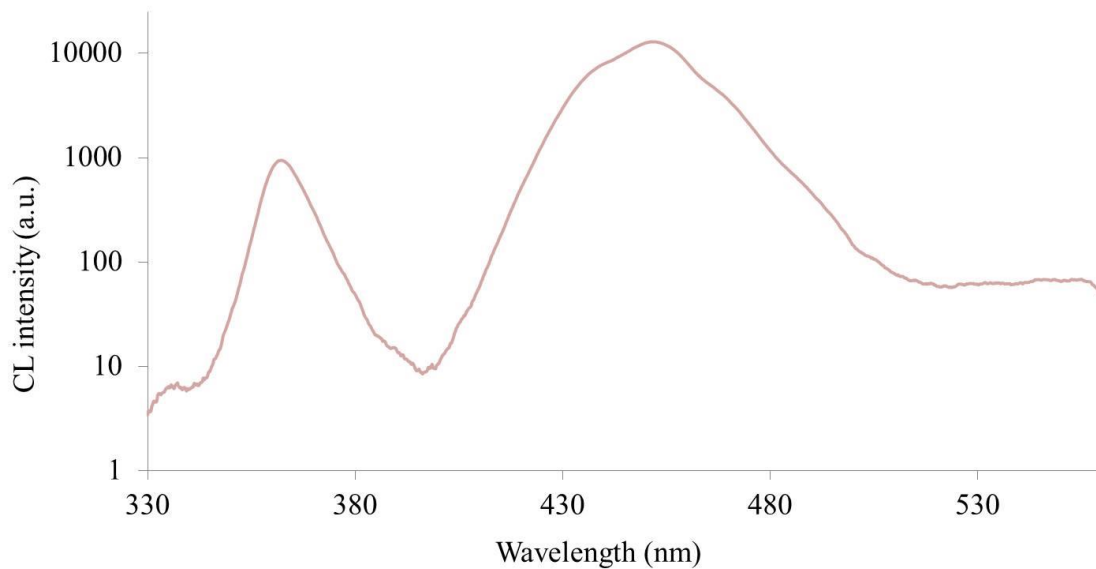


Figure 6.15: CL spectrum of A3 at 4keV EB voltage and 30um aperture size

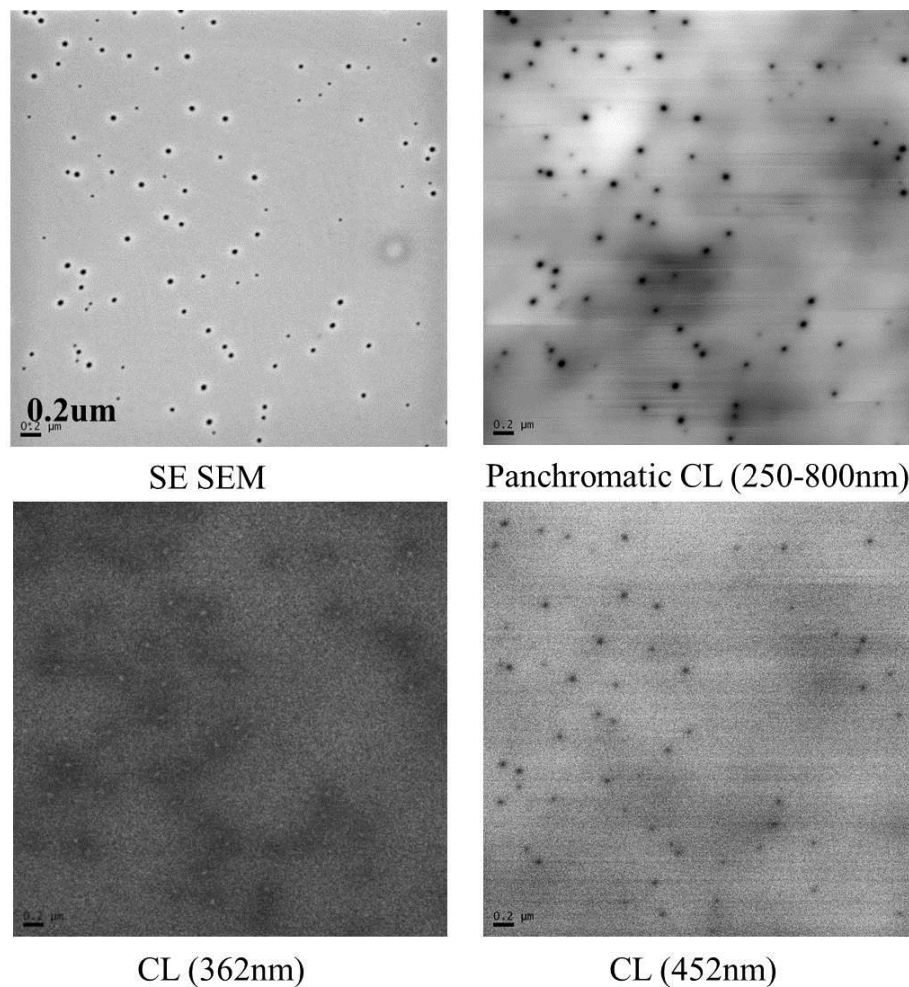


Figure 6.16: SE SEM, panchromatic CL, and monochromatic CL (at 362nm and 452nm) images of MQW sample A3 at 4keV EB voltage and 30um aperture size

Similar analysis with same CL settings is done at 8keV EB voltage and 30um aperture size, in which the EB diffuses through the MQW layer to the bulk n-GaN. Figure 6.17 shows the CL spectrum, which shows the GaN emission around 364nm and a double peak emission at around 440nm and 450nm. These wavelengths, therefore, are set as central wavelength for monochromatic CL images. Figure 6.18 shows the 4um by 4um SE SEM image and the corresponding panchromatic CL image and monochromatic CL image at 364nm (GaN emission), 440nm and 450nm on A3 at 8keV EB voltage and

30um aperture size, in which EB diffuses $\sim 0.3\mu\text{m}$ into the bulk GaN. The intensity of the GaN emission peak increases with increasing EB voltage, since more e-h pairs are generated and recombined in bigger interaction volume in the nGaN layer. The new peak centered at around 440nm seems to have the same origin as the shoulder in Figure 6.14 when 4keV EB voltage was used, which will be discussed in detail. V-pits constantly show as dark spots in the SEM, panchromatic, and 450nm CL images, and higher contrast center surrounded by dark halos in the GaN emission CL. V-pits show as dark regions in the 440nm CL image. However, signals from V-pits are less sharp in the 440nm CL compared to the 450nm counterpart. This indicates that the 440nm emission maybe related to the presence of V-pits, but not exactly caused by the V-pits. This double peak emission will be discussed in detail later.

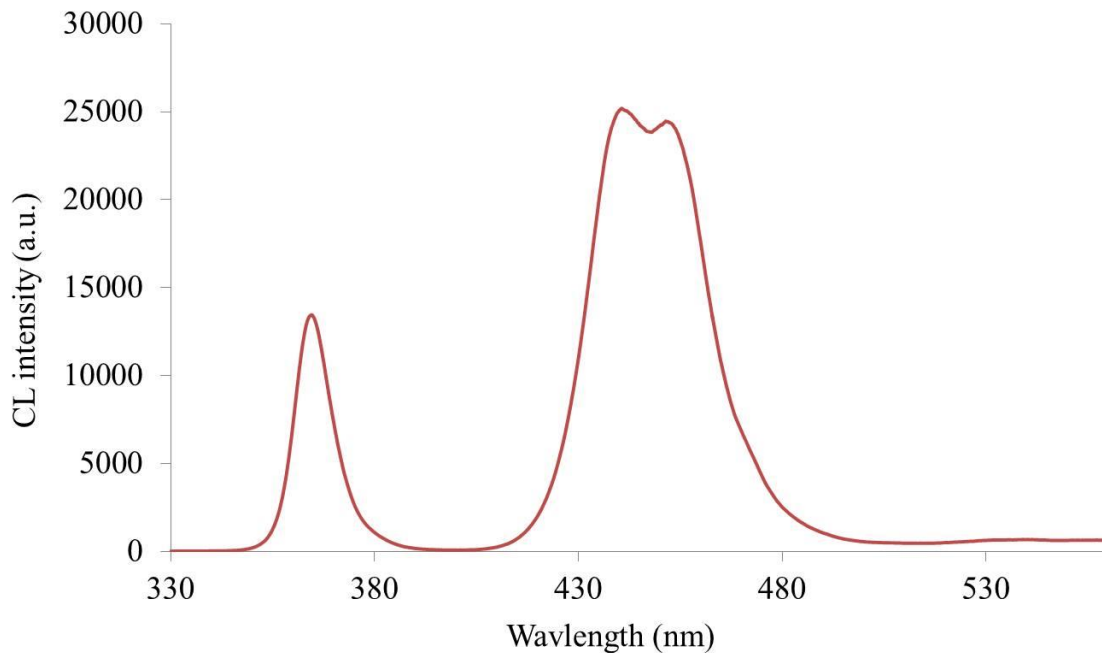


Figure 6.17: CL spectrum of A3 at 8keV EB voltage and 30um aperture size

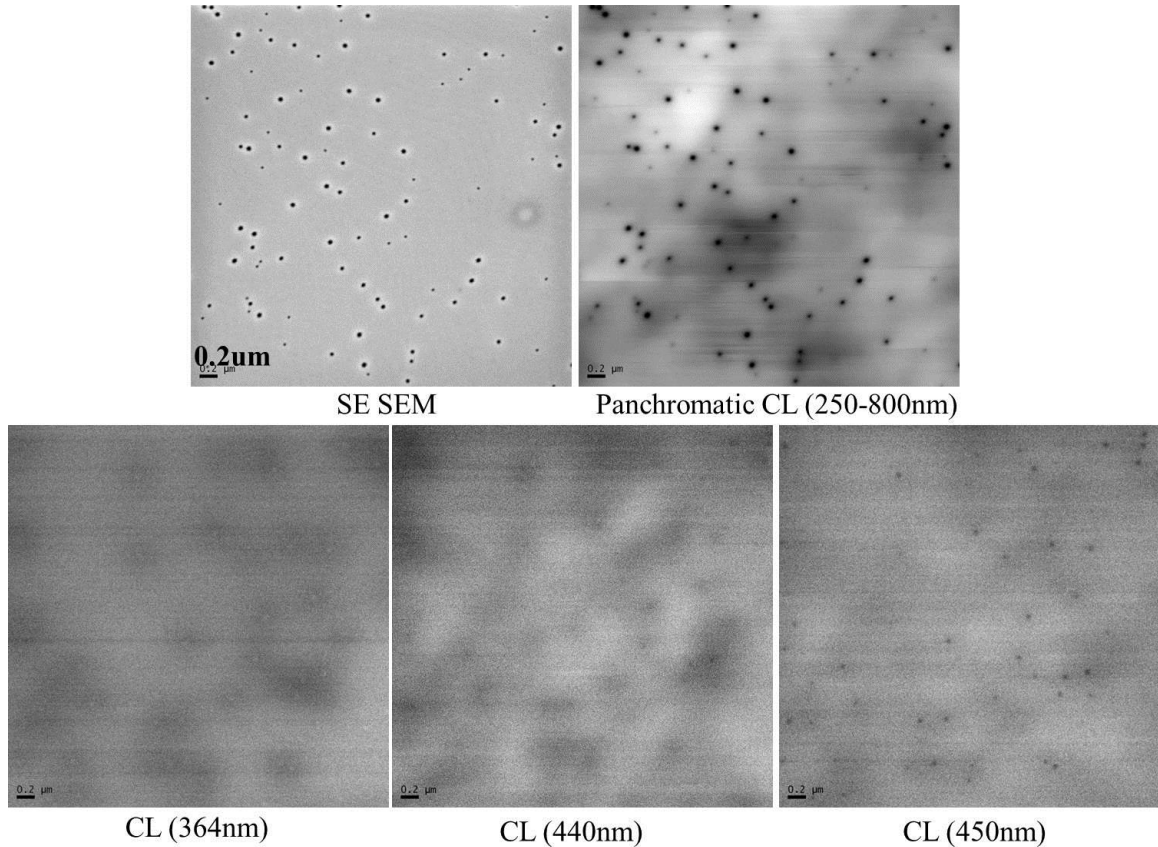


Figure 6.18: SE SEM, panchromatic CL, and monochromatic CL (at 362nm and 452nm) images of MQW sample A3 at 8keV EB voltage and 30μm aperture size

6.2.4.2 Spot CL Analysis

To study the luminescence of the regions with different contrasts at pit free areas in the CL images, spot CL analysis is performed using 2keV EB voltage which gives an EB penetration width of about 30nm. Figure 6.19 shows the secondary electron SEM image and corresponding panchromatic CL image taken from MQW sample A3 at 2keV EB voltage and 30μm aperture size. Other than V-pits, which show the darkest contrast in the CL image, luminescence fluctuations are also observed in the pit free areas. For simplification, we call the regions with relatively higher contrast bright spots, and those with relatively lower contrast dark spots. 8 spots were taken for spot CL analysis as

marked in the CL image. Spot 1, 3, 5, and 7 are from bright regions, and 2, 4, 6, and 8 from dark.

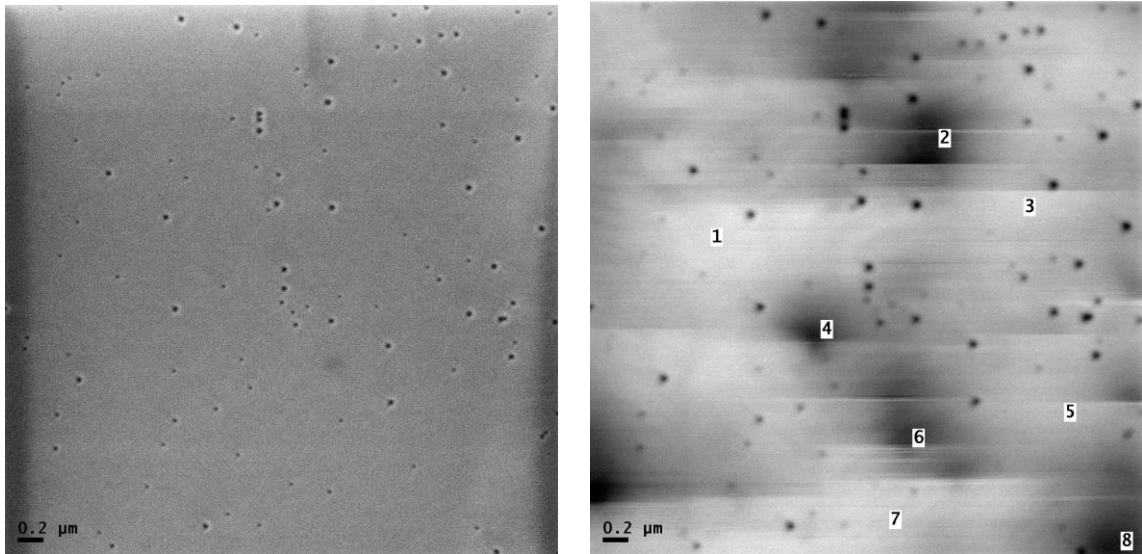


Figure 6.19: SEM (left) and panchromatic CL (right) images at 2keV EB voltage and 30um aperture size. In the CL image, spots 1, 3, 5, and 7 are from bright regions, and 2, 4, 6, and 8 dark.

Figure 6.20 (a) shows the CL spectrum of bright spot 1 and dark spot 2. A single peak emits at around 2.74eV is observed for both spot. The peak emission energies of all 8 spots are shown in Figure 6.20 (b). Bright spots constantly exhibit lower peak emission energy than the dark spots do, which is consistent with the reported results on bulk InGaN layer grown on sapphire and GaN substrates by using micron scale CL-EDX system [99] and CL-SEM system [100], and on InGaN/GaN MQW structure by using confocal microscope [101] and CL system [102]. The low emission energy bright spots may indicate that regions with higher luminescence have smaller bandgap thus better carrier localization.

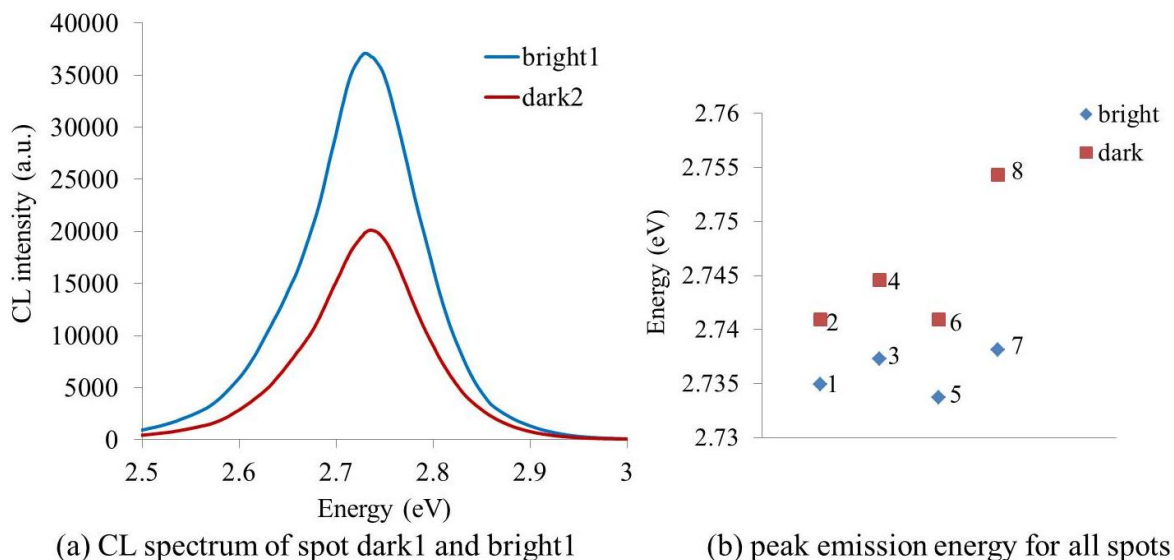


Figure 6.20: (a) CL spectrum of spot b1 and d1 and (b) the peak emission energies of all 8 spots

6.2.4.3 EB Voltage Dependent CL Analysis

Figure 6.21 shows the emission spectrums with EB rastering on a 4 μ m by 4 μ m sample size for EB voltages varying from 2keV to 8keV at 30 μ m aperture size. A same PMT voltage of -1100V is used in all the measurements so the CL intensities can be compared. According to Figure 5.5 and Equation (5-3), when EB voltage is increased from 2keV to 8keV at 30 μ m aperture size, the number of e-h pairs generated per second in the diffusion region N_{e-h} increases from 7.7×10^{10} to 5.4×10^{11} , and according to Figure 5.6, EB diffusion length increases from 30 μ m to 330 μ m. Therefore, it can be calculated that the current density decreases from $7.4\text{A}/\text{cm}^2$ to $0.1\text{A}/\text{cm}^2$, and the electron dose increases from $1.3 \times 10^{-4} \text{c}/\text{cm}^2$ to $2.4 \times 10^{-4} \text{c}/\text{cm}^2$. The current density and electron dose used in our experiments are considerably smaller than those used to study LEEBI effects on InGaN/GaN structures, i.e., electron beam induced In and Ga diffusion and thus the generation of new InGaN emission peak, as discussed in Section 4.3.

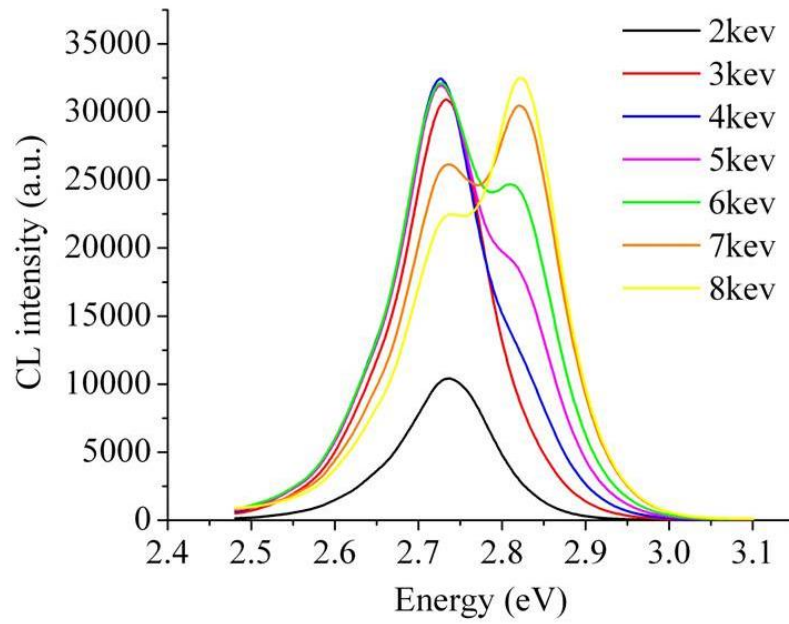


Figure 6.21: CL spectrum at 2-8keV EB voltages at 30um aperture size

The CL data have been corrected from system response, and then the peak emission energy, peak emission wavelength, Gaussian and Lorentzian broadening FWHM, and intensity ratio between the low energy (LE) peak and the high energy (HE) peak are obtained from Voigt fit into the CL curves and shown in Table 6.1.

Table 6.1: Voigt fitted CL data at 2-8keV at 30um aperture size

EB voltage (keV)	Peak energy (eV)	Peak wavelength (nm)	Gaussian FWHM (meV)	Lorentzian FWHM (meV)	FWHM (meV)	Peak intensity ratio I_{HE}/I_{LE}	
2	LE peak	2.738	452.6	83.9	56.2	117.9	
	HE peak						
3	LE peak	2.736	453.2	71.5	73.7	118.7	
	HE peak						
4	LE peak	2.736	453.3	60.8	87.3	119.8	
	HE peak						
5	LE peak	2.733	453.7	46.7	95.9	115.9	0.33
	HE peak	2.813	440.5	86.9	2.3E-15	86.9	
6	LE peak	2.734	453.5	33.2	102.7	113.1	0.58
	HE peak	2.815	440.5	96.8	4.5E-12	96.8	
7	LE peak	2.742	452.2	14.6	106.9	109.0	1.18
	HE peak	2.821	439.6	90.8	19.7	101.8	
8	LE peak	2.746	451.6	1.4E-3	106.7	106.7	1.72
	HE peak	2.821	439.6	84.8	29.3	101.5	

The discussion of Figure 6.21 and Table 6.1 are as following.

- (1) It is shown in Figure 6.21 that at 2keV and 3keV, only one emission peak around 2.74eV is distinguishably observed with increasing peak intensity, which results from the

increasing numbers of e-h pairs generated and increasing activation volume from increasing EB. This peak should be the MQW emission peak. Since at 2keV, the e-h pairs generated per second is 7.7×10^{10} , compared with the 1.5×10^9 photons generated per pulse in the PL measurement discussed before in Section 6.2.3, in which a double peak emission spectrum was observed, it seems that the absence of the 2.82eV peak does not result from the number of injected e-h pairs, but the depth of the interaction volume into the MQW layer.

(2) As shown in Figure 6.21, at 4keV, a shoulder at higher energy around 2.82eV starts to show up, and turns into a distinguished peak at 6keV. This trend of increasing HE peak intensity versus the LE peak can be clearly observed in the intensity ratio column of Table 6.1. Such a trend may be explained by that a radiative recombination center around 2.82eV exists at the bottom pairs of MQW which localizes more e-h pair with increasing EB voltage. If this is the case, then the competition for carriers between the localization centers at 2.82eV and 2.74eV should also be considered, as the areas with a smaller bandgap, or potential minima, will be filled before carrier recombination occurs more frequently in larger bandgap regions [99][103].

(3) At high EB voltage, i.e., 7keV and 8keV, the HE peak becomes dominant, which suggests the possible feature of more quantum size confined structures due to more efficient recombination [104] by Phonon Assisted Stimulated Emission as discussed in Section 2.3.3.3, and plus the possible electron beam induced indium diffusion into the HE sites [84].

(4) A wavelength red shift from 452.6nm to 453.7nm when increases EB voltage from 2keV to 5keV leads to the suspicion that bottom pairs of MQW have higher In

composition than the top pairs, which is consistent with the reported results that the concentration of the strain at the bottom of the MQW is higher due to either interface strain or the piezoelectric field [86] and thus leads to high In concentration. The relationship between strain and In concentration will be discussed more.

(5) A gradual blue shifted peak emission wavelength with increasing EB voltage from 5keV to 8keV is observed for the LE peak, which can be explained by combined effects of band filling and carrier screening of the QCSE introduced by the piezoelectric field as discussed in Section 2.3.4. Meanwhile, such a gradual blue shift is also observed for the HE peak, which suggests that it is possible that this unknown emission is from some other InGaN/GaN related structures which exhibit QCSE and piezoelectric field, for example, nanostructured compositional inhomogeneities like InGaN quantum size inhomogeneities which have larger effective bandgap than InGaN/GaN MQW. Interestingly, the blue shift observed in HE peak is smaller than that in the LE peak, which is consistently with the QCSE theory and reported experimental results that higher In content and/or larger InGaN thickness will both lead to higher piezoelectric field and thus more blue shift due to more carrier screening of the piezoelectric field [103][105][107].

(6) The LE peak turns from about half Gaussian half Lorentzian line shape to almost all Lorentzian with increasing EB voltage, while Gaussian line shape is constantly dominant for the HE peak. It is known that the CL process at individual energy level is a Lorentzian distribution, in which excitonic effects increase the oscillator strength at the band gap energy and remarkably decrease the emission line width [2][85]. However, the superposition of multiple radiative recombination levels, system responses and noises add

Gaussian broadening to the CL spectrum. The increasingly Lorentzian LE peak may be caused by the improved MQW effective bandgap uniformity over a larger interaction area and/or by the increasing e-h pair injection, the latter will be proved not related in the next Section. Meanwhile, the Gaussian distribution dominance in HE peak may be caused by the superposition of multiple radiative recombination energy levels, for example, the superposition of luminescence from InGaN quantum size structures of different sizes and In compositions.

The emission spectrum of the sample A3, B3 and C3 at 8keV EB voltage and 30um aperture size are shown in Figure 6.22. A same PMT voltage of -1100v is applied to all measurements. Double peak emission is observed in C3 as in A3, while not in B3, which is consistent with the room temperature PL measurement. Considering same amount of e-h pairs is generated for both measurements, not only the peak intensity of B3 doubles that of A3 and C3, the integration intensity at the MQW emission range of B3 also doubles that of the latter two samples. It indicates that HE peak competes with the LE emission and share the generated e-h pairs.

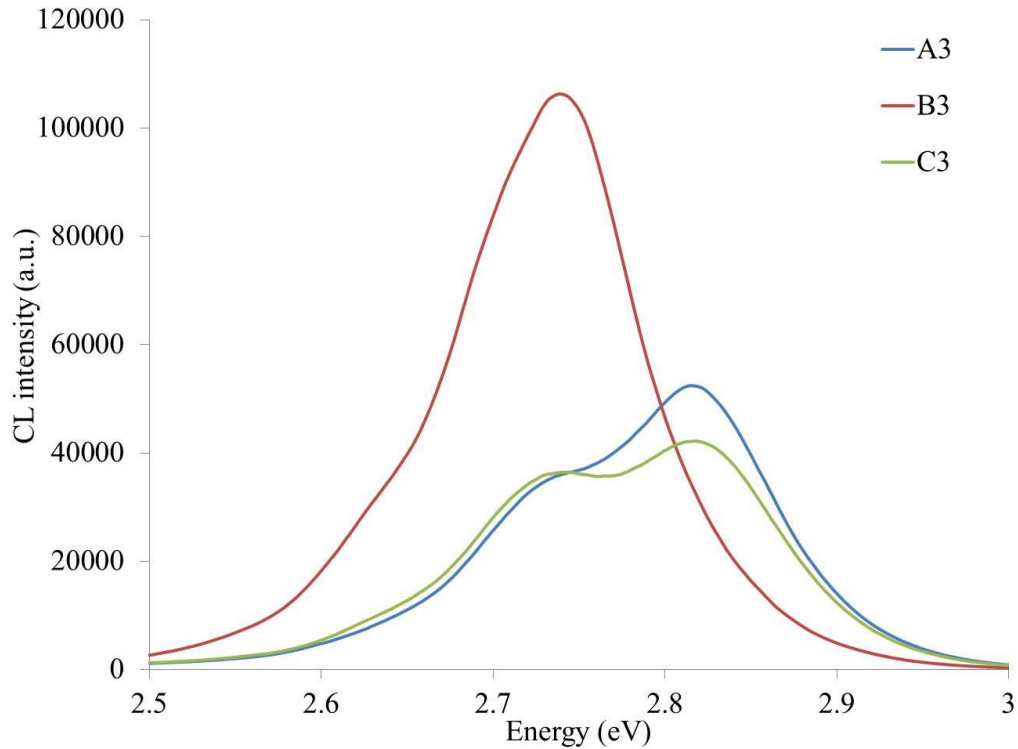


Figure 6.22: CL spectrum at 8keV EB voltage and 30um aperture size for sample A3, B3 and C3

6.2.4.4 Aperture Size Dependent CL

The aperture size dependent CL spectrum at 3keV is shown in Figure 6.23. A same PMT voltage of -1100v is applied to all the measurements so the CL intensities are comparable among all the curves. The Voigt fitted data after system response correction are shown in Table 6.2. According to Figure 5.5 and Equation (5-3), when increase aperture size from 30um to 120um at 3keV EB voltage, the number of e-h pairs generated per second in the diffusion region N_{e-h} increases from 1.3×10^{11} to 2.7×10^{12} , and EB diffusion length stays the same. It can be calculated that the current density is from $1.5A/cm^2$ to $31.7A/cm^2$, and the electron dose is from $1.5 \times 10^{-4} c/cm^2$ to $3.2 \times 10^{-3} c/cm^2$.

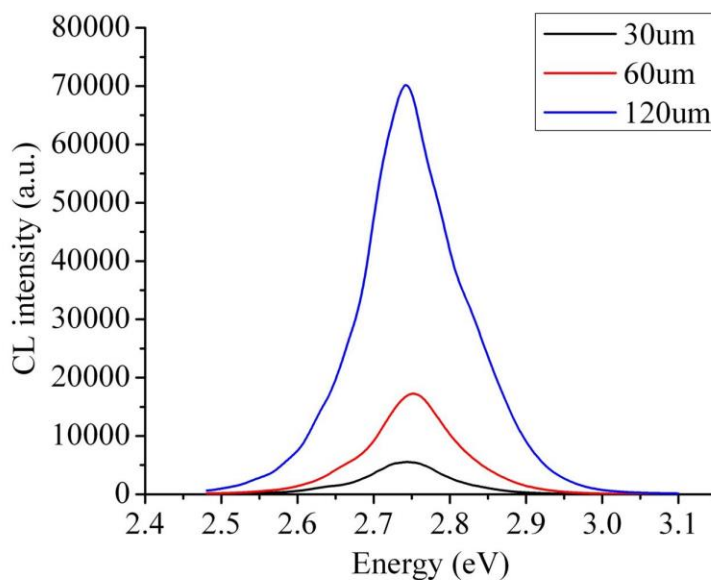


Figure 6.23: CL spectrum at 30um, 60um and 120um aperture sizes at 3keV EB voltage

Table 6.2: Voigt fitted CL data at 30, 60 and 120um aperture size at 6keV EB voltage

Aperture size (um)	Peak energy (eV)	Peak wavelength (nm)	Gaussian FWHM (meV)	Lorentzian FWHM (meV)	FWHM (meV)	Peak intensity (a.u.)	
30	LE peak	2.732	453.8	79.9	52.4	111.5	5707
60	LE peak	2.746	452.6	66.3	79.1	118.1	17526.6
120	LE peak	2.742	452.2	82.4	70.9	126.6	69017.5

Only LE emission peak at around 2.74eV is distinguishably observed in all three CL curves. At 120um aperture size, a shoulder at around 2.82eV can be vaguely observed, even though the e-h pair generated is higher than at 8keV EB voltage and 30um aperture

size, which indicates that the HE peak luminescence is dependent on the e-h generation depth in the MQW layer. Peak intensity increases with aperture size, i.e., increasing current density and N_{e-h} , since more e-h pairs are generated and recombine in the MQW. The blue shifts in peak wavelength from 30um to 120um aperture size are observed, which may be caused by the carrier screening of piezoelectric field. Besides, the almost half Gaussian and half Lorentzian line shaped LE peak is consistent with what was observed at 3keV in Table 6.1. The LE peak doesn't change into Lorentzian distribution dominant at high e-h pair injection at 120um aperture size. This proves that the changing of line shape of the LE peak observed in Table 6.1 was caused by the increasing EB interaction area in MQW, rather than increasing number of carriers injected.

The aperture size dependent CL spectrum at 6keV is shown in Figure 6.24. Since beam current increases a lot with aperture size, to prevent PMT from saturating, decreasing PMT voltages have been used for different aperture sizes, so only the intensity ratios are comparable. The Voigt fitted data are shown in Table 6.3. According to Figure 5.5 and Equation (5-3), when increase aperture size from 30um to 120um at 6keV EB voltage, the number of e-h pairs generated per second in the diffusion region N_{e-h} increases from 1.3×10^{11} to 7.0×10^{12} , and EB diffusion length stays the same. It can be calculated that the current density is from $0.1A/cm^2$ to $4.5A/cm^2$, and the electron dose is from $7.0 \times 10^{-5} c/cm^2$ to $4.0 \times 10^{-3} c/cm^2$.

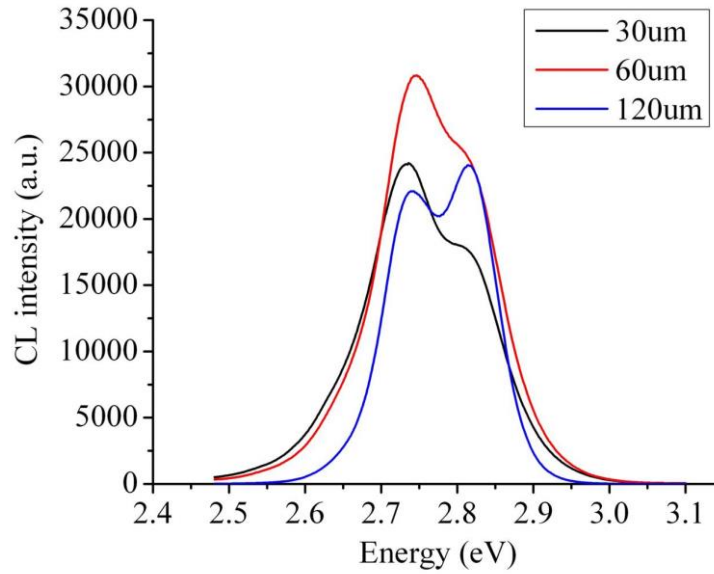


Figure 6.24: CL spectrum at 30um, 60um and 120um aperture sizes at 6keV EB voltage

Table 6.3: Voigt fitted CL data at 30, 60 and 120um aperture size at 6keV EB voltage

Aperture size (um)		Peak energy (eV)	Peak wavelength (nm)	Gaussian FWHM (meV)	Lorentzian FWHM (meV)	FWHM (meV)	Peak intensity ratio I_{HE}/I_{LE}
30	LE peak	2.734	453.5	45.5	97.6	116.4	0.47
	HE peak	2.807	441.8	91.1	2.87E-18	91.1	
60	LE peak	2.746	452.6	38.2	86.8	102.0	0.56
	HE peak	2.815	440.5	99.9	9.68E-18	99.9	
120	LE peak	2.741	452.3	61.1	34.2	81.4	1.10
	HE peak	2.817	440.1	73.9	6.0	77.1	

Both emissions at around 2.74eV and 2.82eV are distinguishably observed in all three

CL curves. Peak intensity ratio I_{HE}/I_{LE} increasing with aperture size indicates that more and more carriers radiatively recombine at the 2.82eV energy level. The blue shifts in both the LE peak wavelength and HE peak wavelength from 30um to 120um aperture size are observed again, which may be caused by the carrier screening of piezoelectric field. Besides, the half Gaussian and half Lorentzian line shaped LE peak and mostly Gaussian line shaped HE peak are also consistent with the observation before.

6.2.5 Time Resolved PL Analysis

Room temperature time resolved PL measurement is applied to the MQW sample A3 for multiple times. One set of temporal profiles of PL intensity at HE and LE peak energies, approximately 2.82eV and 2.74eV, respectively, is shown in Figure 6.25.

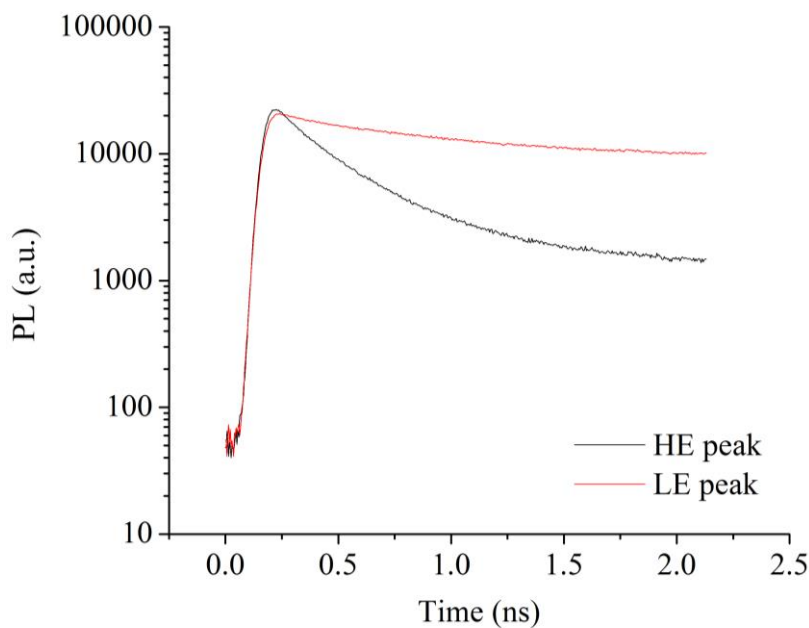


Figure 6.25: Time resolved PL curves at room temperature at HE and LE peak energies with a 5nm bandpass

The PL decay curves are fitted by double exponential function (6-1):

$$y = A_1 e^{-t/\tau_1} + A_2 e^{-t/\tau_2} + y_0, \quad (6-1)$$

where τ_1 and τ_2 are the lifetimes, and A_1 and A_2 are the decay coefficients, respectively.

Table 6.4 shows A_1/A_2 , τ_1 , and τ_2 values of 9 sets of TRPL data on sample A3 after double exponential fitting. The HE peak shows double exponential decays of average lifetime 0.13ns and 0.38ns, which indicate the relatively fast decay in the early stage and the slow decay in the extended stage, respectively. These two decay mechanisms are both dominate the carrier recombination at HE level since the decay coefficients are close, i.e. A_1/A_2 is close to 1. According to Reference [108][110], the two decay time phenomena is attributed to the carrier localization from weaker localized states, i.e., higher potential minimums, into stronger ones. Similarly, two average lifetimes of 0.75ns and 0.11ns at LE peak indicate the existence of two localization mechanisms. Recombination at the stronger localized states in this case, however, dominates the carrier recombination process, because the decay coefficient for the longer lifetime is larger, i.e., A_1/A_2 is significantly larger. In experiment 1, 2, and 5, there is even only one decay mechanism observed. These stronger localized states at LE level are mostly likely MQW, and weakly localized state is attributed to the InGaN/GaN interface fluctuations induced by threading dislocations [24]. Since localization sites associated with dislocations and other defects exhibit shorter carrier lifetimes [111], and the limiting factor of lifetime is considered to be mainly point defects or any other electronic nonradiative centers rather than dislocations [30], the carrier recombination sites at the HE level are expected to be more defective in point defects and/or any other electronic NRRCs than MQW. The two localization states at HE level suggest the possible existence of nanostructures with different In concentrations [112] which are bonded to locale defective regions.

Table 6.4: PL decay coefficients and lifetimes for HE and LE peaks

No.		A_1/A_2	τ_1 (ns)	τ_2 (ns)
1	HE peak	3.7	0.41	0.1
	LE peak	∞	0.73	
2	HE peak	2.6	0.39	0.12
	LE peak	∞	0.69	
3	HE peak	1.6	0.37	0.13
	LE peak	8.1	0.73	0.1
4	HE peak	1.5	0.36	0.13
	LE peak	7.8	0.74	0.09
5	HE peak	1.4	0.34	0.12
	LE peak	∞	0.63	
6	HE peak	0.9	0.36	0.14
	LE peak	4.7	0.81	0.14
7	HE peak	0.6	0.39	0.15
	LE peak	4.7	0.83	0.14
8	HE peak	0.7	0.37	0.14
	LE peak	5.2	0.8	0.12
9	HE peak	1.1	0.4	0.16
	LE peak	16	0.77	0.09

6.2.6 AFM-SCM Analysis

An AFM-SCM study on MQW sample A3 has been done and shown in Figure 6.26. A

strong correlation between V-pits and areas with capacitance can be observed, which indicates that there are charge accumulations at V-pits.

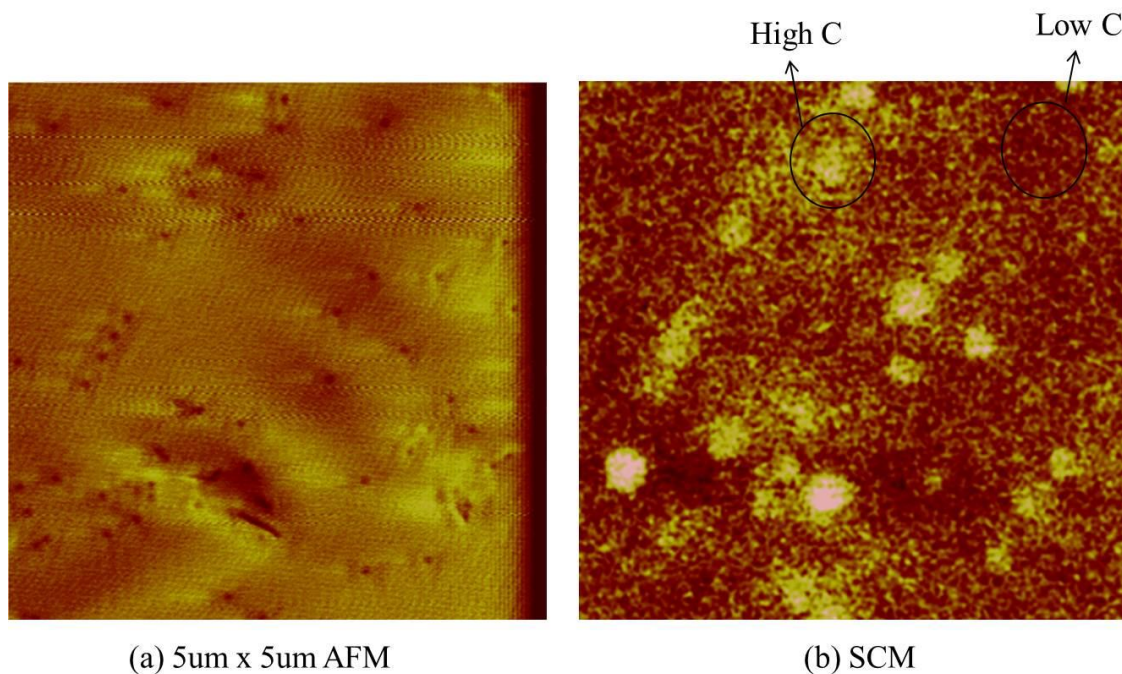


Figure 6.26: AFM image (a) and corresponding SCM image of MQW sample A3

To investigate what kind of charges accumulating at V-pit areas, the dependence of capacitance signals on the DC bias are studied on the sample--DC bias of -1v, 0v and +1v are applied to the sample stage. Figure 6.27 shows the SCM images at different DC biases. It is observed that when the sample bias changes from -1v to 1v, the SCM signal contrast decreases obviously. In another word, the capacitance at V-pit areas decreases with increasing DC bias from -1v to 1v. Figure 6.28 shows the SCM system diagrams when DC bias is at -1v and 1v. When sample is negatively biased as in Figure 6.28 (a), i.e., the SCM probe is positively biased, negative charges in the sample move toward the surface, which decrease the capacitor thickness and leads to higher capacitance. On the

other hand, when sample is positively biased as in Figure 6.28 (b), the probe is negatively biased. Negative charges in the sample get repelled from the surface, which results in increasing capacitor thickness and smaller capacitance. The situation is opposite for positive charges in the sample. Therefore, the charges accumulating at V-pit areas are negatively charged, which is consistent with reported results [34][40][42][47]. It suggested the existence of deep acceptor like trap states in the vicinity of the valence band associated with V-pits and the defects they originated from, such as Ga vacancy (V_{Ga}^{3-}) and ($V_{Ga}-O_N$) $^{2-}$ complexes.

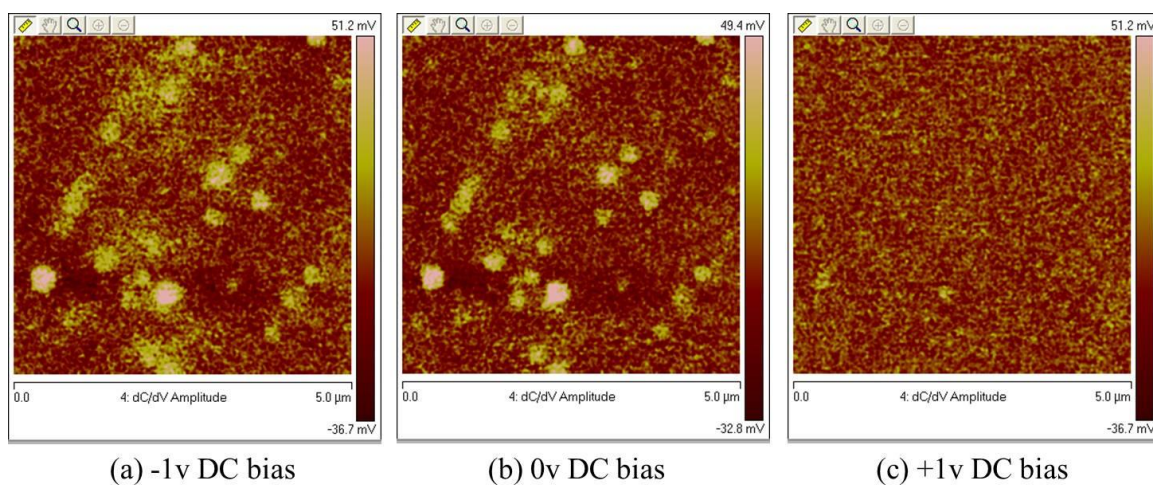


Figure 6.27: SCM images of the same area at -1v, 0v, and +1v DC bias

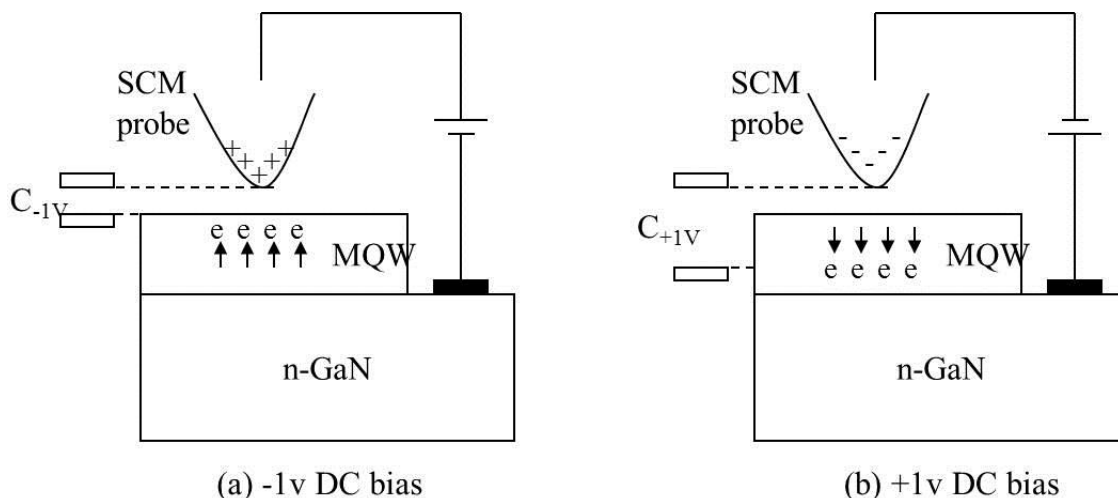


Figure 6.28: Schematic of the SCM system when the DC bias is at -1v (a) and +1v (b)

6.2.7 STEM Analysis

Figure 6.29 shows the cross section STEM image of the side wall of a V-pit on MQW sample A3. 4 pairs of quantum barrier/well can be clearly observed. 4 pairs of thinner MQW growth on the side wall of V-pit are also observed. Consider the In composition is same for both the thick MQW structure on the (0001) plane and the thin MQW structure on the side wall (1 0 -1 1) plane, the thin MQW structure is expected to show higher energy emission. But according to CL spectrum at 2keV, in which no blue emission shoulder to the (0001) MQW emission peak is observed, either the In composition in the thin MQW on (1 0 -1 1) plane is higher to compensate effective bandgap change caused by the smaller well thickness or the thin MQW emission is too weak to be detected.

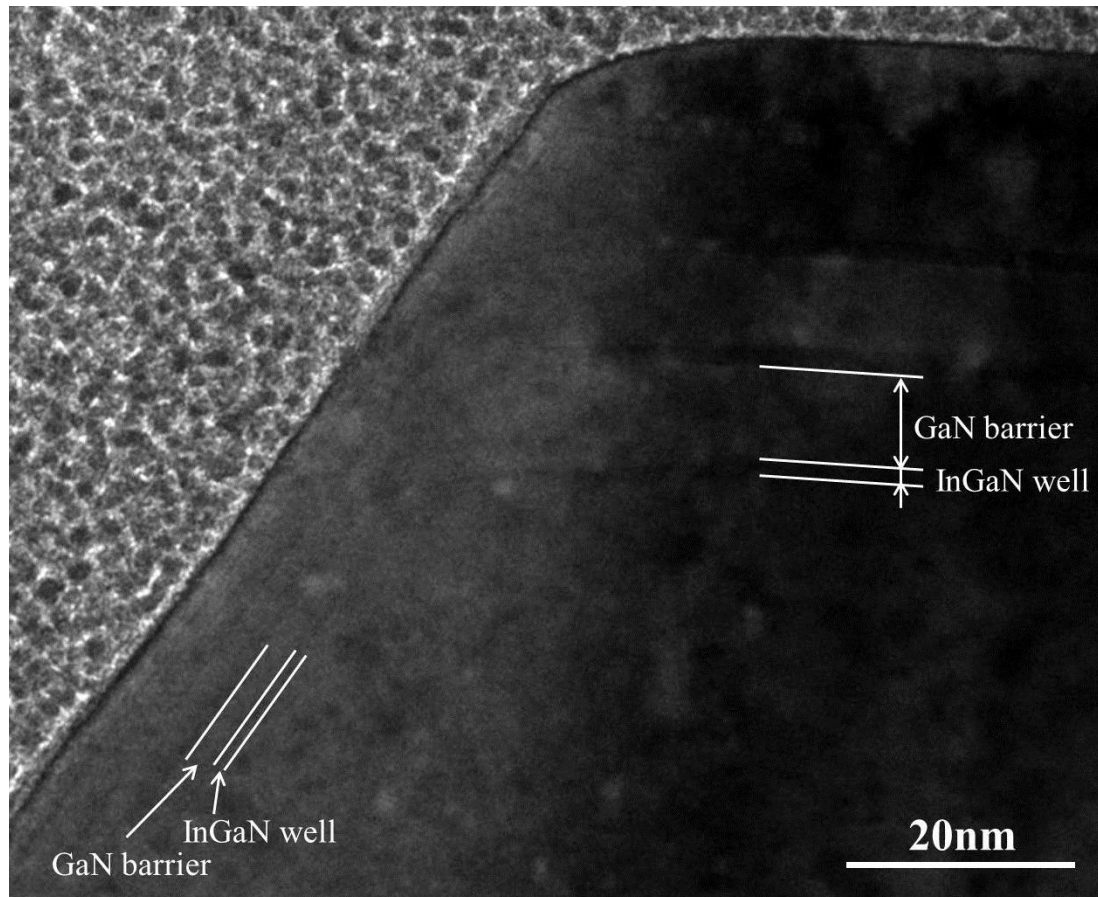


Figure 6.29: Cross section TEM image of MQW A3 at a V-pit

Even though there are negative charges, for example, point defects, accumulating around V-pit, as suggested in Section 6.2.6, the formation of thin quantum well layers on the wall of V-pit confined carriers from trapping into the defects and recombining nonradiatively [36][39].

6.2.8 SIMS Analysis

If SIMS is applied for MQW structure, the impurity levels will be extremely high at the surface, i.e., the top pair of MQW, because surface impurities are moved further into the sample due to the knock-on effect or atomic mixing created by the sputtering process. This high impurity artifact will affect the results in the thin MQW layers. Therefore,

SIMS is applied to the LED sample A1 and B1 to trace the atomic concentration profile of In, O, H, and C down from the surface. For clearer discussion and easier understanding, we put this part here in the MQW Section 6.2 instead of LED Section 6.4.

The SIMS profiles are shown in Figure 6.30. O, H, and C are common impurities in the growth process from precursors and residual vacuum, and cannot be excluded. Experimental data clearly shows that O, H, and C are involved in the defect-impurity complex in GaN system and act as efficient NRRCs [113][114]. Indium is measured as a marker for the MQW positions, left of which are p-AlGaN and p-GaN layers and right of which n-GaN layer. 4 pairs of MQW in A1 and 6 pairs of MQW in B1 are clearly observed. However, due to the small well and barrier thickness and relatively high sputtering rate and high ion beam energy of SIMS, in concentrations in those fine layers are not trustable.

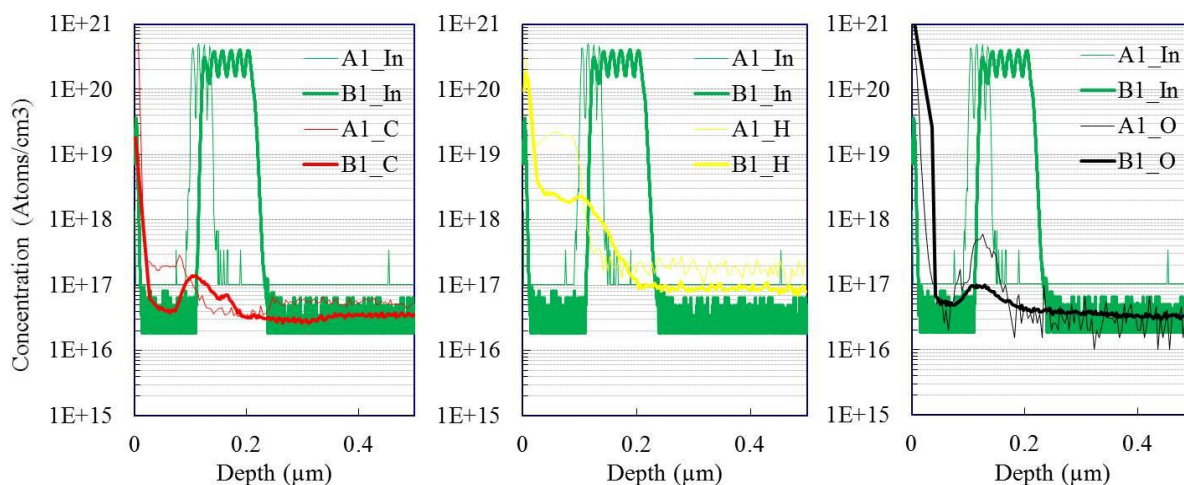


Figure 6.30: SIMS profile for In, C, H, and O on LED sample A1 and B1

C concentration profiles behave similarly in both samples. H concentration profiles

have the same trend in both samples, but the concentration in A1 is about 2 times of that in B1. In sample B1, O concentration is relatively high at the AlGaN/MQW interface and then decreases gradually through the layers, which is very common as the AlGaN is a known gatherer for O. In sample A1, however, O concentration peak is at the center of the MQW layer, and the integrated O concentration is 6.33 times of that for B1 in the MQW layer. Besides, it is observed that the high O concentration happens at the bottom side of the 4-pair MQW structure, and remain high at the MQW/n-GaN interface. The high O concentration in the MQW layer of A1 can be caused by the rougher GaN/InGaN interface thus more defective nature of the films, indicated by the XRD data, and/or the lower InGaN growth temperature [115].

Since two samples have similar C concentration profiles, and H in GaN based systems does not produce impurity luminescence itself, but broadens the luminescent band relative to the C-related or other point defect related peak [113], it is suspicious that the existence of the HE peak in sample A3 (and also A1 which will be discussed later) is related to the extremely high and abnormal O concentration profile in the MQW layer.

It is know that under the N-rich conditions used in InGaN/GaN MOCVD epitaxial process, O impurity is easily incorporated [116][117] and O_N^+ is a common form of shallow donor [44][113][118]. It has been reported that O implantation in GaN leads to tremendous defect density, a recombination of vacancies and interstitials, which is even higher than the implanted ion density [119]. Therefore, it is very possible that the extremely high O concentration in the MQW layer of sample A1 leads to a highly defective MQW structure. With the favorable deep acceptor, Ga vacancy (V_{Ga}^{3-}) under N-rich growth conditions [42], ($V_{Ga}-O_N$)²⁻ complexes are formed, which, according to

first-principles total energy calculations, is a very stable vacancy-impurity complex in the GaN system, as strong Ga-O bonds can be formed [44][86][120]. The atomic geometry of the V_{Ga}^{3-} and $(V_{\text{Ga}}\text{-O}_\text{N})^{2-}$ complex are shown in Figure 6.31, the number giving the increase in the bond strength in % [120].

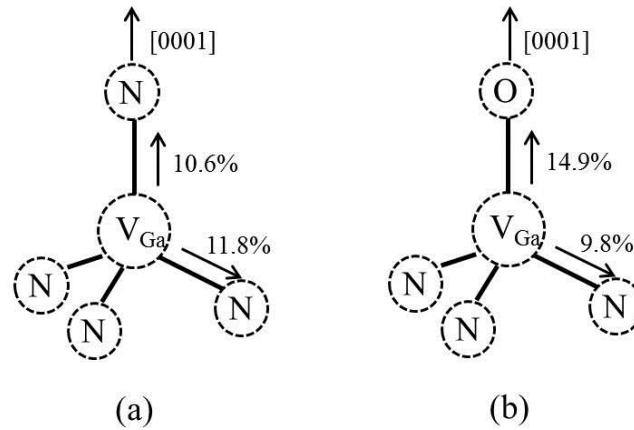


Figure 6.31: Atomic geometry of the V_{Ga}^{3-} and $(V_{\text{Ga}}\text{-O}_\text{N})^{2-}$ complex

O and C impurities and the induced vacancy-impurity complexes are all defined as point defects, which in one of the most efficient strain relaxation mechanisms. Point defects (i) decreases the energy required for dislocation formation and assists the propagation of dislocations in the material, which improves the strain relieving rate and/or causes atom rearrangements in strained layers resulting in strain relieving [16], just like dislocation, V-pit, and other defects do [20][54][95][98].

It is well known as the compositional pulling effect that in InGaN/GaN system, in atoms are pulled from InGaN by compulsive strain and segregate at strain relaxed regions [91][121]. Cross section HRTEM of InGaN/GaN MQW is reported by others in Ref. [122], in which threading dislocation and V-pit are observed. It can be seen that indium

rich clusters with diameter range from 5 to 12 nm aggregate near those defects as a consequence of the compositional pulling effect. It is reported by a great many researchers and groups that the stress field resulted from point defects, dislocations and other defects enhance the migration of In atoms toward defects and thus enhances the indium incorporation [65][97][118][122][129]. The high density of In rich clusters in the vicinity of defects suggests that carriers are trapped in these segregations before structural defects capture them. [122]

Therefore, it is proposed that InGaN nanostructures form around the $(V_{Ga}-O_N)^{2-}$ complex point defect. Since point defects are known to preferably cluster around Dislocations and other defects, which are suggested by the AFM-SCM data and other literature [40][42][47], a big percentage of this InGaN quantum structure may form around the V-pits and other defects in the MQW.

6.2.9 Summary of Double Peak InGaN Emission

To summarize all the results discussed in Section 6.1 and 6.2, a LE emission peak around 2.74eV and a HE emission peak around 2.82eV, both in the InGaN emission range, are observed for MQW samples A3 and C3. We attribute the LE emission to the InGaN/GaN MQW structure, and the HE emission to the InGaN/GaN quantum size structures formed surrounding the $(V_{Ga}-O_N)^{2-}$ point defects mainly at the bottom pairs of MQW layer, due to the strain relaxation by the point defects and the compositional pulling effect on In.

The discussions are summarized as below:

(1) Room temperature PL and CL spectrum show that both LE and HE emissions exist in MQW A3 and C3, but not B3. Since the current density and electron dose used in CL are

too small to cause the formation of a new electron beam induced HE InGaN emission peak, the double peak emission is considered to be intrinsic to the MQW samples.

(2) Bulk GaN sample A4 doesn't exhibit the HE emission peak, but the MQW sample A3 does. It indicates that the HE emission peak comes from the MQW layer of the structures.

(3) Both MQW samples grown on pity GaN (A4 on A3) and pit-free GaN (C4 on C3) exhibit the HE emission peak. It indicates that pits in bulk GaN are not the cause for the HE emission.

(4) At EB voltage smaller than 4keV, no matter how high the current density and electron dose are, only LE emission can be observed. It indicates that the LE emission comes from the InGaN/GaN MQW structure, and the HE emission is mainly initiated by radiative structures in the bottoms pairs of the MQW stack.

(5) The HE emission becomes stronger than the LE emission when current density and electron dose are high. It suggests that the HE emission comes from quantum size features which exhibit stronger carrier localization and more efficient recombination than MQW.

(6) A wavelength red shift from 452.6nm to 453.7nm was observed when increases EB voltage from 2keV to 5keV. It indicates that bottom pairs of MQW have higher in composition than the top pairs, which is consistent with the reported results that the concentration of the strain at the bottom of the MQW is higher due to either interface strain or the piezoelectric field [86] and thus leads to high In concentration.

(7) A gradual blue shift in both the LE and HE emission peak wavelengths with further increasing current density and electron dose were observed. It indicates that the HE emission also comes from some InGaN/GaN related structures which exhibit QCSE and

piezoelectric field like the MQW structure does.

(8) The HE emission is Gaussian broadened. It indicates that this emission is the superposition of multiple radiative recombination energy levels from InGaN/GaN structures of different bandgaps.

(9) Time resolved PL show that the LE emission has longer life time than the HE emission. It indicates that the HE emission sites are more defective.

(10) Two localization levels were observed in the TRPL data for the HE emission. It indicates the existence of InGaN/GaN structures of different bandgaps.

(11) SIMS data shown high O concentration in the bottom 3 pairs of MQWs in A3. It suggests high point defect density in those InGaN/GaN pairs.

This O-related HE InGaN emission shares e-h pairs which all should and are expected to contribute to the MQW emission, and thus decrease the quantum efficiency of the MQW structure.

Since O impurity incorporation is enhanced by defective nature of the films and low growth temperature, higher temperature growth of GaN quantum barriers, 860°C versus 760°C in B3 and A3, respectively, can be a solution to the double peak MQW structure [130]. This is consistent with the reported observation that In inclusions formed when GaN barrier is grown at temperature lower than 800°C [65] and more deep level defects are formed during low temperature GaN barrier growth [131][133].

6.3 AlGaIn Capped MQW Structure (Sample A2)

6.3.1 Surface Morphology

AFM image of AlGaIn capped MQW structure A2 is shown in Figure 6.32. V-pits which were observed on the MQW surface do not show up in the AlGaIn capped structure

any more. As discussed in Section 3.3.6, AlGa_N layer fills and buries the open pits.

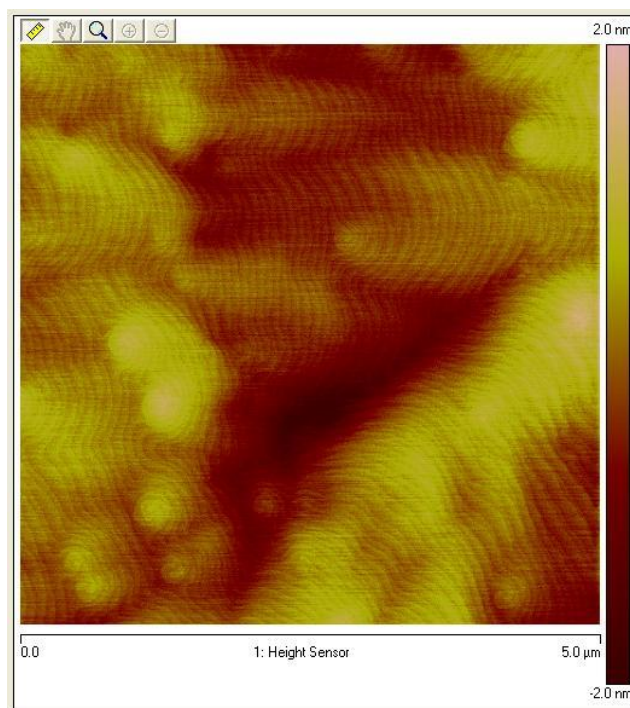


Figure 6.32: AFM images of AlGa_N capped MQW sample A2

6.3.2 SEM-CL Analysis

EB interaction in the AlGa_N capped MQW structure A2 is simulated by EFS and shown in Figure 6.33. Top white layer stands for the 20nm p-AlGa_N cap, then the light grey layer for the total of 4 pairs of GaN barriers, darker grey layer for the total of 4 pairs of InGa_N well, and the bottom darkest grey layer stands for bulk Ga_N. The approximate diffusion lengths at different EB voltages are listed too. The diffusion length increases with EB voltage as discussed in Section 5.2.5. SEM-CL studies at 2, 4, 6, and 8keV EB voltages at 30μm aperture size are done to sample A2 to study the luminescence properties of this structure. Monochromatic CL images are taken by using 1200L/mm

grating blazing at 500nm and 0.1mm slit width. The bandpass is about 2.5nm.

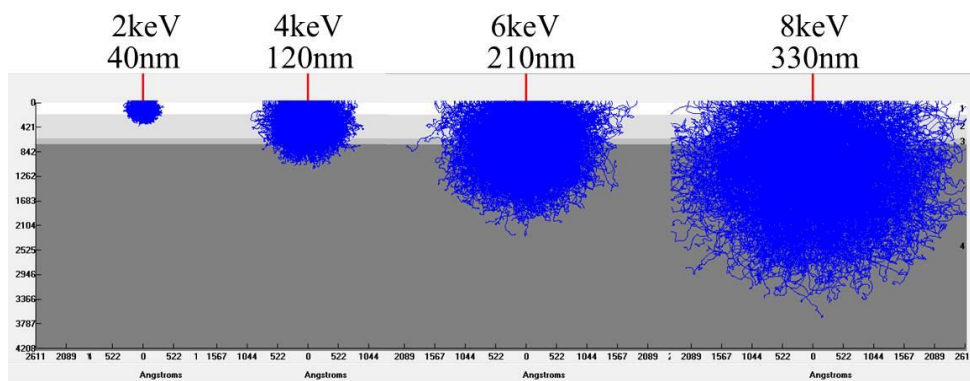


Figure 6.33: EB penetration volume in sample A2 simulated by EFS

Figure 6.34 shows the CL spectrums at AlGa_N emission, Ga_N emission, and MQW emission energy ranges when various EB voltages are applied to sample A2. The PMT voltage is -1100v for MQW emission and -1500v for AlGa_N and Ga_N emissions. In Figure 6.34 (a), the HE peak appears at 6keV EB voltage and gets stronger at 8keV, maintaining the same trend as observed for MQW sample A3 in Section 6.2. In Figure 6.34 (b), a left skewed Ga_N peak is observed due to the re-absorption of the higher energy side of the luminescence and the donor-valance band emission. AlGa_N emissions are very weak.

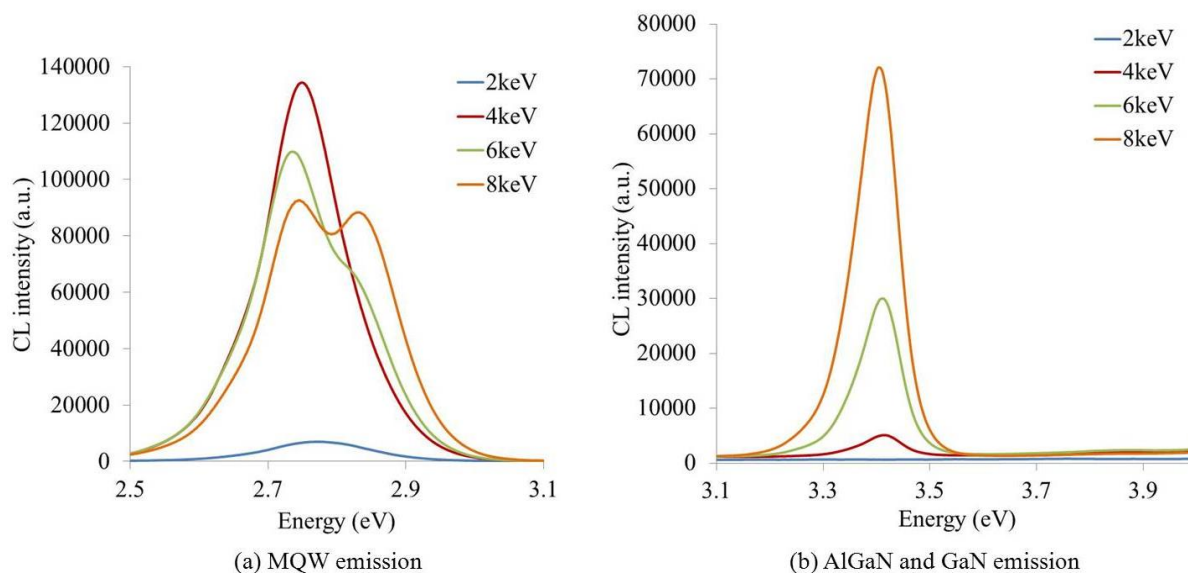


Figure 6.34: CL spectrums at MQW, AlGaN and GaN emissions at 2, 4, 6 and 8keV EB voltages for sample A2

Figure 6.35 shows the 4 μm by 4 μm SE SEM image and the corresponding panchromatic CL image and monochromatic CL images at 329nm, 363nm, and 448nm on A2 at 2keV EB voltage and 30 μm aperture size. SEM image shows pit free surface morphology just as AFM image does. Dark spots, however, are observed in the panchromatic CL image, and 448nm CL image, which corresponds to the top pairs of MQW emission at 2keV. Therefore, those dark spots seem to correspond to the V-pits in MQW layer. There is no observable signal in either the 329nm CL image due to the low AlGaN emission, or the 363nm CL image since EB has not diffused into bulk GaN layer yet. AlGaN emission is low due to two reasons. First, the AlGaN layer is only 20nm thick, so the interaction volume is small. Second, AlGaN is very not conductive, so it is difficult to generate carriers.

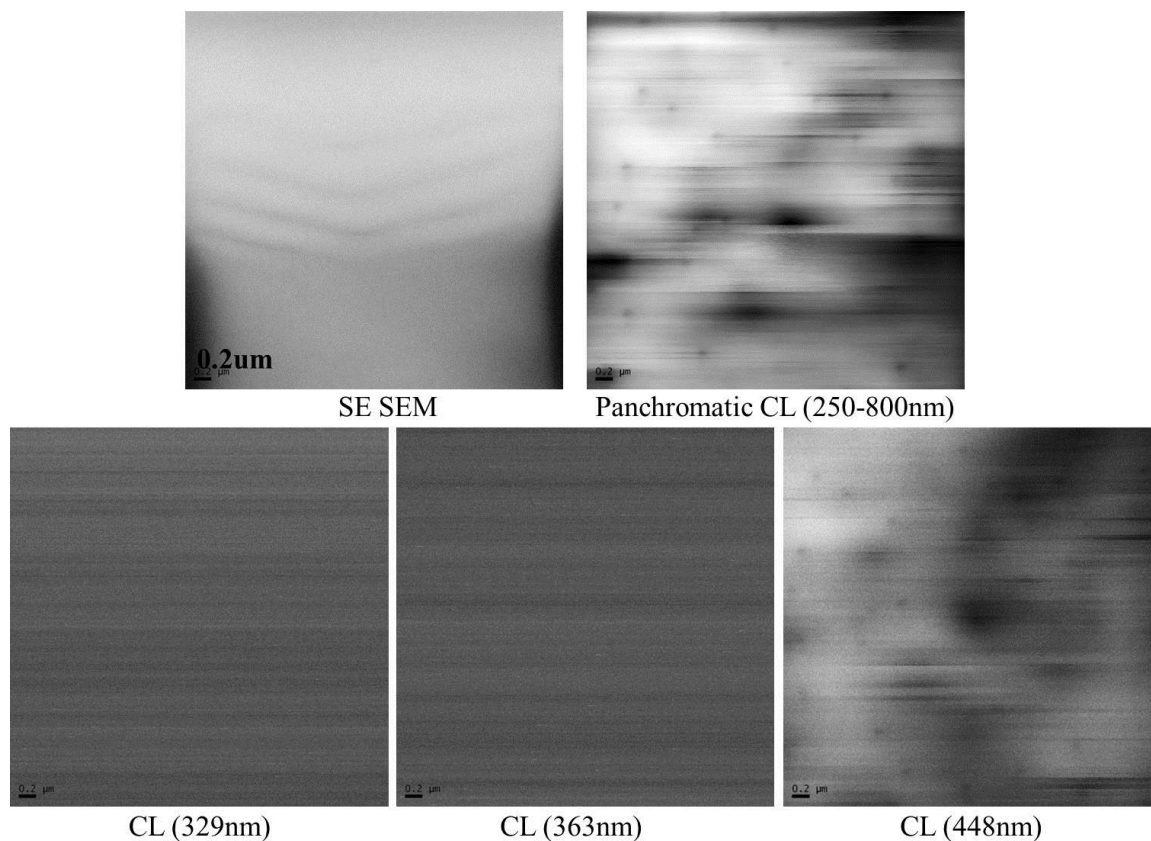


Figure 6.35: SE SEM, panchromatic CL, and monochromatic CL (at 329nm, 363nm and 448nm) images of AlGaN capped MQW sample A2 at 2keV EB voltage and 30um aperture size

Similar work is done on the A2 at 4keV EB voltage and 30um aperture size, at which EB diffuses into bulk GaN layer. Figure 6.36 shows the 4um by 4um SE SEM image and the corresponding panchromatic CL image and monochromatic CL images on A2 at 30um aperture size and 4keV EB voltages. Dark spots corresponding to the dislocations and other defects are observed in the GaN emission CL image. Areas shown as dark spots in the 363nm CL but not in the 450nm CL, an example being marked in red circles, correspond to the dislocations or other defects in bulk GaN which terminate before reaching the GaN/MQW interface and thus not form V-pits in MQW. Areas having dark

contrast in 450nm CL but not 363nm CL, an example being marked in blue circles, correspond to the MQW emission variations which are not directly caused by GaN quality beneath the areas. Still no AlGaIn emission contrast can be achieved.

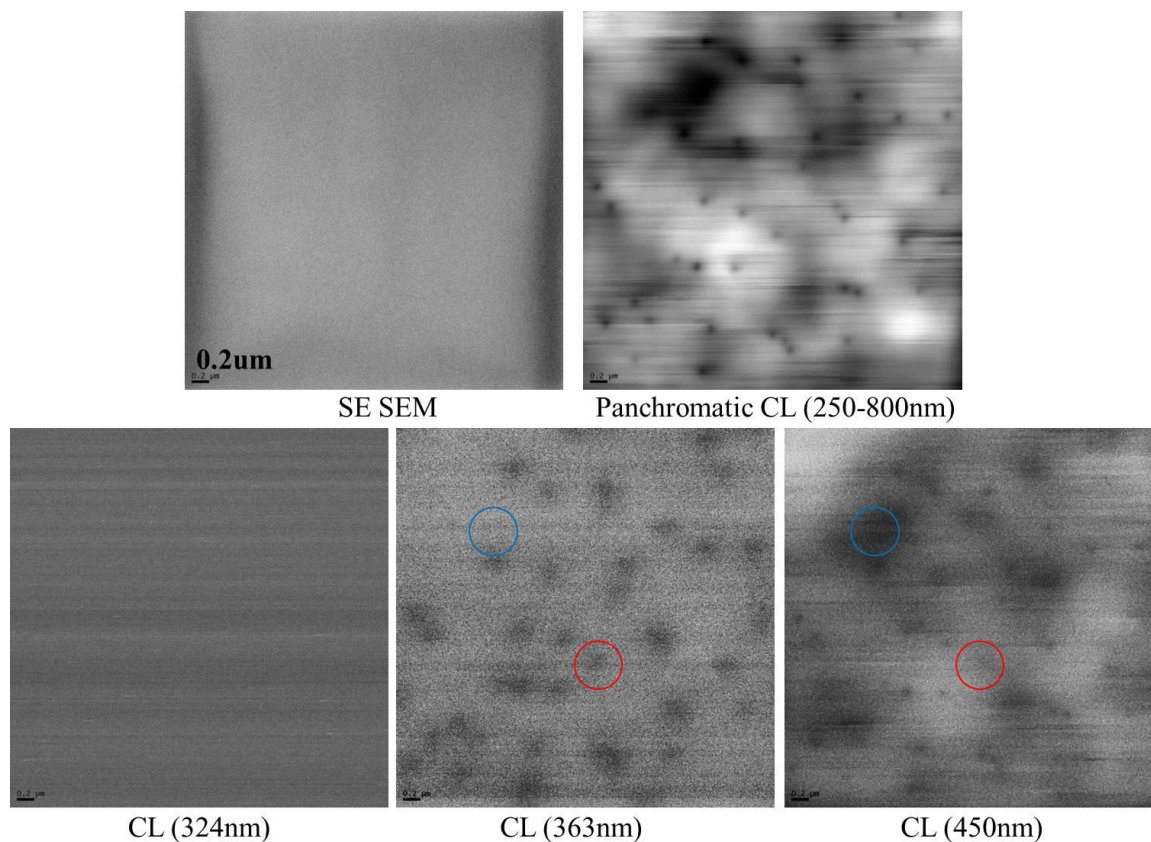


Figure 6.36: SE SEM, panchromatic CL, and monochromatic CL images of A2 at 4keV EB voltage and 30um aperture size

Figure 6.37 and 6.38 show the SEM-CL images at 6keV and 8keV EB voltages, respectively. The HE emission CL images, i.e., at around 440nm, show similar trend as the LE emission CL images do, but more variegated patterns, which indicates that the HE emission sources are more discretely distributed in space.

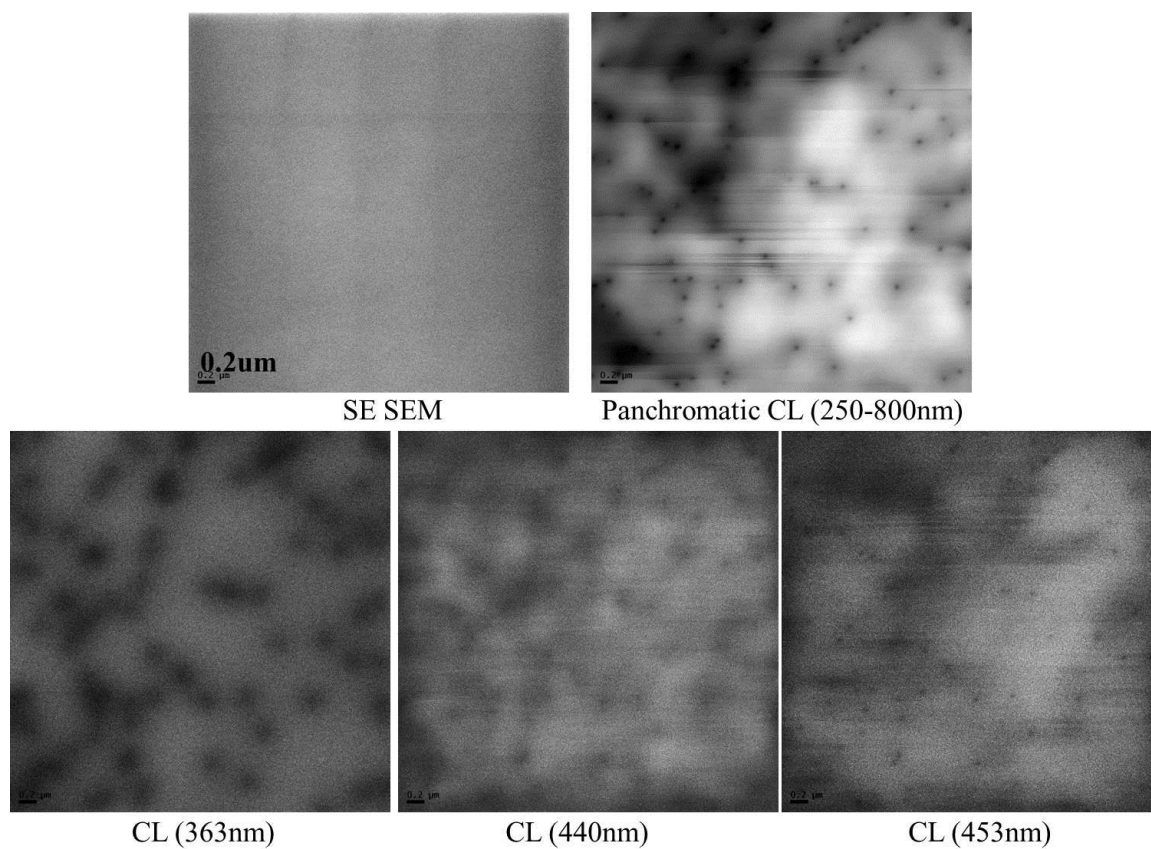


Figure 6.37: SE SEM, panchromatic CL, and monochromatic CL images of A2 at 6keV EB voltage and 30um aperture size

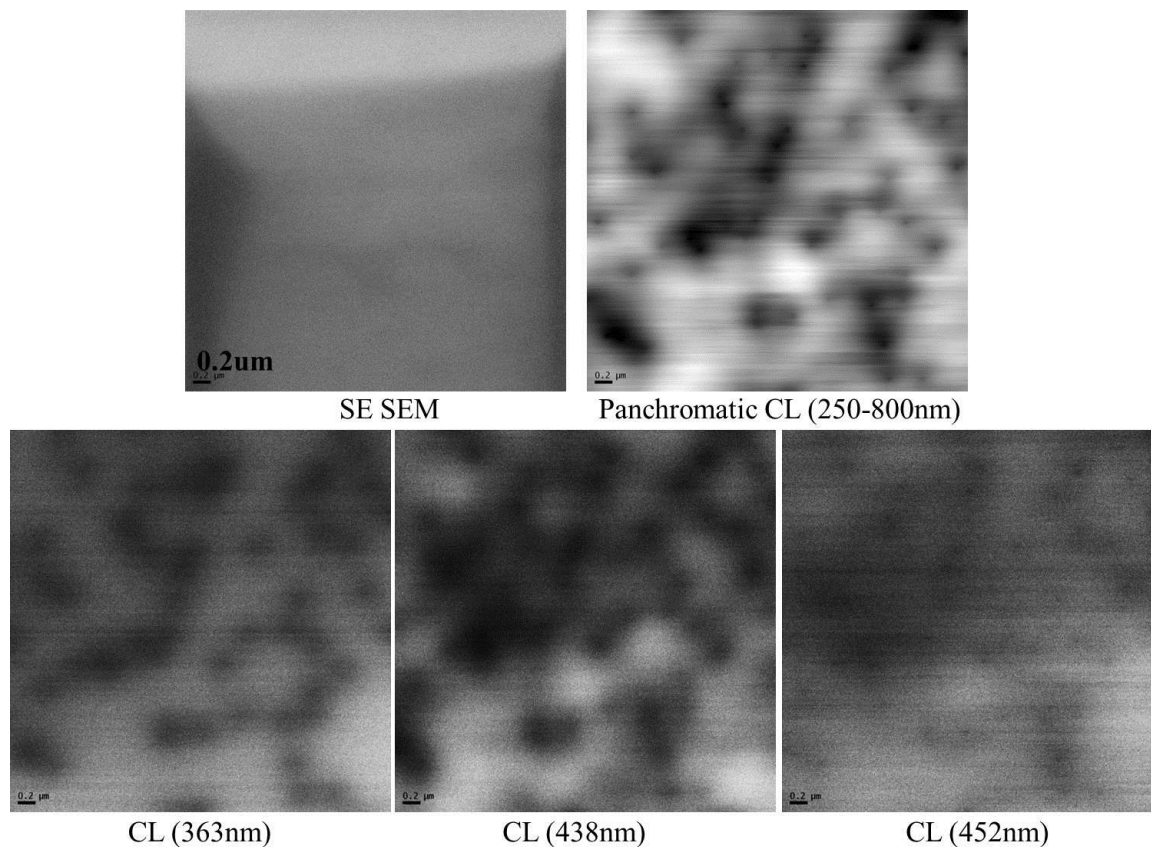
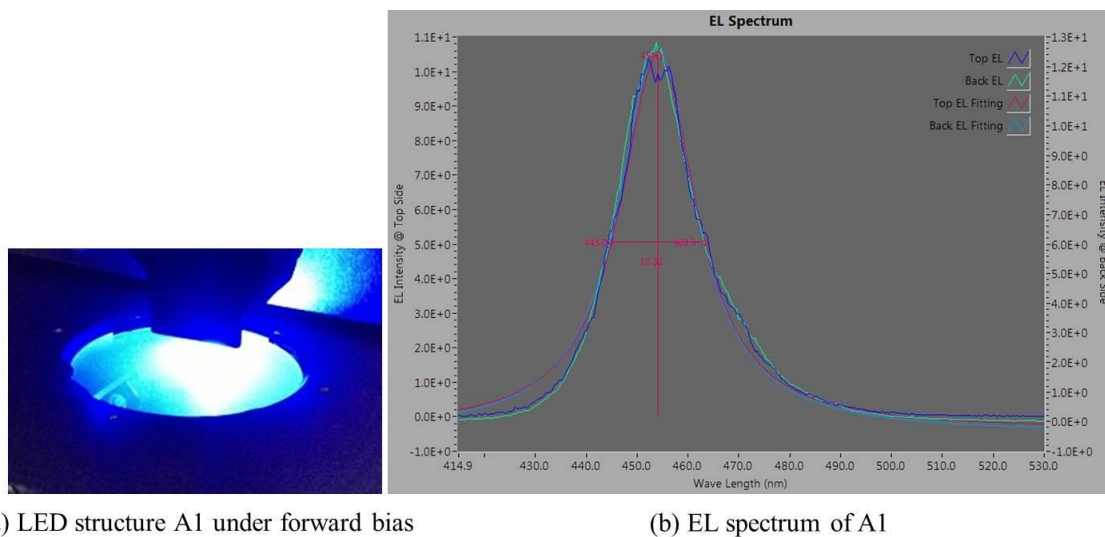


Figure 6.38: SE SEM, panchromatic CL, and monochromatic CL images of A2 at 8keV EB voltage and 30μm aperture size

6.4 LED As-grown Structure (Sample A1 and B1)

6.4.1 EL Test

Figure 6.39 (a) shows the picture of the LED As-grown sample A1 on the Maxmile EL mapper stage at forward bias. Blue emission around 452nm is observed, measured spectrum at 20mA driving current shown in Figure 6.39 (b). This shows that our LED sample grown under the chosen process conditions is electrically radiative.



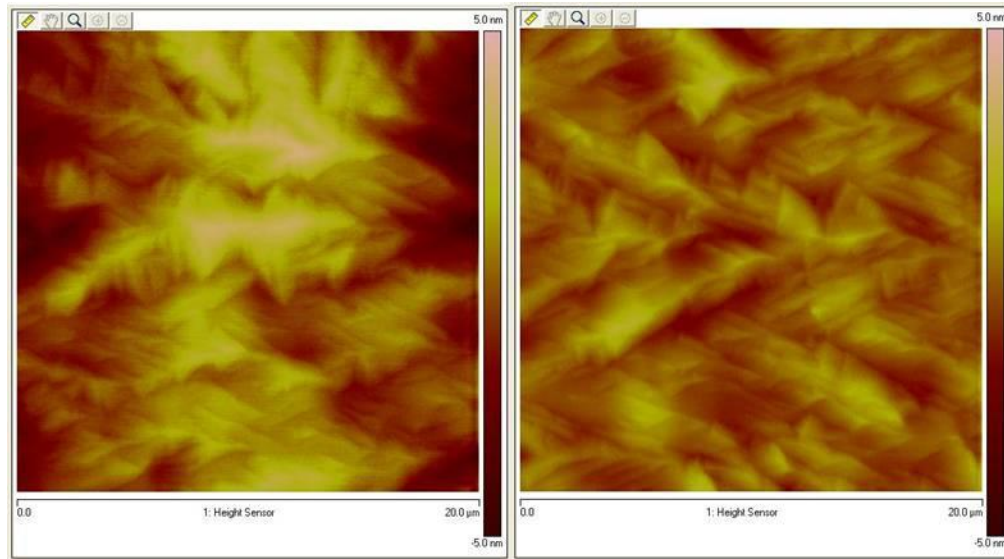
(a) LED structure A1 under forward bias

(b) EL spectrum of A1

Figure 6.39: Picture of LED As-grown sample A1 at forward bias (a) and measured EL spectrum at 20mA driving current (b)

6.4.2 Surface Morphology

20um by 20um AFM images of LED structures A1 and B1 are shown in Figure 6.40. Pit free surface and typical fish-bone morphology are observed for both samples.



(a) Sample A1

(b) Sample B1

Figure 6.40: AFM images of LED sample A1 and B1

6.4.3 SEM-CL Analysis

EB interaction in the LED structure A1 is simulated by EFS and shown in Figure 6.41. Top white layer stands for the 95nm p-GaN layer. Then from top to bottom are the 20nm p-AlGa_N electron blocking layer, a total of 4 pairs of GaN barriers, a total of 4 pairs of InGa_N well, and bulk Ga_N. Notice that due to the top 115nm of p-type AlGa_N and Ga_N layers, EB barely diffuses into the MQW layer even at 4keV voltage. The depth of EB penetration in LED structure A1 at 10keV is about the same in MQW structure A3 at 8keV. SEM-CL studies at 5, 6, 8 and 10keV EB voltages at 30μm aperture size are done to sample A1 to study the luminescence properties of this structure. Monochromatic CL images are taken by using 1200L/mm grating blazing at 500nm and 0.1mm slit width. The bandpass is about 2.5nm.

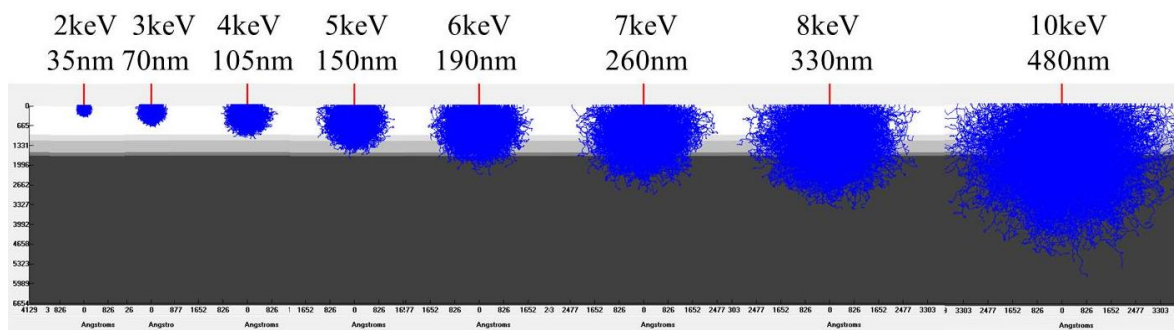


Figure 6.41: EB penetration volume in LED sample A1 simulated by EFS

Figure 6.42 shows the system response corrected CL spectrums of A1 when 30 μ m aperture size and various EB voltages are applied. A PMT voltage of -1100v is used for all measurement. Table 6.5 shows the Voigt fitted peak emission energies. A constant red shift in GaN emission is observed with increasing EB voltage due to the destruction of Mg–H pairs in p-GaN stimulated by EB irradiation [83]. GaN emission peaks are skew to the lower energy side due to the acceptor and donor levels introduced in the doped GaN. Single MQW emission peak are observed when 5keV and 6keV EB voltages are applied respectively, and an emission shoulder at HE starts to show up when the EB voltage increases to 8 and then 10keV. The appearance of HE peak in LED structure is very consistent with that in MQW sample. Blue shifts in both LE peak and HE peak with increasing EB voltages are observed due to the carrier screening of PZ field, which is also consistent with the data from MQW sample. One more thing to be mentioned is that at 8keV EB voltage, the peak wavelengths of the LE emission are 448.8nm, 451.2nm, and 451.6nm for LED structure A1, AlGaIn capped MQW structure A2, and MQW structure A3, respectively. This result indicates that the higher growth temperature of p-AlGaIn and

p-GaN top layers at 980°C can cause inter-diffusion and re-evaporation of In in the InGaN quantum well [134].

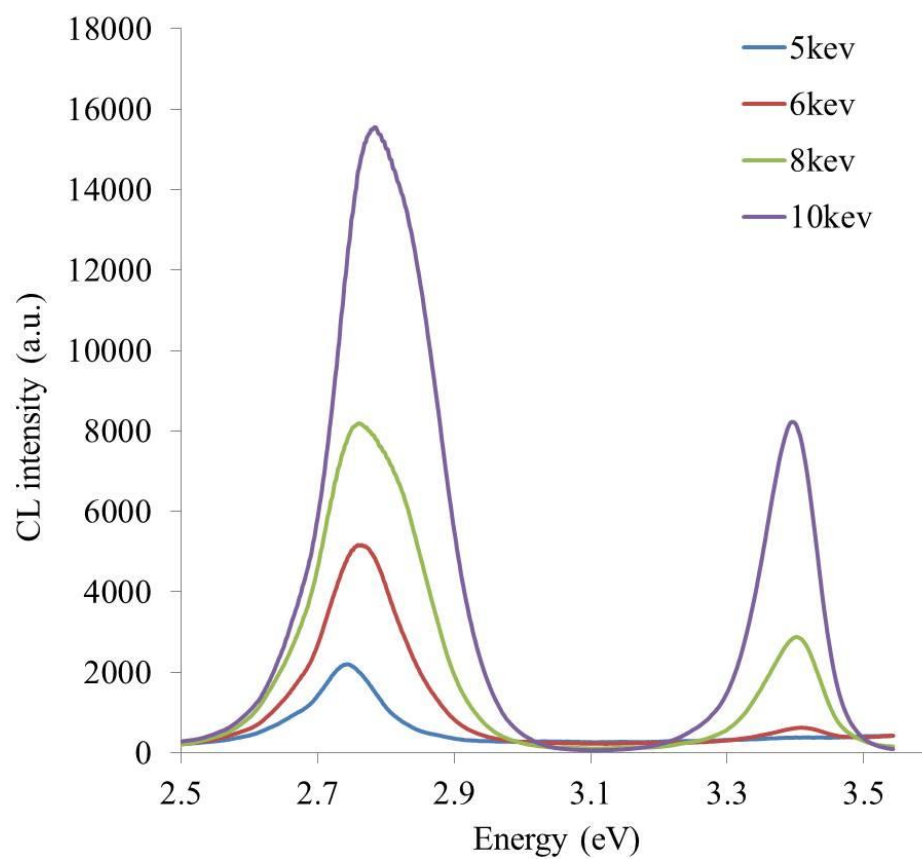


Figure 6.42: CL spectrums at 5, 6, 8 and 10keV EB voltages for LED structure A1

Table 6.5: Voigt fitted CL data at 5, 6, 8, and 10keV EB voltage at 30um aperture size

	GaN peak		LE peak		HE peak	
	eV	nm	eV	nm	eV	nm
5kev	3.414	363.2	2.747	451.4		
6kev	3.410	363.6	2.764	448.6		
8kev	3.403	364.4	2.763	448.8	2.817	440.2
10kev	3.397	365.0	2.785	445.2	2.826	438.8

Figure 6.43 shows the 4um by 4um SE SEM image and the corresponding panchromatic CL image and monochromatic CL images on A1 at 10keV EB voltage and 30um aperture size. SEM image shows pit free surface morphology just as AFM image does. Luminescence variations are observed in the panchromatic CL image. There is no observable signal in the 325nm CL image which corresponds to the low AlGaN emission, especially after the re-absorption of AlGaN emission by p-GaN cap layer. 365nm GaN emission CL image shows clear dark areas in the almost uniform GaN emission background. These dark areas refer to the Dislocations and other defects in GaN layer. The variegated pattern in the 445nm MQW emission CL image is caused by the nonradiative V-pits and luminescence variation pit free areas as shown in the CL images of MQW structure A3 before.

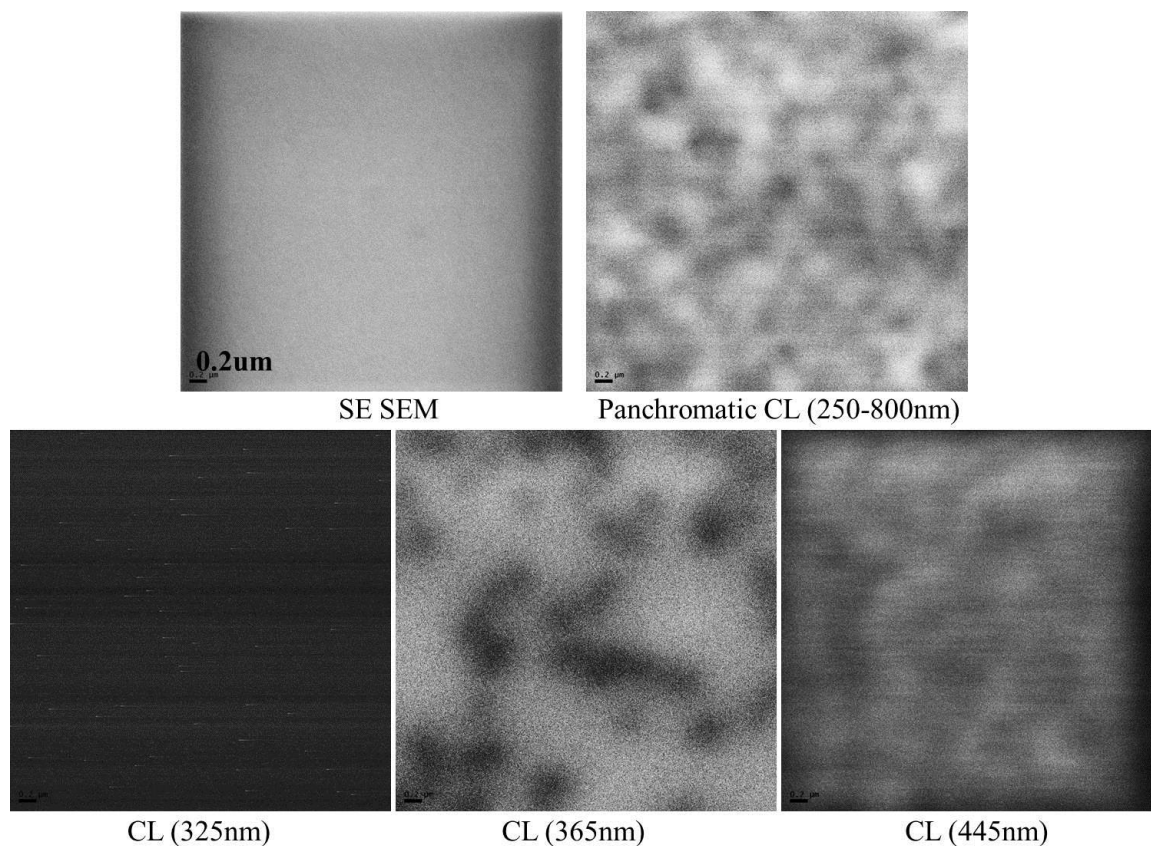


Figure 6.43: SE SEM, panchromatic CL, and monochromatic CL (at 325nm, 365nm and 445nm) images of LED A1 at 10keV EB voltage and 30μm aperture size

6.4.4 AFM-CAFM Analysis

An AFM-CAFM study on LED sample A1 with various reverse biases has been done and shown in Figure 6.44. Notice that in Figure (b) and (c), the color bar is from 450nA to 300nA, while 450nA to -400nA in Figure (d). High density of spots of early breakdown has been observed when the reverse bias increases. The high reverse current at those spots may owe to the defect-assisted tunneling by deep-level traps located in the active layer [32][135], i.e., the MQW layer in A1. This is consistent with the high O concentration and high point defects density in the MQW layer suggested in Section 6.3.

These point defects cause leakage and deteriorate the device performance [64].

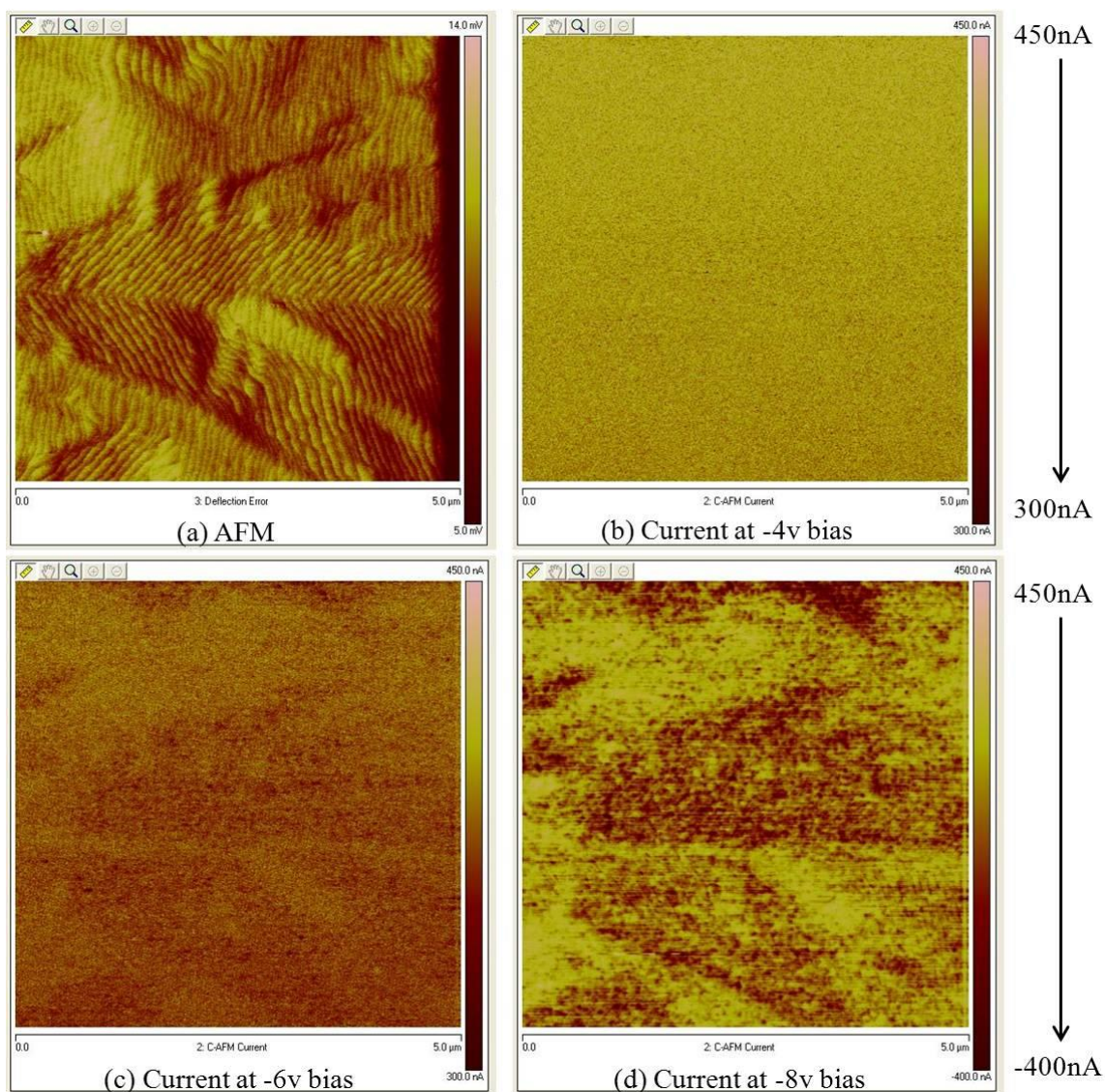


Figure 6.44: 5um by 5um AFM image of Al1 (a) and corresponding CAFM images at -4v (b), -6v (c), and -8v (d) biases

6.5 Summary of Experiment Results

The results discussed in this chapter are summarized as below:

(1) LED epitaxial structure has been studied optically layer by layer. V-pits form in

MQW structure regardless of whether the bulk GaN surface is pity or not. AlGa_N layer covers the open V-pits.

(2) CL has been used to show the nonradiative features hidden beneath the surface which otherwise would not have been observed in any surface morphology measurements, including defects on and beneath the bulk GaN surface capped by epi-layers on top, and V-pits capped by p-AlGa_N and p-GaN layers. These defects are proven to be NRRCs.

(3) Depth dependent CL and cross section STEM of bulk GaN show that threading dislocation density decreases as the thickness increases. GaN peaks skewing to the lower energy side were observed due to the donor-valance band emission.

(4) High resolution CL images showed submicron scale luminescence fluctuations of the MQW emission which enabled the study of In distribution in the InGa_N material. Higher luminescence intensity areas constantly exhibit lower peak emission energy, and thus are very likely to be areas with high Indium composition and stronger carrier localization.

(5) The double peak in the InGa_N emission range observed for sample series A and C was discussed and explained by formation of the InGa_N/GaN quantum size structures localized around point defects at the bottom of the MQW stack.

(6) Red shifting in GaN emission peak with increased current density and electron dose was observed in the CL spectrum of LED structure A1 due to the destruction of Mg–H pairs in p-GaN stimulated by EB irradiation.

(7) A constant blue shift in the peak emission wavelength of MQW was observed when p-AlGa_N and p-GaN layers are deposited onto the MQW structure. It indicates that the higher temperature p-AlGa_N and p-GaN growth causes inter-diffusion and re-evaporation of In in the InGa_N quantum well.

(8) Point defect induced HE InGaN emission not only reduces the quantum efficiency of the MQW structure, but also deteriorates the device performance by forming leakage paths.

CHAPTER 7: CONCLUSIONS

In the present work, a novel approach to investigate the submicron structural, optical and electrical properties of InGaN/GaN MQW LED structure grown by MOCVD system layer by layer has been introduced. The epitaxial process has been stopped at various points to study bulk GaN, InGaN/GaN MQW, p-AlGaN capped MQW structure, and full LED structure separately. GaN barrier layers have been grown at different temperatures (760°C and 860°C) to study the growth temperature dependent properties of the samples.

High resolution CL imaging (30um spatial resolution) and spectroscopy have been applied at various electron doses by changing EB voltage and aperture size separately. Due to the ability to study the luminescence properties in the vertical axis, i.e., at various depth from the surface, with CL system by varying the electron beam interaction volume, the NRRCs and luminescence fluctuations have been explored. Pits and dislocations on and beneath the bulk GaN surface and V-pits on the MQW surface have been studied and proven to be NRRCs. Submicron scale luminescence fluctuations of the MQW emission has been observed in CL images and correlated to local bandgap variation. The correlation between each layer (bulk GaN, MQW, p-AlGaN, and p-GaN) and the effects of the previous layer on the subsequent layers have been investigated.

Together with other characterization measurements, microscope, AFM and its

electrical modules (SCM and CAFM), XRD, PL, EL, TRPL, STEM, and SIMS, the effects of O impurity on the optical and electrical properties of the MQW active layer and on the device performance of the LED structure have been investigated by using high resolution SEM-CL system. The double peak in the InGaN emission range observed in some structures associated with MQW layer (LE emission peak around 2.74eV and HE emission peak around 2.82eV) have been studied in detail. From deduction, we attribute the LE emission to the InGaN/GaN MQW structure, and the HE emission to the InGaN/GaN quantum size structures formed surrounding the $(V_{\text{Ga}}-O_{\text{N}})^{2-}$ point defects mainly at the bottom pairs of MQW layers, due to the strain relaxation by the point defects and the compositional pulling effect on Indium.

This O impurity introduced HE InGaN emission shares e-h pairs which all should and are expected to contribute to the MQW emission, and thus decreases the quantum efficiency of the MQW structure and deteriorates the device property by forming leakage paths.

It has been found out that O impurity incorporation is enhanced by defective nature of the films and low growth temperature. Higher temperature growth of GaN quantum barriers at 860°C has been discovered to eliminate the unwanted HE emission and improve LED efficiency. This discovery is an important contribution in making better LED device in the future.

Some future work can be done based on the present work:

(1) For the dislocations and other defects hidden beneath the surface, CL technique has been applied to image them due to the lack of luminescence. In future work, chemical etching can be performed onto the structures to expose the hidden defects and correlate

the etch pits with the dark spots in the CL images that corresponds to dislocations and other defects beneath the surface.

(2) Consider the limitation of streak camera to measure lifetimes in a short time frame, more work can be done in time resolved PL measurement to measure lifetime in a longer time span which may provide slower decay in even more extended stage.

(3) All the CL imaging and spectrometry work has been performed under room temperature. In the future, temperature dependent CL measurement can be implemented to study the low temperature optical properties of the MQW samples and the CL quantum efficiencies of the HE and LE emission.

(4) Since only two different GaN barrier growth temperatures were used in the present work, future work can be done to more thoroughly investigate the GaN barrier growth temperature dependent optical and electrical properties of the MQW and LED structures. An optimized growth temperature may be explored to minimize the effects of impurities and thus optimize the optoelectronic performance of the MQW structures and LED devices.

REFERENCES

- [1] J. I. Pankove, and T. D. Moustakas, "Gallium Nitride I", *Semiconductors and Semimetals*, v 50, (1998)
- [2] M. Fox, "Optical Properties of Solids", Oxford Master Series in Condensed Matter Physics
- [3] E. F. Schubert, "Light-Emitting Diodes", second edition, Cambridge
- [4] P. Phattacharya, "Semiconductor Optoelectronic Devices", Prentice-Hall India
- [5] E. A. Berkman, "Growth and fabrication of GaN and In_xGa_{1-x}N based optoelectronic devices", Material Science and Engineering, North Carolina State University (2008)
- [6] R. Juza, H. Hahn, "Über die Kristallstrukturen von Cu₃N, GaN und InN Metallamide und Metallnitride", *Anorganische und Allgemeine Chemie*, v 234 (1938)
- [7] H. G. Grimmeiss, and H. Koelmans, "Analysis of p-n Luminescence in Zn-Doped GaP", *Phys. Rev.*, v 123, p 1939 – 1947 (1961)
- [8] W. Seifert, R. Franzheld, E. Butter, H. Sobotta, and V. Riede, "On the Origin of Free Carriers in High-conducting n-GaN", *Crystal Research and Technology*, v 18, p 383 (1983)
- [9] J. I. Pankove, E. A. Miller, and J.E. Berkeyheiser, "GaN blue light-emitting diodes", *Journal of Luminescence*, v 5, p 84 (1972)
- [10] A. P. Alivisatos, "Semiconductor Clusters, Nanocrystals, and Quantum Dots", *Science*, v 271, 933-937 (1996)
- [11] M. C. Daniel and D. Astruc, "Gold Nanoparticles: Assembly, Supramolecular Chemistry, Quantum-Size-Related Properties, and Applications toward Biology, Catalysis, and Nanotechnology", *Chem. Rev.*, v 104, 293-346, (2004)
- [12] A. D. Yoffe, "Low-dimensional systems: quantum size effects and electronic properties of semiconductor microcrystallites (zero-dimensional systems) and some quasi-two-dimensional systems", *Advances in Physics*, v 51, n 2, 799-890 (2002)
- [13] M. E. Sayed, "Small Is Different: Shape-, Size-, and Composition-Dependent Properties of Some Colloidal Semiconductor Nanocrystals", *Acc. Chem. Res.*, v 37, 326-333 (2004)

- [14]N. Holonyak, D. W. Nam, W. E. Plano, K. C. Hsieh, "Photopumping of Quantum Well Heterostructures at High or Low 0: Phonon-Assisted Laser Operation," J. Phys. Chem., v 94, 1082-1087 (1990)
- [15]S. D. Benjamin, Y. C. Lo, and R. M. Kolbas, "Time-Resolved Phonon-Assisted Stimulated Emission in Quantum-Well Heterostructures", IEEE Transactions on Electron Devices, v 16, n 2 (1999)
- [16]K. L. Bunker, "Development and application of electron beam induced current and cathodoluminescence analytical techniques for characterization of Gallium Nitride-based devices", Material Science and Engineering, North Carolina State Univeristy (2004)
- [17]A. F. Vyatkin, "The role of point defects in strain relaxation in epitaxially grown SiGe structures", Thin Solid Films, v 508, 90-95 (2006)
- [18]Hadis Morkoc, "Handbook of nitride semiconductors and devices. Volumn 1: materials properties, physics and growth", WILEY-VCH erlag GmbH & Co. KGaA, Winheim (2008)
- [19]L. Sugiura, Dislocation Motion in GaN Light-emitting Devices and Its Effect on Device Lifetime, Journal of Applied Physics, v 81, 1637 (1997)
- [20]J. C. Zhang, D. S. Jiang, Q. Sun, J. F. Wang, Y. T. Wang, J. P. Liu, J. Chen, R. Q. Jin, J. J. Zhu and H. Yang, "Influence of Dislocations on Photoluminescence of InGaN/GaN Multiple Quantum Wells", Applied Physics Letters, v 87, 071908 (2005)
- [21]S. J. Rosner, E. C. Carr, M. J. Ludowise, G. Girolami, and H. I. Erikson, "Correlation of Cathodoluminescence Inhomogeneity with Microstructural Defects in Epitaxial GaN Grown by Metalorganic Chemical-vapor Deposition", Applied Physics Letter, v 70, 420 (1997)
- [22]Y. S. Choi, J. H. Park, S. S. Kim, H. J. Song, S. H. Lee, J. J. Jung, and B. T. Lee, "Effects of Dislocations on the Luminescence of GaN/InGaN Multi-quantum-well Light-emitting-diode Layers", Material Letter, v 58, 2614 (2004)
- [23]S. J. Henley, and D. Cherns, "Cathodoluminescence Studies of Threading Dislocations in InGaN/GaN as a Function of Electron Irradiation Dose", Journal of Applied Physics, v 93, 3934 (2003)
- [24]H. B. Yu, H. Chen, D. Li, J. Wang, Z. G. Xing, X. H. Zheng, Q. Huang, and J. M. Zhou, "Influence of Threading Dislocations on the Properties of InGaN-based Multiple Quantum Wells", Journal of Crystal Growth, v 266, 455 (2004)
- [25]L. Macht, J. L. Weyher, A. Grzegorzcyk, and P. K. Larsen, "Statistical Photoluminescence of Dislocations and Associated Defects in Heteroepitaxial GaN

- Grown by Metal Organic Chemical Vapor Deposition”, *Physical Review B*, v 71, 073309 (2005)
- [26] T. Sugahara, H. Sato, M. Hao, Y. Naoi, S. Kurai, S. Tottori, K. Yamashita, K. Nishino, L. T. Romano, and S. Sakai, “Direct Evident that Dislocations are Non-Radiative Recombination Centers in GaN”, *Japanese Journal of Applied Physics*, v 37, 398 (1998)
- [27] M. S. Jeong, J. Y. Kim, Y. W. Kim, J. O. White, E. K. Suh, C. H. Hong, and H. J. Lee, “Spatially Resolved Photoluminescence in InGaN/GaN Quantum Wells by Near-field Scanning Optical Microscopy”, *Applied Physics Letter*, v 79, 976 (2001)
- [28] P. A. Crowell, D. K. Young, S. Keller, E. L. Hu, and D. D. Awschalom, “Near-field Scanning Optical Spectroscopy of an InGaN Quantum Well”, *Applied Physics Letter*, v 72, 927 (1998)
- [29] J. Liu, N. R. Perkins, M. N. Horton, J. M. Redwing, M. A. Tischler, and T. F. Kuech, “A Near-field Scanning Optical Microscopy Study of the Photoluminescence from GaN Films”, *Applied Physics Letter*, v 69, 3519 (1996)
- [30] S. F. Chichibu, H. Marchand, M. S. Minsky, S. Keller, P. T. Fini, J. P. Ibbetson, S. B. Fleischer, J. S. Speck, J. E. Bowers, E. Hu, U. K. Mishra, S. P. DenBaars, T. Deguchi, T. Sota, and S. Nakamura, “Emission mechanisms of bulk GaN and InGaN quantum wells prepared by lateral epitaxial overgrowth”, *Applied Physics Letter*, v 74, 1460 (1999)
- [31] T. Hino, S. Tomiya, T. Miyajima, K. Yanashima, S. Hashimoto, and M. Ikeda, “Characterization of Threading Dislocations in GaN Epitaxy Layers”, *Applied Physics Letter*, v 76, 3421 (2000)
- [32] X. A. Cao, K. Topol, F. S. Sandvik, J. Teetsov, P. M. Sandvik, S. F. LeBoeuf, A. Ebong, J. Krechmer, E. B. Stokes, S. Arthur, A. E. Kaloyeros, and D. Walker, “Influence of Defects on Electrical and Optical Characteristics of GaN/InGaN-based Light-emitting Diodes”, *Proceedings of SPIE, Solid State Lighting II*, v 4776, 105 (2002)
- [33] D. Cherns, S. J. Henley, and F. A. Ponce, “Edge and Screw Dislocations as Nonradiative Centers in InGaN/GaN Quantum Well Luminescence”, *Applied Physics Letter*, v 78, 2691 (2001)
- [34] Y. Chen, T. Takeuchi, H. Amano, I. Akasaki, N. Yamada, Y. Kaneko, and S. Y. Wang, “Pit Formation in GaInN Quantum Wells”, *Applied Physics Letter*, v 72, 710 (1998)
- [35] S. Mahanty, M. Hao, T. Sugahara, R. S. Q. Fareed, Y. Morishima, Y. Naoi, T. Wang, and S. Sakai, “V-shaped Defects in InGaN/GaN Multiquantum Wells”, *Material Letter*, v 41, 67 (1999)

- [36] S. D. Lester, F. A. Ponce, M. G. Craford, and D. A. Steigerwald, "High Dislocation Densities in High Efficiency GaN-based Light-emitting Diodes", *Applied Physics Letter*, v 66, 1249 (1995)
- [37] A. Verikov, M. Kuball, and A. V. Nurmikko, "Near-field Optical Study of InGaN/GaN Epitaxial Layers and Quantum Wells", *Applied Physics Letter*, v 72, 2645 (1998)
- [38] S. D. Lester, F. A. Ponce, M. G. Craford, and D. A. Steigerwald, "High Dislocation Densities in High Efficiency GaN-based Light-emitting Diodes", *Applied Physics Letter*, v 66, 1249 (1995)
- [39] L. Sugiura, "Dislocation Motion in GaN Light-emitting Devices and Its Effect on Device Lifetime", *Journal of Applied Physics*, v 81, 1637 (1997)
- [40] P. J. Hansen, Y. E. Strausser, and A. N. Erickson, "Scanning Capacitance Microscopy Imaging of Threading Dislocations in GaN Films Grown on (0 0 0 1) Sapphire by Metalorganic Chemical Vapor Deposition", *Applied Physics Letters*, v 72, 2247 (1998)
- [41] D. C. Look and J. R. Sizelove, "Dislocation Scattering in GaN", *Physical Review Letters*, v 82, 1237 (1999)
- [42] K. Leung, A. F. Wright, and E. B. Stechel, "Charge Accumulation at A Threading Edge Dislocation in Gallium Nitride", *Applied Physics Letter*, v 74, 2495 (1999)
- [43] S. M. Lee, M. A. Belkhir, X. Y. Zhu, and Y. H. Lee, "Electronic Structures of GaN Edge Dislocations", *Physical Review B*, v 61, 16033 (2000)
- [44] J. Elsner, R. Jones, M. I. Heggie, P. K. Sitch, M. Haugk, T. Frauenheim, S. Oberg, and P. R. Briddon, "Deep Acceptors Trapped at Threading-edge Dislocations in GaN", *Physical Review B*, v 58, 12571 (1998)
- [45] C. Youtsey, L. T. Romano, and I. Adesida, "Gallium Nitride Whiskers Formed by Selective Photoenhanced Wet Etching of Dislocations", *Applied Physics Letter*, v 74, 797 (1998)
- [46] C. Youtsey, L. T. Romano, R. J. Molnar, and I. Adesida, "Rapid Evaluation of Dislocation Densities in n-type GaN Films Using Photoenhanced Wet Etching", *Applied Physics Letter*, v 74, 3537 (1999)
- [47] F. A. Ponce, D. P. Bour, W. Gotz, and P. J. Wright, "Spatial Distribution of the Luminescence in GaN Thin Films", *Applied Physics Letter*, v 68, 57 (1996)

- [48] P. Kozodoy, J. P. Lbbetson, H. Marchand, P. T. Fini, S. Keller, J. S. Speck, S. P. DenBaars, and U. K. Mishra, "Electrical Characterization of GaN p-n Junctions with and without Threading Dislocations", *Applied Physics Letter*, v 73, 975 (1998)
- [49] E. G. Brazel, M. A. Chin, and V. Narayanamurti, "Direct Observation of Localized High Current Densities in GaN Films", *Applied Physics Letter*, v 74, 2367 (1999)
- [50] J. Elsner, R. Jones, R. K. Sitch, V. D. porezag, M. Elstner, T. Frauenheim, M. I. Heggie, S. Oberg, and P. R. Briddon, "Theory of Threading Edge and Screw Dislocations in GaN", *Physical Review Letters*, v 79, 3672 (1997)
- [51] R. H. Moss and J. S. Evans. "A new approach to MOCVD of indium phosphide and gallium-indium arsenide." *Journal of Crystal Growth*, v 55, 129 (1981)
- [52] P. A. Grudowski, A. L. Holmes, C. J. Eiting, and R. D. Dupuis, "The Effect of Substrate Misorientation on the Photoluminescence Properties of GaN Grown on Sapphire by Metalorganic Chemical Vapor Deposition", *Applied Physics Letter*, v 69, 24 (1996)
- [53] J. C. Lin, Y. K. Su, W. H. Lan, T. M. Kuan, W. R. Chen, Y. C. Cheng, W. J. Lin, Y. C. Tzeng, and H. Y. Shin, "The Influence of Vicinal Sapphire Substrate on GaN Epilayers and LED Structures Grown by Metalorganic Chemical Vapor Deposition", *Material Science and Engineering B*, v 128, 107 (2006)
- [54] Z. Y. Li, W. Y. Uen, M. H. Lo, C. H. Chiu, P. C. Lin, C. T. Huang, T. C. Lu, H. C. Kuo, S. C. Wang, and Y. C. Huang, "Enhancing the Emission Efficiency of In_{0.2}Ga_{0.8}N/GaN MQW Blue LED by Using Appropriately Misoriented Sapphire Substrates", *Journal of the Electrochemical Society*, v 156, 2 (2009)
- [55] S. W. Kim, H. Aida, and T. Suzuki, "The Effect of a slight mis-orientation Angle of c-plane Sapphire Substrate on Surface and Crystal Quality of MOCVD Grown GaN Thin Films", *Physics Status Solidi (c)*, v 1, 2483 (2004)
- [56] S. M. Jeong, S. Kissinger, D. W. Kim, S. J. Lee, J. S. Kim, H. K. Ahn, and C. R. Lee, "Characteristic Enhancement of the Blue LED Chip by the Growth and Fabrication on Patterned Sapphire (0 0 0 1) Substrate", *Journal of Crystal Growth*, v 312, 258 (2010)
- [57] K. Tadatomo, H. Okagawa, Y. Ohuchi, T. Tsunekawa, Y. Imada, M. Kato and T. Taguchi, "High Output Power InGaN Ultraviolet Light-Emitting Diodes Fabricated on Patterned Substrates Using Metalorganic Vapor Phase Epitaxy", *Japanese Journal of Applied Physics*, v 40, 583 (2001)
- [58] D. S. Wu, W. K. Wang, W. C. Shih, R. H. Horng, C. E. Lee, W. Y. Lin, and J. S. Fang, "Enhanced Output Power of Near-Ultraviolet InGaN-GaN LEDs Grown on Patterned Sapphire Substrates", *IEEE Photonics Technology Letters*, v 17, 288 (2005)

- [59] Y. P. Hsu, S. J. Chang, Y. K. Su, J. K. Sheu, C. T. Lee, T. C. Wen, L. W. Wu, C. H. Kuo, C. S. Chang, and S. C. Shei, "Lateral Epitaxial Patterned Sapphire InGaN/GaN MQW LEDs", *Journal of Crystal Growth*, v 261, 466 (2004)
- [60] X. H. Wu, P. Fini, E. J. Tarsa, B. Heying, S. Keller, U. K. Mishra, S. P. DenBaars, and J. S. Speck, "Dislocation Generation in GaN Heteroepitaxy", *Journal of Crystal Growth*, v 189, 231 (1998)
- [61] D. Kapolnek, X. H. Wu, B. Heying, S. Keller, U. K. Mishra, S. P. Denbaars, and J. S. Speck, "Structural Evolution in Epitaxial Metalorganic Chemical Vapor Deposition Grown GaN Films on Sapphire", *Applied Physics Letter*, v 67, 1541 (1995)
- [62] X. H. Wu, L. M. Brown, D. Kapolnek, S. Keller, B. Keller, S. P. DenBaars, and J. S. Speck, "Defect Structure of Metal-organic Chemical Vapor Deposition-grown Epitaxial (0 0 0 1) GaN/Al₂O₃", *Journal of Applied Physics*, v 80, 3228 (1996)
- [63] H. K. Cho, J. Y. Lee, G. M. Yang and C. S. Kim, "Formation Mechanism of V Defects in the InGaN/GaN Multiple Quantum Wells Grown on GaN Layers with Low Threading Dislocation Density", *Applied Physics Letter*, v 79, 215 (2001)
- [64] J. S. Speck, and S. J. Rosner, "the Role of Threading Dislocations in the Physical Properties of GaN and Its Alloys", *Physica B*, v 24, 273-274 (1999)
- [65] M. S. Kumar, J. Y. Park, Y. S. Lee, S. J. Chung, C. H. Hong, and E. K. Suh, "Effect of barrier growth temperature on morphological evolution of green InGaN/GaN multi-quantum well heterostructures", *Journal of Physics D: Applied Physics*, v 40, 5050-5054 (2007)
- [66] X. H. Wu, C. R. Elsass, A. Abare, M. Mack, S. Keller, P. M. Petroff, S. P. DenBaars, J. S. Speck, and S. J. Rosner, "Structural origin of V-defects and correlation with localized excitonic centers in InGaN/GaN multiple quantum wells", *Applied Physics Letters*, v 72, 692 (1998)
- [67] J. Bruckbauer, P. R. Edwards, T. Wang, and R. W. Martin, "High resolution Cathodoluminescence hyperspectral imaging of surface features in InGaN/GaN multiple quantum well structures", *Applied Physics Letters*, v 98, 141908 (2011)
- [68] A. Hangleiter, F. Hitzel, C. Netzel, D. Fuhrmann, U. Rossow, G. Ade, and P. Hinze, "Suppression of nonradiative recombination by v-shaped pits in GaInN/GaN quantum wells produces a large increase in the light emission efficiency", *Physical Review Letters*, v 95, 127402 (2005)
- [69] Z. L. Weber, D. F. Ogletree, K. M. Yu, M. Hawkrige, J. Z. Domagala, J. B. Misiuk, A. E. Berman, A. Emara, and S. Bedair, "Structural defects and Cathodoluminescence of In_xGa_{1-x}N layers", *Physica Status Solidi C*, v 8, 2248-2250 (2011)

- [70] T. Mitsui, T. Sekiguchi, D. Fujita, and N. Koguchi, "Comparison between Electron Beam and Near-Field Light on the Luminescence Excitation of GaAs/AlGaAs Semiconductor Quantum Dots", *Japan Society of Applied Physics*, v 44, 1820-1824 (2005)
- [71] M. Toth and M. R. Phillips, "Monte Carlo Modeling of Cathodoluminescence Generation Using Electron Energy Loss Curves", *Scanning*, v 20, 425-432 (1998)
- [72] M. Toth, K. Fleischer, and M. R. Phillips, "Direct experimental evidence for the role of oxygen in the luminescent properties of GaN", *Physical Review B*, v 59, 1575 (1999)
- [73] X. Li, S. Q. Gu, E. E. Reuter, J. T. Verdeyen, and S. G. Bishop, "Effect of ebeam irradiation on a pn junction GaN light emitting diode", *Journal of Applied Physics*, v 80, 2687 (1996)
- [74] S. Dassonneville, A. Amokrane, B. Sieber, J. L. Farvacque, B. Beaumont, V. Bousquet, P. Gibart, K. Leifer, and J. D. Ganiere, "Cathodoluminescence intensity and dislocation contrast evolutions under electron beam excitation in epitaxial GaN laterally overgrown on (0001) sapphire", *Physica B*, v 273-274, 148 (1999)
- [75] Y. C. Chang, A. L. Cai, M. A. L. Johnson, J. F. Muth, and R. M. Kolbas, "Electron-beam-induced optical memory effects in GaN", *Applied Physics Letters*, v 80, 1675 (2002)
- [76] B. Dierre, X. L. Yuan, Y. Z. Yao, M. Kokoyama, and T. Sekiguchi, "Impact of electron beam irradiation on the Cathodoluminescence intensity for ZnO and GaN", *Journal of Material Science: Material Electron*, v 19, S307 (2008)
- [77] U. Jahn, S. Dhar, H. Kostial, I. M. Watson, and K. Fujiwara, "Electron-beam-induced modifications of electronic properties in GaN-based quantum well structures", *Institute of Physics Conference Series*, n 180, 337 (2003)
- [78] M. Toth, K. Fleischer, and M. R. Phillips, "Electron beam induced impurity electro-migration in unintentionally doped GaN", *MRS Proceedings*, v 537 (1998)
- [79] U. Jahn, S. Dhar, H. Kostial, I. M. Watson, and K. Fujiwara, "Low-energy electron-beam irradiation of GaN-based quantum well structures", *Physica Status Solidi C*, v 0, 2223-2226 (2003)
- [80] C. Kim, M. Yang, J. Yi, M. Kim, H. Song, J. Jeon, Y. Choi, T. K. Yoo and S. J. Leem, "Cathodoluminescence Characteristics of Large-Scale In-Rich InGa_N Grains and Effect of Low-Energy Electron-Beam Irradiation", *Journal of the Korean Physical Society*, v 37, 846-849 (2000)

- [81] I. A. Buyanova, Mt. Wagner, W. M. Chen, B. Monemar, J. L. Lindström, H. Amano, and I. Akasaki, "Photoluminescence of GaN: Effect of electron irradiation", *Applied Physics Letters*, v 73, 2968 (1998)
- [82] P. S. Vergeles, E. B. Yakimov, "EBIC investigation of InGaN/GaN multiple quantum well structures irradiated with low energy electrons", *Journal of Physics: Conference Series*, v 281, 012013 (2011)
- [83] P. S. Vergeles, N. M. Schmidt, E. E. Yakimov, and E. B. Yakimov, "Effect of low energy electron irradiation on optical properties of InGaN/GaN light emitting structures", *Physics Status Solidi C*, v 8, 1265-1268 (2011)
- [84] N. M. Schmidt, P. S. Vergeles, E. E. Yakimov, and E. B. Yakimov, "Effect of low-energy electron irradiation on the Cathodoluminescence of multiple quantum well (MQW) InGaN/GaN structures", *Solid State Communications*, v 151, 208-211 (2011)
- [85] M. N. Lockrey, and M. R. Phillips, "Stability of InGaN/GaN MQW luminescence under prolonged high current injection", *Microscopy and Microanalysis*, v 18, 1876 (2012)
- [86] T. M. Smeeton, M. J. Kappers, J. S. Barnard, M. E. Vickers, and C. J. Humphreys, "Electron-beam-induced strain within InGaN quantum wells: false indium "cluster" detection in the transmission electron microscope", *Applied Physics Letters*, v 83, 5419 (2003)
- [87] J. R. Matey, and J. Blanc, "Scanning capacitance microscopy", *Journal of Applied Physics*, v 57, 1437 (1985)
- [88] C. A. Klein, "Bandgap Dependence and Related Features of Radiation Ionization Energies in Semiconductors", *Journal of Applied Physics*, v 39, 2029 (1968)
- [89] B. G. Yacobi, and D. B. Holt, "Cathodoluminescence scanning electron microscopy of semiconductors", *Journal of Applied Physics*, v 59, 4 (1986)
- [90] K. J. Lethy, P. R. Edwards, C. Liu, P. A. Shields, D. W. E. Allsopp, and R. W. Martin, "Cathodoluminescence studies of GaN coalesced from nanopyramids selectively grown by MOVPE", *Semiconductor Science and Technology*, v 27, 085010 (2012)
- [91] B. Liu, R. Zhang, J. G. Zheng, X. L. Ji, and D. Y. Fu, "Compositional pulling effect and strain relief mechanism in AlGaN/AlN distributed bragg reflectors", *Applied Physics Letters*, v 98, 261916 (2011)
- [92] J. Priesol, and A. Šatka, "Cathodoluminescence characterization of InGaN/GaN QW pyramidal structure by Monte Carlo method", *ASDAM 2012, The Ninth International Conference on Advanced Semiconductor Devices and Microsystems*, v 11, 79 (2012)

- [93] S. Nakamura, T. Mukai, and M. Senoh, "Si- and Ge-doped GaN films grown with GaN buffer layers", *Japan Journal of Applied Physics*, v 31, 2883-2888 (1992)
- [94] E. F. Schubert, I. D. Goepfert, W. Grieshaber, and J. M. Redwing, "Optical properties of Si-doped GaN", *Applied Physics Letters*, v 71, 921 (1997)
- [95] F. Lu, D. Lee, D. Byrnes, E. Armour, and W. Quinn, "Blue LED growth from 2 inch to 8 inch", *SCIENCE CHINA Technological Sciences*, v 54, 33-37 (2011)
- [96] J. E. Northrup, and J. Neugebauer, "Indium-induced changes in GaN (0001) surface morphology", *Physical Review B*, v 60, R8473 (1999)
- [97] A. Cremades, V. Navarro, J. Piqueras, A. P. Lima, and O. Ambacher, "Inhomogeneous incorporation of In and Al in molecular beam epitaxial AlInGaN films", *Journal of Applied Physics*, v 90, 4868 (2001)
- [98] W. Liu, S. J. Chua, X. H. Zhang, and J. Zhang, "Effect of high temperature and interface treatments on photoluminescence from InGaN/GaN multiple quantum wells with green light emissions", *Applied Physics Letters*, v 83, 914 (2003)
- [99] H. Sato, T. Sugahara, Y. Naoi, and S. Sakai, "Compositional inhomogeneity of InGaN grown on sapphire and bulk GaN substrates by metalorganic chemical vapor deposition", *Japan Journal of Applied Physics*, v 37, 2013-2015 (1998)
- [100] H. J. Chang, C. H. Chen, Y. F. Chen, T. Y. Lin, L. C. Chen, K. H. Chen, and Z. H. Lan, "Direct evidence of nanocluster-induced luminescence in InGaN epilayers", *Applied Physics Letters*, v 86, 021911 (2005)
- [101] C. Li, E. B. Stokes, R. Hefti, P. Moyer, R. Arif, D. Byrnes, S. M. Lee and E. Armour, "Confocal microscopy and TRPL spectroscopy study on spatial variation of PL in blue-emitting InGaN/GaN MQWs", *ECS Transactions*, v 53, 43-51 (2013)
- [102] Y. Li, F. Lu, F. Ramos, and E. B. Stokes, "Cathodoluminescence studies of InGaN/GaN multiple quantum well structure grown by metalorganic chemical vapor deposition", *ECS Transactions*, v 53, 31-38 (2013)
- [103] S. J. Henley, A. Bewick, D. Cherns, and F.A. Ponce, "Luminescence studies of defects and piezoelectric fields in InGaN/GaN single quantum wells", *Journal of Crystal Growth*, v 230, 481-486 (2001)
- [104] T. Wang, P. J. Parbrook, W. H. Fan, and A. M. Fox, "Optical investigation of InGaN/GaN multiple-quantum wells under high excitation", *Applied Physics Letters*, v 84, 5159 (2004)

- [105] P. Riblet, H. Hirayama, A. Kinoshita, A. Hirata, T. Sugano, and Y. Aoyagi, "Determination of photoluminescence mechanism in InGaN quantum wells", *Applied Physics Letters*, v 75, 2241 (1999)
- [106] K. Kazlauskas, G. Tamulaitis, J. Mickevicius, E. Kuokstis, and A. Zukauskas, "Excitation power dynamics of photoluminescence in InGaN/GaN quantum wells with enhanced carrier localization", *Journal of Applied Physics*, v 97, 013525 (2005)
- [107] S. Chichibu, T. Sota, K. Wada, and S. Nakanura, "Exciton localization in InGaN quantum well devices", *Journal of Vacuum Science and Technology B*, v 16, 2204 (1998)
- [108] A. Kaneta, T. Mutoh, Y. Kawakami, and S. Fujita, "Discrimination of local radiative and nonradiative recombination processes in an InGaN/GaN single-quantum-well structure by a time-resolved multimode scanning near-field optical microscopy", *Applied Physics Letters*, v 83, 3462 (2003)
- [109] S. W. Feng, Y. C. Cheng, Y. Y. Chuang, C. C. Yang, M. H. Mao, Y. S. Lin, K. J. Ma, and J. I. Chyi, "Multiple-component photoluminescence decay caused by carrier transport in InGaN/GaN multiple quantum wells with indium aggregation structures", *Applied Physics Letters*, v 80, 4375 (2002)
- [110] S. W. Feng, Y. C. Cheng, Y. Y. Chung, C. C. Yang, and Y. S. Lin, "Impact of localized states on the recombination dynamics in InGaN/GaN quantum well structures", *Journal of Applied Physics*, v 92, 4441 (2002)
- [111] V. Liuolia, A. Pinos, S. Marcinkevičius, Y. D. Lin, H. Ohta, S. P. DenBaars, and S. Nakamura, "Carrier localization in m-plane InGaN/GaN quantum wells probed by scanning near field optical spectroscopy", *Applied Physics Letters*, v 97, 151106 (2010)
- [112] M. Pophristic, F. H. Long, C. Tran, R. F. Karlicek, Jr., Z. C. Feng and I. T. Ferguson, "Time-resolved spectroscopy of $\text{In}_x\text{Ga}_{1-2x}\text{N}/\text{GaN}$ multiple quantum wells at room temperature", *Applied Physics Letters*, v 73, 815 (1998)
- [113] S. O. Kucheyev, M. Toth, M. R. Phillips, J. S. Williams, C. Jagadish, and G. Li, "Chemical origin of the yellow luminescence in GaN", *Journal of Applied Physics*, v 91, 5867 (2002)
- [114] P. De Mierry, O. Ambacher, H. Kratzer, and M. Stutzmann, "Yellow luminescence and hydrocarbon contamination in MOVPE-grown GaN", *Physica Status Solidi A*, v 158, 587 (1996)
- [115] S. C. Cruz, S. Keller, T. E. Mates, U. K. Mishra, and S. P. DenBaars, "Crystallographic orientation dependence of dopant and impurity incorporation in

- GaN films grown by metalorganic chemical vapor deposition”, *Journal of Crystal Growth*, v 311, 3817 (2009)
- [116] N. A. Fichtenbaum, T. E. Mates, S. Keller, S. P. DenBaars, and U. K. Mishra, “Impurity incorporation in heteroepitaxial N-face and Ga-face GaN films grown by metalorganic chemical vapor deposition”, *Journal of Crystal Growth*, v 310, 1124 (2008)
- [117] M. Sumiya, K. Yoshimura, K. Ohtsuka, and S. Fuke, “Dependence of impurity incorporation on the polar direction of GaN film growth”, *Applied Physics Letters*, v 76, 2098 (2000)
- [118] D. I. Florescu, S. M. Ting, J. C. Ramer, D. S. Lee, and V. N. Merai, “Investigation of V-defects and embedded inclusion in InGaN/GaN multiple quantum wells grown by metalorganic chemical vapor deposition on (0001) sapphire”, *Applied Physics Letters*, v 83, 33 (2003)
- [119] X. A. Cao, S. J. Pearton, G. T. Dang, A. P. Zhang, F. Ren, R. G. Wilson, and J. M. Van Hove, “Creation of high resistivity GaN by implantation of Ti, O, Fe, or Cr”, *Journal of Applied Physics*, v 87, 1091 (2000)
- [120] J. Neugebauer, and C. G. Van de Walle, “Gallium vacancies and the yellow luminescence in GaN”, *Applied Physics Letters*, v 69, 503 (1996)
- [121] S. Pereira, M. R. Correia, E. Pereira, K. P. O’Donnell, C. T. Cowan, F. Sweeney, and E. Alves, “Compositional pulling effects in $\text{In}_x\text{Ga}_{1-x}\text{N}/\text{GaN}$ layers: a combined depth-resolved cathodoluminescence and Rutherford backscattering/channeling study”, *Physical Review B*, v 64, 205311 (2001)
- [122] Y. S. Lin, K. J. Ma, C. Hsu, S. W. Feng, Y. C. Cheng, C. C. Liao, C. C. Yang, C. C. Chou, C. M. Lee, and J. I. Chyi, “Dependence of composition fluctuation on indium content in InGaN/GaN multiple quantum wells”, *Applied Physics Letters*, v 77, 2988 (2000)
- [123] R. Fornari, M. Bosi, M. Avella, O. Martinez, and J. Jimenez, “Assessment of the short and long range homogeneity of MOVPE grown InGaN epilayers”, 10th European Workshop on MOVPE (2003)
- [124] M. Yoshikawa, M. Murakami, H. Ishida, and H. Harima, “Characterizing nanometer-sized V-defects in InGaN single quantum well films by high-spatial-resolution cathodoluminescence spectroscopy”, *Applied Physics Letters*, v 94, 131908 (2009)
- [125] C. B. Soh, S. Y. Chow, L. Y. Tan, H. Hartono, W. Liu, and S. J. Chua, “Enhanced luminescence efficiency due to carrier localization in InGaN/GaN heterostructures grown on nanoporous GaN templates”, *Applied Physics Letters*, v 93, 173107 (2008)

- [126] M. Pristovsek, J. Stellmach, M. Leyer, and M. Kneissl, "Growth mode of InGaN on GaN (0001) in MOVPE", *Physica Status Solidi C*, v6, s565-s569 (2009)
- [127] S. Srinivasan, F. Bertram, A. Bell, F. A. Ponce, and S. Tannaka, "Low stokes shift in thick and homogeneous InGaN epilayers", *Applied Physics Letters*, v 80, 550 (2002)
- [128] A. Vertikov, M. Kuball, A. V. Nurmikko, Y. Chen, and S. Y. Wang, "Near-field optical study of InGaN/GaN epitaxial layers and quantum wells", *Applied Physics Letters*, v 72, 2645 (1998)
- [129] G. Pozina, J. P. Bergman, B. Monemar, T. Takeuchi, and H. Amano, "Origin of multiple peak photoluminescence in InGaN/GaN multiple quantum wells", *Journal of Applied Physics*, v 88, 2677 (2000)
- [130] Y. Li, D. P. Byrnes, and E. B. Stokes, "Effect of barrier growth temperature on the material properties of InGaN/GaN multiple quantum well structures", *ECS Journal of Solid State Science and Technology*, v 2, R267-R272 (2013)
- [131] F. T. Moon, H. H. Lee, D. Y. Noh, and S. J. Park, "Growth-temperature dependent property of GaN barrier layer and its effect on InGaN/GaN multiple quantum well light-emitting diodes", *Journal of the Korean Physical Society*, v 42, 557-561 (2003)
- [132] L. W. Wu, S. J. Chang, Y. K. Su, R. W. Chuang, T. C. Wen, C. H. Kuo, W. C. Lai, C. S. Chang, J. M. Tsai, and J. K. Sheu, "Nitride-based green light-emitting diodes with high temperature GaN barrier layers", *IEEE transactions on electron devices*, v 50, 1766 (2003)
- [133] S. Kim, K. Lee, K. Park, and C. S. Kim, "Effects of barrier growth temperature on the properties of InGaN/GaN multiple-quantum wells", *Journal of Crystal Growth*, v 247, 62-68 (2003)
- [134] J. W. Ju, J. Zhu, H. S. Kim, C. R. Lee, and I. H. Lee, "Effects of p-GaN growth temperature on a green InGaN/GaN multiple quantum well", *Journal of Korean Physical Society*, v 50, 810-813 (2007)
- [135] J. B. Fedison, T. P. Chow, H. Lu, and I. B. Bhat, "Electrical characteristics of magnesium-doped gallium nitride junction diodes", *Applied Physics Letters*, v 72, 2841 (1998)
- [136] F. Bertram, T. Riemann, J. Christen, A. Kaschner, and A. Hoffmann, "Strain relaxation and strong impurity incorporation in epitaxial laterally overgrown GaN: Direct imaging of different growth domains by cathodoluminescence microscopy and micro-Raman spectroscopy", *Applied Physics Letters*, v 74, 359 (1999)